

NAVAL POSTGRADUATE SCHOOL
Monterey, California



THESIS

**DIAGNOSTIC INITIALIZATION GENERATED
EXTREMELY STRONG THERMOHALINE SOURCES AND
SINKS IN THE SOUTH CHINA SEA**

by

Ahchuan Ong

March 2003

Thesis Advisor:

Peter C. Chu

Second Reader:

Steve Haeger

Approved for public release; distribution is unlimited.

THIS PAGE INTENTIONALLY LEFT BLANK

REPORT DOCUMENTATION PAGE			<i>Form Approved OMB No. 0704-0188</i>	
Public reporting burden for this collection of information is estimated to average 1 hour per response, including the time for reviewing instruction, searching existing data sources, gathering and maintaining the data needed, and completing and reviewing the collection of information. Send comments regarding this burden estimate or any other aspect of this collection of information, including suggestions for reducing this burden, to Washington headquarters Services, Directorate for Information Operations and Reports, 1215 Jefferson Davis Highway, Suite 1204, Arlington, VA 22202-4302, and to the Office of Management and Budget, Paperwork Reduction Project (0704-0188) Washington DC 20503.				
1. AGENCY USE ONLY (Leave blank)		2. REPORT DATE March 2003	3. REPORT TYPE AND DATES COVERED Master's Thesis	
4. TITLE AND SUBTITLE: Diagnostic Initialization Generated Extremely Strong Thermohaline Sources and Sinks in the South China Sea			5. FUNDING NUMBERS	
6. AUTHOR(S) Ahchuan Ong				
7. PERFORMING ORGANIZATION NAME(S) AND ADDRESS(ES) Naval Postgraduate School Monterey, CA 93943-5000			8. PERFORMING ORGANIZATION REPORT NUMBER	
9. SPONSORING /MONITORING AGENCY NAME(S) AND ADDRESS(ES) NAVOCEANO Stennis Space Center, MS 39522-5001			10. SPONSORING/MONITORING AGENCY REPORT NUMBER	
11. SUPPLEMENTARY NOTES The views expressed in this thesis are those of the author and do not reflect the official policy or position of the Department of Defense or the U.S. Government.				
12a. DISTRIBUTION / AVAILABILITY STATEMENT Approved for public release; distribution is unlimited			12b. DISTRIBUTION CODE	
13. ABSTRACT (maximum 200 words) Ocean modeling is usually constrained by the lack of observed velocity data for the initial condition. The diagnostic initialization is widely used to generate velocity data as initial condition for ocean modeling. It integrates the model from known temperature (T_c), salinity (S_c) and zero velocity fields and holds (T_c , S_c) unchanged. After a period of the diagnostic run, the velocity field (V_c) is established, and (T_c , S_c , V_c) fields are treated as the initial conditions for the numerical modeling. During the diagnostic initialization period, the heat and salt 'source/sink' terms are generated at each time step. In this Thesis, the Princeton Ocean Model implemented to the South China Sea demonstrated extremely strong thermohaline sources and sinks generated by the diagnostic initialization. Such extremely strong and spatially non-uniform initial heating/cooling (salting/freshening) rates in the ocean model may cause drastic change in thermohaline and velocity fields initially (after the diagnostic run). There is a need to overcome such problems or find alternative methods as diagnostic initialization is extensively used.				
14. SUBJECT TERMS Ocean modeling, diagnostic initialization, thermohaline, POM, LEVITUS, SCS.			15. NUMBER OF PAGES 95	
			16. PRICE CODE	
17. SECURITY CLASSIFICATION OF REPORT Unclassified	18. SECURITY CLASSIFICATION OF THIS PAGE Unclassified	19. SECURITY CLASSIFICATION OF ABSTRACT Unclassified	20. LIMITATION OF ABSTRACT UL	

NSN 7540-01-280-5500

Standard Form 298 (Rev. 2-89)
Prescribed by ANSI Std. Z39-18

THIS PAGE INTENTIONALLY LEFT BLANK

Approved for public release; distribution is unlimited

**DIAGNOSTIC INITIALIZATION GENERATED EXTREMELY STRONG
THERMOHALINE SOURCES AND SINKS IN THE SOUTH CHINA SEA**

Ahchuan Ong
Major, Republic of Singapore Navy
B.S. (Math Honors), University of Singapore, 1993

Submitted in partial fulfillment of the
requirements for the degree of

MASTER OF SCIENCE IN PHYSICAL OCEANOGRAPHY

from the

**NAVAL POSTGRADUATE SCHOOL
March 2003**

Author Ahchuan Ong

Approved by: Peter C. Chu
 Thesis Advisor

Steve Haeger (NAVO)
Second Reader

Mary Batteen
Chairman, Department of Oceanography

THIS PAGE INTENTIONALLY LEFT BLANK

ABSTRACT

Ocean modeling is usually constrained by the lack of observed velocity data for the initial condition. The diagnostic initialization is widely used to generate velocity data as initial condition for ocean modeling. It integrates the model from known temperature (T_c), salinity (S_c) and zero velocity fields and holds (T_c , S_c) unchanged. After a period of the diagnostic run, the velocity field (\mathbf{V}_c) is established, and (T_c , S_c , \mathbf{V}_c) fields are treated as the initial conditions for the numerical modeling. During the diagnostic initialization period, the heat and salt ‘source/sink’ terms are generated at each time step. In this Thesis, the Princeton Ocean Model implemented to the South China Sea demonstrated extremely strong thermohaline sources and sinks generated by the diagnostic initialization. Such extremely strong and spatially non-uniform initial heating/cooling (salting/freshening) rates in the ocean model may cause drastic change in thermohaline and velocity fields initially (after the diagnostic run). There is a need to overcome such problems or find alternative methods as diagnostic initialization is extensively used.

THIS PAGE INTENTIONALLY LEFT BLANK

TABLE OF CONTENTS

I.	INTRODUCTION.....	1
A.	NUMERICAL OCEAN MODELING	1
B.	PROBLEMS OF THE DIAGNOSTIC INITIALIZATION.....	1
C.	CRITERIA FOR STRENGTH OF SOURCE/SINK.....	3
D.	PROPOSED RESEARCH IN THIS THESIS	4
II.	ENVIRONMENT OF THE SOUTH CHINA SEA	7
III.	MODEL DESCRIPTION	13
A.	FEATURES OF PRINCETON OCEAN MODEL (POM)	13
1.	Sigma Coordinate Model.....	13
2.	Free Surface and Mode Splitting.....	13
3.	Other Significant Attributes of POM.....	14
B.	SCS MODEL INPUT	14
C.	EXPERIMENT DESIGN	14
IV.	RESULT OF SENSITIVITY STUDY – EXTREMELY STRONG SOURCE/SINK TERMS IN DIAGNOSTIC INITIALIZATION.....	19
A.	HORIZONTAL DISTRIBUTION OF HEAT SOURCE/SINK TERMS	19
B.	HORIZONTAL DISTRIBUTION OF SALT SOURCE/SINK TERMS ..	25
C.	HORIZONTAL MEAN OF HEAT ‘SOURCE/SINK’ TERM ($M_s(F_T)$).....	31
D.	HORIZONTAL MEAN OF SALT ‘SOURCE/SINK’ TERM ($M_s(F_s)$).....	37
V.	UNCERTAINTY OF THE DIAGNOSTICALLY INITIALIZED VELOCITY FIELD DUE TO THE UNCERTAIN HORIZONTAL VISCOSITY	43
A.	HORIZONTAL VELOCITIES ON DAY-60 OF THE DIAGNOSTIC INITIALIZATION	43
B.	RELATIVE ROOT MEAN SQUARE DIFFERENCE OF VELOCITIES	48
VI.	UNCERTAINTY OF THE DIAGNOSTICALLY INITIALIZED VELOCITY FIELD DUE TO THE UNCERTAIN LENGTH OF DIAGNOSTIC INTEGRATION	57
VII.	CONCLUSIONS	61

APPENDIX A. HORIZONTAL DISTRIBUTION OF HEAT SOURCE/SINK TERMS	63
APPENDIX B. HORIZONTAL DISTRIBUTION OF SALT SOURCE/SINK TERMS	71
LIST OF REFERENCES	79
INITIAL DISTRIBUTION LIST.....	81

LIST OF FIGURES

Figure 1. Bathymetry (m) of the South China Sea (after Chu et al. 2001).....	7
Figure 2a and 2b. Climatological wind stress (a) Jun and (b) Dec (after Chu et al. 2001).....	9
Figure 3. Observational surface circulation: (a) Jun and (b) Dec (after Wyrki 1961).....	9
Figure 4. Kuroshio excursion near the Bashi Strait (after Tomczak 2003).....	10
Figure 5. Mixed layer depths of SCS taken from an AXBT experiment.....	11
Figure 6. Climatological Salinity and Sea Surface Temperature.....	12
Figure 7. Mean model kinetic energy per unit mass reached quasi-steady state when POM is implemented for the SCS after about 30 days	16
Figure 8. Mean model kinetic energy per unit mass reached quasi-steady state when POM is implemented for the SCS after about 30 days	16
Figure 9. Mean model kinetic energy per unit mass reached quasi-steady state when POM is implemented for the SCS after about 30 days	17
Figure 10. Mean model kinetic energy per unit mass reached quasi-steady state when POM is implemented for the SCS after about 30 days	17
Figure 11. Horizontal distribution of F_T on day-60 with $C = 0.05$	20
Figure 12. Horizontal distribution of F_T on day-60 with $C = 0.1$	21
Figure 13. Horizontal distribution of F_T on day-60 with $C = 0.2$	22
Figure 14. Horizontal distribution of F_T on day-60 with $C = 0.3$	23
Figure 15. Horizontal distribution of F_T near the bottom of SCS (- 4000m) on day-60 with different C -values.....	24
Figure 16. Horizontal distribution of F_S on day-60 with $C = 0.05$	26
Figure 17. Horizontal distribution of F_S on day-60 with $C = 0.1$	27
Figure 18. Horizontal distribution of F_S on day-60 with $C = 0.2$	28
Figure 19. Horizontal distribution of F_S on day-60 with $C = 0.3$	29
Figure 20. Horizontal distribution of F_S near the bottom of SCS (- 4000m) on day-60 with different C -values.....	30
Figure 21. Temporal evolution of $M_S(F_T)$ at four different S levels with $C = 0.05$	31
Figure 22. Temporal evolution of $M_S(F_T)$ at four different S levels with $C = 0.1$	32
Figure 23. Temporal evolution of $M_S(F_T)$ at four different S levels with $C = 0.2$	32
Figure 24. Temporal evolution of $M_S(F_T)$ at four different S levels with $C = 0.3$	33
Figure 25. Depth profiles of $M_S(F_T)$ with $C = 0.05$	35
Figure 26. Depth profiles of $M_S(F_T)$ with $C = 0.1$	35
Figure 27. Depth profiles of $M_S(F_T)$ with $C = 0.2$	36
Figure 28. Depth profiles of $M_S(F_T)$ with $C = 0.3$	36
Figure 29. Temporal evolution of $M_S(F_S)$ at four different S levels with $C = 0.05$	38
Figure 30. Temporal evolution of $M_S(F_S)$ at four different S levels with $C = 0.1$	39
Figure 31. Temporal evolution of $M_S(F_S)$ at four different S levels with $C = 0.2$	39
Figure 32. Temporal evolution of $M_S(F_S)$ at four different S levels with $C = 0.3$	40

Figure 33. Depth profiles of $M_s(F_s)$ with $C = 0.05$	40
Figure 34. Depth profiles of $M_s(F_s)$ with $C = 0.1$	41
Figure 35. Depth profiles of $M_s(F_s)$ with $C = 0.2$	41
Figure 36. Depth profiles of $M_s(F_s)$ with $C = 0.3$	42
Figure 37. Horizontal velocities on the 60 th day ($C=0.05$)	44
Figure 38. Horizontal velocities on the 60 th day ($C = 0.1$)	45
Figure 39. Horizontal velocities on the 60 th day ($C = 0.2$)	46
Figure 40. Horizontal velocities on the 60 th day ($C = 0.3$)	47
Figure 41. Temporally Varying of $RRMSDV(k, 0.05)$	50
Figure 42. Temporally Varying of $RRMSDW(k, 0.05)$	50
Figure 43. Depth profiles of $RRMSDV(k, 0.05)$ at different day.....	51
Figure 44. Depth profiles of $RRMSDW(k, 0.05)$ at different day.....	51
Figure 45. Temporally Varying of $RRMSDV(k, 0.1)$	52
Figure 46. Temporally Varying of $RRMSDW(k, 0.1)$	52
Figure 47. Depth profiles of $RRMSDV(k, 0.1)$ at different day.....	53
Figure 48. Depth profiles of $RRMSDW(k, 0.1)$ at different day.....	53
Figure 49. Temporally Varying of $RRMSDV(k, 0.3)$	54
Figure 50. Temporally Varying of $RRMSDW(k, 0.3)$	54
Figure 51. Depth profiles of $RRMSDV(k, 0.3)$ at different day	55
Figure 52. Depth profiles of $RRMSDW(k, 0.3)$ at different day.....	55
Figure 53. Temporally varying of $RRMSDV(t)$ with four different C -values	58
Figure 54. Temporally varying of $RRMSDW(t)$ with four different C -values	59

ACKNOWLEDGMENTS

The author is grateful for the professional expertise and guidance provided by Dr. Peter C. Chu and Mr. Steven Haeger. This study would not have been possible without the technical expertise of Chenwu Fan at the Naval Postgraduate School and encouragement of Leeling Chua, my wife. This work was funded by the Naval Oceanographic Office and the Naval Postgraduate School.

THIS PAGE INTENTIONALLY LEFT BLANK

I. INTRODUCTION

A. NUMERICAL OCEAN MODELING

Numerical ocean modeling is essential to achieve better understanding and prediction of the ocean behavior. It integrates hydrodynamic and thermodynamic equations numerically with boundary conditions (lateral and vertical) from initial states of temperature (T), salinity (S) and velocity. Besides having a good ocean model, it is essential to have reliable data for specifying the initial condition in order to achieve accurate prediction. Past observations of the ocean have contributed greatly to our knowledge of the T and S fields. Relatively reliable climatological (T_c , S_c) datasets can be obtained from the National Oceanographic Data Center (NODC) or the Navy's Global Digital Environmental Model (GDEM) as initial T and S fields input for the ocean model. However, initial velocity field is usually not available due to insufficient number of velocity observations and difficulty to obtain such data. Thus, initialization of velocity field becomes an important procedure for the ocean modeling. In order to accurately predict the ocean behaviors using numerical ocean modeling, a reliable initialization process for the velocity field is essential.

B. PROBLEMS OF THE DIAGNOSTIC INITIALIZATION

A widely used model initialization for the velocity field is the diagnostic mode. This process integrates the model from climatological (T_c , S_c), zero velocity fields and holds (T_c , S_c) unchanged. After a period of about 30 days of the diagnostic run, a quasi-steady state is achieved and the velocity field (V_c) is established. (T_c , S_c , V_c) fields are treated as the initial conditions for the numerical modeling. Since initial condition error can drastically affect the model's predictability [Lorenz, 1969; Chu 1999], there is a need to ensure that the initial condition data are correctly determined. Since diagnostic mode model initialization is being used extensively, there is a need to examine the reliability of such an initialization process and determine whether such an approach leads to any non-physical phenomenon.

Chu and Lan [2003] pointed out the problems of the diagnostic initialization and found that such an initialization is artificially adding extremely strong heat/salt sources or

sinks in the ocean. Their arguments are outlined as follows. The horizontal momentum equations for the numerical ocean models are based on

$$\frac{\partial \mathbf{V}}{\partial t} = -\mathbf{V} \cdot \nabla \mathbf{V} - w \frac{\partial \mathbf{V}}{\partial z} - \mathbf{k} \times f \mathbf{V} - \frac{1}{\rho} \nabla p + \frac{\partial}{\partial z} (K_M \frac{\partial \mathbf{V}}{\partial z}) + \mathbf{H}_V, \quad (1)$$

where $\mathbf{V} = (u, v)$ and w is the horizontal and vertical velocity components respectively. ∇ is the horizontal gradient operator. The temperature and salinity equations are

$$\frac{\partial T}{\partial t} = -\mathbf{V} \cdot \nabla T - w \frac{\partial T}{\partial z} + \frac{\partial}{\partial z} (K_H \frac{\partial T}{\partial z}) + H_T, \quad (2)$$

$$\frac{\partial S}{\partial t} = -\mathbf{V} \cdot \nabla S - w \frac{\partial S}{\partial z} + \frac{\partial}{\partial z} (K_H \frac{\partial S}{\partial z}) + H_S, \quad (3)$$

where f is the Coriolis parameter, ρ the density, p the pressure, and (K_M, K_H) the vertical eddy diffusivity for turbulent mixing of momentum, temperature, and salinity. The terms (\mathbf{H}_V, H_T, H_S) represent horizontal diffusion and the subgrid processes causing the local time rate of change in (\mathbf{V}, T, S) .

The diagnostic initialization is to integrate (1)-(3) under the following conditions:

$$T = T_c, \quad S = S_c, \quad \mathbf{V} = 0, \quad \text{at } t = 0, \quad (4)$$

with T and S unchanged. This is analogous to the process of adding heat and salt source/sink terms (F_T, F_S) in (2) and (3). Thus, equations (2) and (3) become

$$\frac{\partial T}{\partial t} = -\mathbf{V} \cdot \nabla T - w \frac{\partial T}{\partial z} + \frac{\partial}{\partial z} (K_H \frac{\partial T}{\partial z}) + H_T + F_T, \quad (5)$$

$$\frac{\partial S}{\partial t} = -\mathbf{V} \cdot \nabla S - w \frac{\partial S}{\partial z} + \frac{\partial}{\partial z} (K_H \frac{\partial S}{\partial z}) + H_S + F_S, \quad (6)$$

and keeping

$$\frac{\partial T}{\partial t} = 0, \quad \frac{\partial S}{\partial t} = 0 \quad (7)$$

at each time step. Combining (5), (6) and (7) leads to

$$F_T \equiv \mathbf{Vg}\nabla T + w \frac{\partial T}{\partial z} - \frac{\partial}{\partial z} (K_H \frac{\partial T}{\partial z}) - H_T, \quad (8)$$

$$F_S \equiv \mathbf{Vg}\nabla S + w \frac{\partial S}{\partial z} - \frac{\partial}{\partial z} (K_H \frac{\partial S}{\partial z}) - H_S. \quad (9)$$

Thus, the heat and salt ‘source/sink’ terms F_T and F_S are generated artificially at each time step during the diagnostic initialization. There is a need to examine how large are these source/sink terms generated from the initialization process to determine whether these false ‘sources/sinks’ are physical or bearable for numerical modeling. In this thesis, POM is implemented for the SCS to evaluate the magnitude of the source/sink terms from the diagnostic initialization. Prior to describing the SCS and the model essential features, the measures/criteria of the artificial heat and salt ‘source/sink’ terms F_T and F_S have to be established.

C. CRITERIA FOR STRENGTH OF SOURCE/SINK

Chu and Lan (2003) had proposed the criteria for the strength of the artificial source and sink generated during diagnostic initialization. Based on the SCS condition, the maximum annual variability of T, S is estimated to be about 35°C and 15 ppt respectively. Thus, the maximum rates of absolute change of the T, S data are estimated as follows:

$$\left| \frac{\partial T}{\partial t} \right| \leq \frac{35^\circ\text{C}}{\text{yr}} \approx 0.1^\circ\text{C}/\text{day}, \quad \left| \frac{\partial S}{\partial t} \right| \leq \frac{15 \text{ ppt}}{\text{yr}} \approx 0.04 \text{ ppt}/\text{day}. \quad (10)$$

These values are used as standard measures for ‘source/sink’. Twenty four times of the standard measures (10) represent strong ‘source/sink’ and is given as follows:

$$\left| \frac{\partial T}{\partial t} \right|_{\text{Strong}} \approx 0.1^\circ\text{C}/\text{hr}, \quad \left| \frac{\partial S}{\partial t} \right|_{\text{Strong}} \approx 0.04 \text{ ppt}/\text{hr} \quad (11)$$

Ten times of the strong ‘source/sink’ measures (11) represent extremely strong ‘source/sink’ and is given by:

$$\left| \frac{\partial T}{\partial t} \right|_{\text{Extremely Strong}} \approx 1^\circ\text{C/hr} , \quad \left| \frac{\partial S}{\partial t} \right|_{\text{Extremely Strong}} \approx 0.4 \text{ ppt/hr} . \quad (12)$$

D. PROPOSED RESEARCH IN THIS THESIS

Although *Chu and Lan* [2003] found the problem of the diagnostic initialization (generation of spurious heat/salt sources and sinks), they did not analyze the uncertainty of the initialized velocity field to the uncertainty of horizontal eddy viscosity and the duration of the diagnostic initialization.

The horizontal viscosity is usually taken from the Smagorinsky (1963) formula,

$$A_M = C \Delta x \Delta y \frac{1}{2} \left| \Delta V + (\Delta V)^T \right| \quad (13)$$

where

$$\frac{1}{2} \left| \Delta V + (\Delta V)^T \right| = \left[(\partial u / \partial x)^2 + (\partial v / \partial x + \partial u / \partial y)^2 + (\partial v / \partial y)^2 \right]^{\frac{1}{2}}, \quad (14)$$

C is the horizontal viscosity parameter.

This thesis is a follow-on work of *Chu and Lan* [2003] to examine the following issues that have not been done earlier:

1. How long is the duration of the diagnostic initialization needed to get a suitable initial velocity field?
2. How does the uncertainty of the horizontal viscosity parameter C affect the artificial heat/salt sources and sinks generated during the diagnostic initialization?
3. How does the uncertainty of C affect the initial velocity field (\mathbf{V}) derived from the diagnostic initiation process?
4. How is the uncertainty of the velocity field (\mathbf{V}) due to the uncertain duration of the diagnostic initialization?

Different from the result presented by *Chu and Lan* [2003], which was based on the Japan/East Sea, this thesis's area of study is the South China Sea (SCS). The Princeton Ocean Model [POM, *Blumberg and Mellor*, 1987] was implemented for the SCS to investigate the physical outcome of the diagnostic initialization with no surface and lateral forcing. The NODC annual mean (T_∞ , S_∞) data with $1^\circ \times 1^\circ$ resolution [*Levitus et al.*, 1994] was used. The SCS model was initialized diagnostically for 90 days with

four different values (0.05, 0.1, 0.2, 0.3) of the horizontal viscosity parameter C . The 60th day velocity field with $C = 0.2$ was taken as the reference to investigate the uncertainty of the diagnostic initialization.

THIS PAGE INTENTIONALLY LEFT BLANK

II. ENVIRONMENT OF THE SOUTH CHINA SEA

The South China Sea (SCS) is the largest marginal sea in the Western Pacific Ocean. It includes within its boundaries large shelf regions and deep basins. The deepest water is confined to a bowl-type trench between the Philippines and Vietnam, around 4300 m deep. It includes the shallow Gulf of Thailand and connections to the East China Sea (through the Taiwan Strait), the Pacific Ocean (through the Luzon Strait), the Sulu Sea (through the Mindoro Strait), the Java Sea (through the Gasper and Karimata Straits) and the Indian Ocean (through the Strait of Malacca). It has a total surface area of about $3.5 \times 10^6 \text{ km}^2$. South of 5° N , the water depth drops to 100m and less as shown in the bathymetry chart.

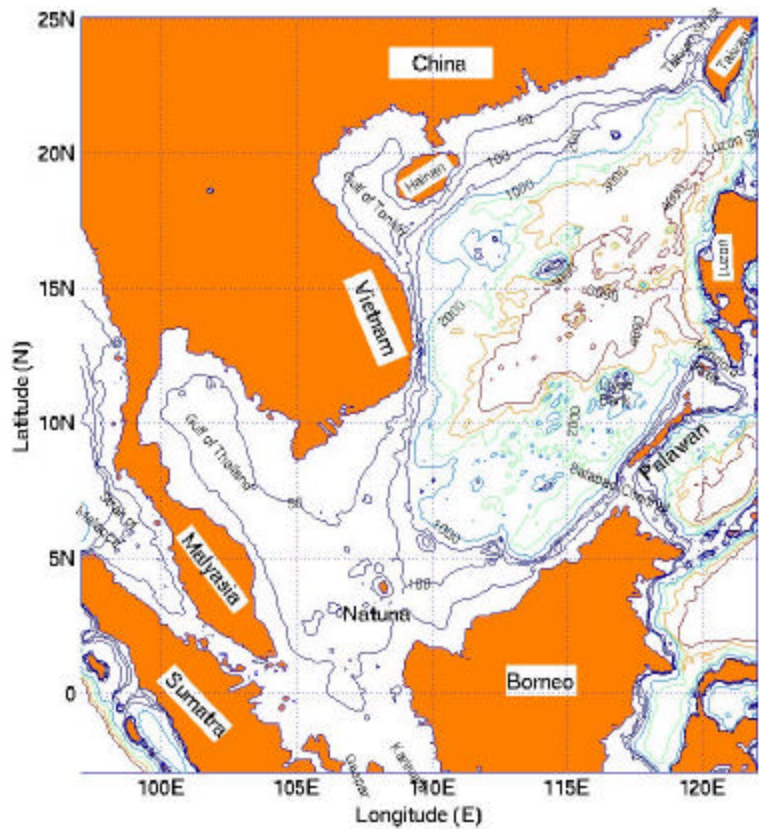


Figure 1. Bathymetry (m) of the South China Sea (After Chu et al. 2001)

All the connecting straits of SCS are shallow except the Luzon Strait, which has a sill depth of 2600m. Consequently the SCS is considered a semi-enclosed water body (Huang et al., 1994). The complex topography includes the broad shallows of the Sunda Shelf in the south/southwest; the continental shelf of the Asian landmass in the north, extending from the Gulf of Tonkin to the Taiwan Strait; a deep, elliptical shaped basin in the center, and numerous reef islands and underwater plateaus scattered throughout. The shelf that extends from the Gulf of Tonkin to the Taiwan Strait is consistently near 70 m deep, and averages 150 km in width; the central deep basin is 1900 km along its major axis (northeast-southwest) and approximately 1100 km along its minor axis, and extends to over 4000 m deep. The Sunda Shelf is the submerged connection between southeast Asia, Malaysia, Sumatra, Java, and Borneo and is 100 m deep in the middle; the center of the Gulf of Thailand is about 70 m deep.

The SCS is subjected to a seasonal monsoon system (Wyrki, 1961). From April to August, the weaker southwesterly summer monsoon winds result in a wind stress of over 0.1 N/m^2 (Figure 2a) which drives a northward coastal jet off Vietnam and anticyclonic circulation in the SCS (Figure 3a). From November to March, the stronger northeasterly winter monsoon winds corresponds to a maximum wind stress of nearly 0.3 N/m^2 (Figure 2b) causing a southward coastal jet and cyclonic circulation in the SCS (Figure 3b). The transitional periods are marked by highly variable winds and surface currents.

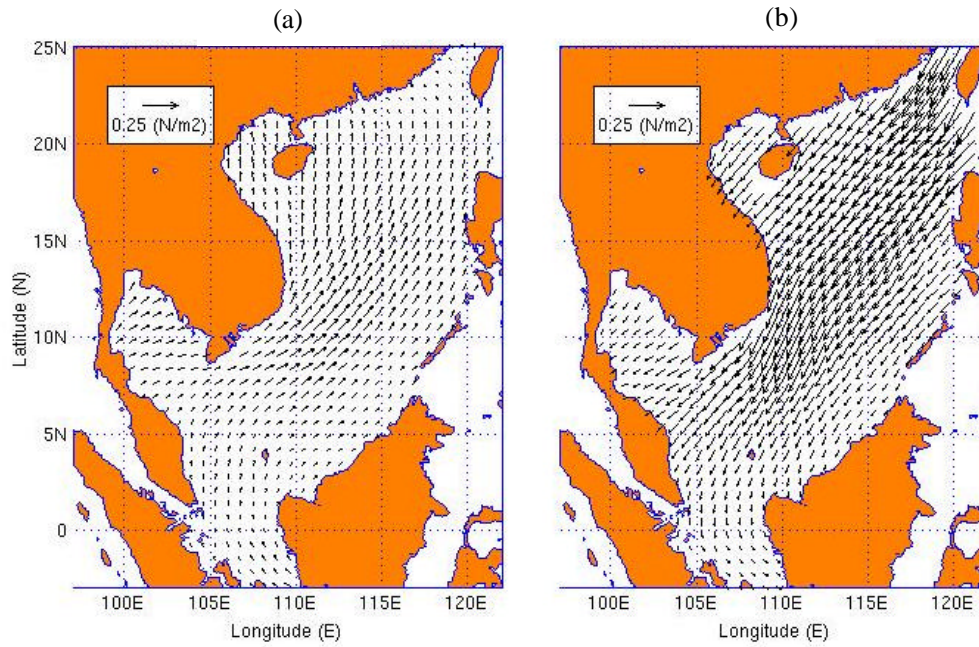


Figure 2a and 2b. Climatological wind stress (a) Jun and (b) Dec (after Chu et al. 2001)

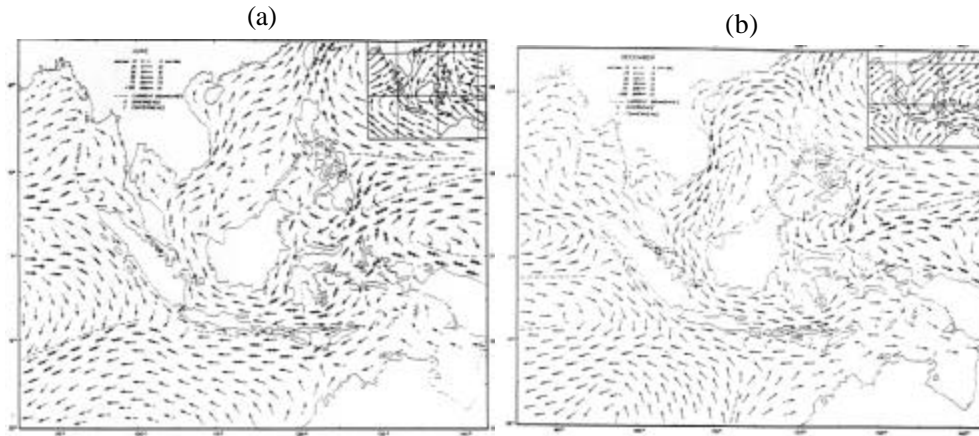


Figure 3. Observational surface circulation: (a) Jun and (b) Dec (after Wyrski 1961)

The observed circulation patterns of the intermediate to upper layers of the SCS are primarily forced by the local monsoon systems (Wyrski, 1961), with contributions from the Kuroshio Current via the Luzon Strait (or called Bashi Channel), in the southern half of the Luzon Strait. The Kuroshio enters the SCS through the southern side of the

channel then executes a tight, anticyclonic turn and exits the SCS near Taiwan. Because of the kuroshio excursion near the Bashi Strait, occasionally anti-cyclonic rings detached from the Kuroshio front would propagate westward into the SCS. This results in a persistent southwestward strong current exists near the Dongsha Islands, shown in Figure 4.

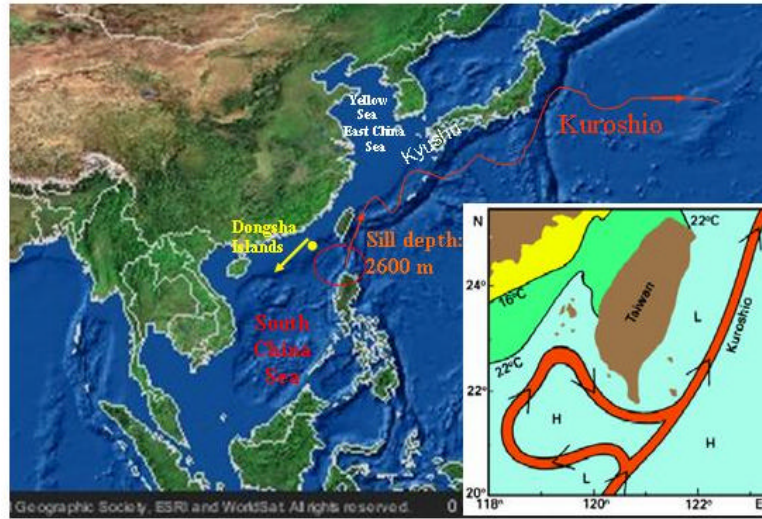


Figure 4. Kuroshio excursion near the Bashi Strait (after Tomczak 2003)

Upwelling and downwelling occur off the coast of central Vietnam and eastern Hainan. In the north, the waters are cold and saline. The annual variability of salinity is small, due to the inflow and diffusion of high salinity water from the Pacific Ocean through the Luzon Strait. In the south the tropical conditions cause the waters to be warmer and fresher. During the transitions the central region is alternately subjected to high and low salinity inflow as the monsoons reverse, resulting in a region of higher horizontal gradient and annual variability. Mixed layer depths vary from 30 to 40 m during the summer monsoon, and 70 to 90 m (Figure 5) during the winter monsoon with variations due to both winds and currents (Wyrski, 1961). Salinity near the coast of major rivers outflow tends to be lower, such as the coast near to Mekong and Pearl rivers, shown in Figure 6.

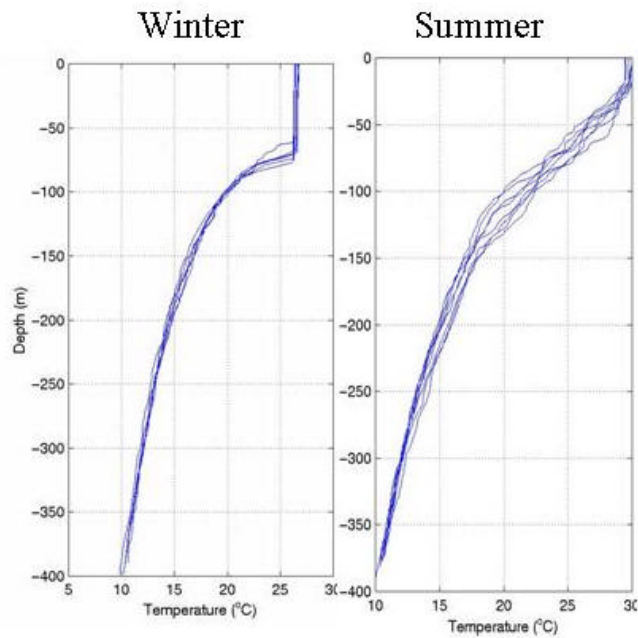


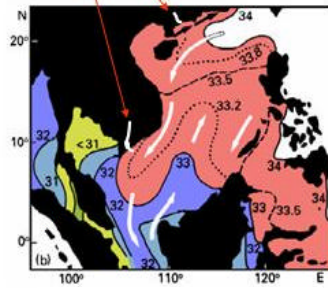
Figure 5. Mixed layer depths of SCS taken from an AXBT experiment

In winter, the sea surface temperature is generally above 25°C south of 16°N and ranges from 20 to 25°C north of 16°N. During summer, sea surface temperature is about 29°C south of 16°N and ranges from 25 to 29°C north of 16°N. (See Figure 6 for the sea surface temperature plot.)

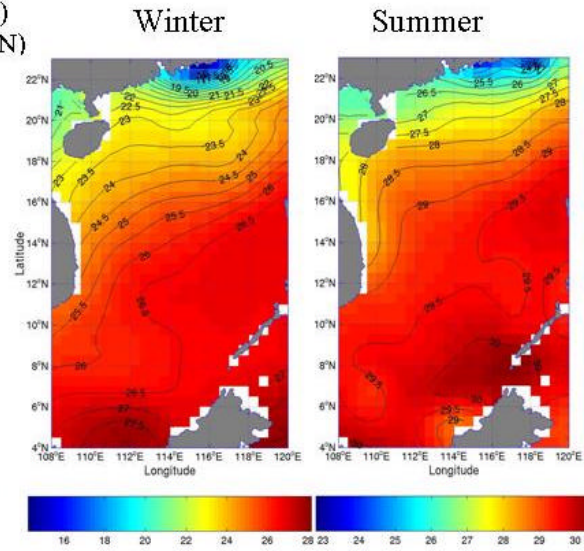
- Winter: 20-25°C ($> 16^{\circ}\text{N}$)
25-27.5°C ($< 16^{\circ}\text{N}$)

- Summer:
25-29°C ($> 16^{\circ}\text{N}$)
29-30°C ($< 16^{\circ}\text{N}$)

- Pearl & Mekong Rivers



Climatological Salinity



Climatological Sea Surface Temperature

Figure 6. Climatological Salinity and Sea Surface Temperature

III. MODEL DESCRIPTION

A. FEATURES OF PRINCETON OCEAN MODEL (POM)

The Princeton Ocean Model (Alan Blumberg and George Mellor, 1987) is a time-dependent, primitive equation numerical model on a three-dimensional grid that includes realistic topography and a free surface. The significant attributes of the model are as follows:

1. Sigma Coordinate Model

It is a sigma coordinate model in that the vertical coordinate is scaled on the water column depth. The sigma coordinate equations are based on the following transformation:

$$x^* = x, y^* = y, \mathbf{s} = \frac{z - \mathbf{h}}{H + \mathbf{h}}, t^* = t \quad (15)$$

where x, y, z are the conventional cartesian coordinates; $D \equiv H + \mathbf{h}$ where $H(x, y)$ is the bottom topography and $\mathbf{h}(x, y, t)$ is the surface elevation. Thus, \mathbf{s} ranges from $\mathbf{s} = 0$ at $z = \mathbf{h}$ to $\mathbf{s} = -1$ at $z = -H$. The sigma coordinate system is necessary in dealing with significant topographical variability such as that encountered over continental shelf breaks and slopes. Together with the turbulence sub-model, the model produces realistic bottom boundary layers, which are important in coastal waters (Mellor, 1985).

2. Free Surface and Mode Splitting

The model has a free surface and a split time step. For computational efficiency, the mode splitting technique [Blumberg and Mellor, 1987] is applied with a barotropic time step of 25 seconds, based on the Courant-Friederichs-Levy (CFL) computational stability condition and the external wave speed; and a baroclinic time step of 900 seconds, based on the CFL condition and the internal wave speed.

3. Other Significant Attributes of POM

POM contains an imbedded second moment turbulence closure sub-model to provide vertical mixing coefficients. The horizontal grid uses curvilinear orthogonal coordinates. The horizontal time differencing is explicit whereas the vertical differencing is implicit. The latter eliminates time constraints for the vertical coordinate and permits the use of fine vertical resolution in the surface and bottom boundary layers.

B. SCS MODEL INPUT

The SCS model contains 125×162 horizontally fixed grid points with 23 σ levels. The horizontal spacing is $\sim 0.179^\circ$ by 0.175° in the latitudinal and longitudinal direction (approximately 20 km resolution). The model domain is from 3.06°S to 25.07°N , and from 98.84°E to 121.16°E , which encompasses the SCS and the Gulf of Thailand. The bottom topography is obtained from the smoothed Naval Oceanographic Office Digital Bathymetry Data Base with 5 minutes resolution. The horizontal diffusivities are modeled using the Smagorinsky form with the parameter C chosen to be 0.05, 0.1, 0.2 and 0.3 for this application. No atmospheric forcing is applied to the model.

Closed lateral boundaries, that is, the modeled ocean bordered by land, were defined using a free slip condition for velocity and a zero gradient condition for temperature and salinity. No advective or diffusive heat, salt or velocity fluxes occur through these boundaries. At open boundaries, the radiative boundary condition is used with zero volume transport.

The bottom stress is assumed to follow a quadratic forcing

$$\mathbf{t}_b = \mathbf{r}_\sigma D_d |\mathbf{V}_b| \mathbf{V}_b \quad (16)$$

where $\mathbf{r}_\sigma = 1025 \text{ kg m}^{-3}$ is assigned as the density of the seawater. \mathbf{V}_b is the horizontal component of the bottom velocity, and D_d is the drag coefficient, which is specified as 0.0025 (Blumberg and Mellor 1987) in the model.

C. EXPERIMENT DESIGN

To analyze the impact of the uncertainty of the C to the initialized velocity field, one control run and three sensitivity runs of the POM were implemented on the SCS

model. The control run was conducted with $C = 0.2$ while the three sensitivity runs were conducted with $C = 0.05, 0.1$ and 0.3 .

To assess the duration of the initialization and its impact on the velocity field under different C -values, the diagnostic model was integrated for 90 days for the four cases of C -values. The 60th day of the model result was used as reference to compute the relative root mean square difference of the velocities between day-60 and day- i ($i = 60, 61, 62, \dots, 90$) to investigate the sensitivity of the initialized velocity field due to the uncertainty of the initialization period.

The POM diagnostic mode was integrated with all three components of velocity (u, v, w) initially set to zero, and with temperature and salinity specified by interpolating annual mean data to each model grid point. The heat and salt ‘source/sink’ terms F_T and F_S were obtained at each time step. The horizontal distributions of the heat and salt source/sink terms at the surface, subsurface, mid-level and near bottom were derived and compared to the measures established in (10), (11) and (12). In addition, the horizontal mean $|F_T|$ and mean $|F_S|$ on the \mathbf{S} level with N grid points are calculated in Chapter IV to identify the overall strength of the thermohaline source/sink terms generated in the diagnostic initiation process.

The experiment revealed that 30 days were sufficient for the mean model kinetic energy per unit mass to reach quasi-steady state under the imposed conditions as illustrated in Figures 7 to 10. The thermohaline source/sink terms (F_T, F_S) generated by the diagnostic initialization on day-30, day-45, day-60 and day-90 were used to identify their magnitudes and sensitivity to the integration period.

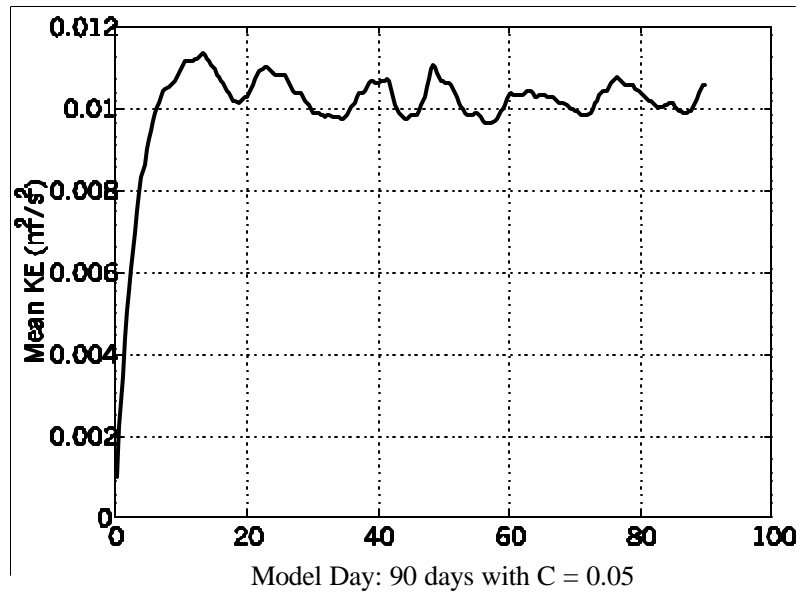


Figure 7. Mean model kinetic energy per unit mass reached quasi-steady state when POM is implemented for the SCS after about 30 days

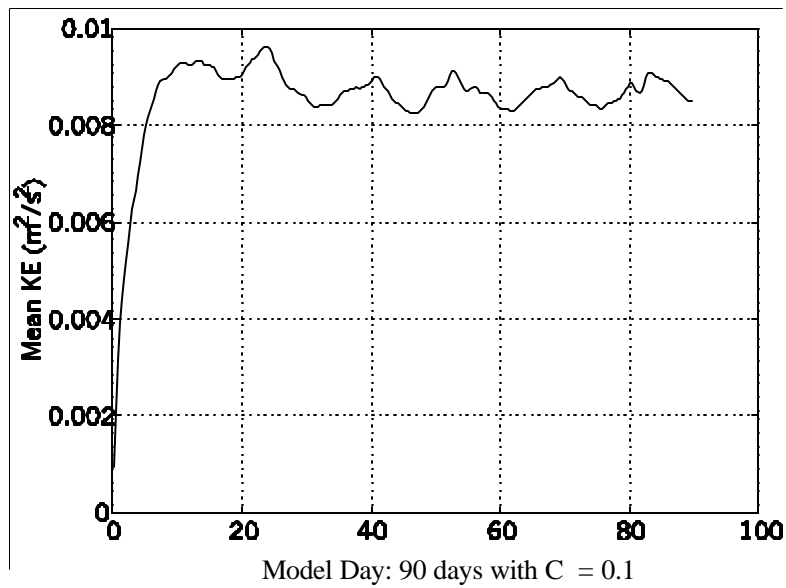


Figure 8. Mean model kinetic energy per unit mass reached quasi-steady state when POM is implemented for the SCS after about 30 days

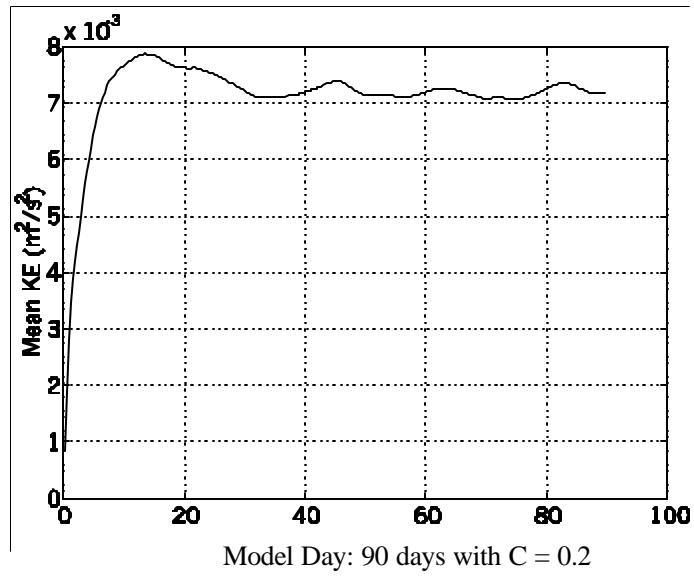


Figure 9. Mean model kinetic energy per unit mass reached quasi-steady state when POM is implemented for the SCS after about 30 days

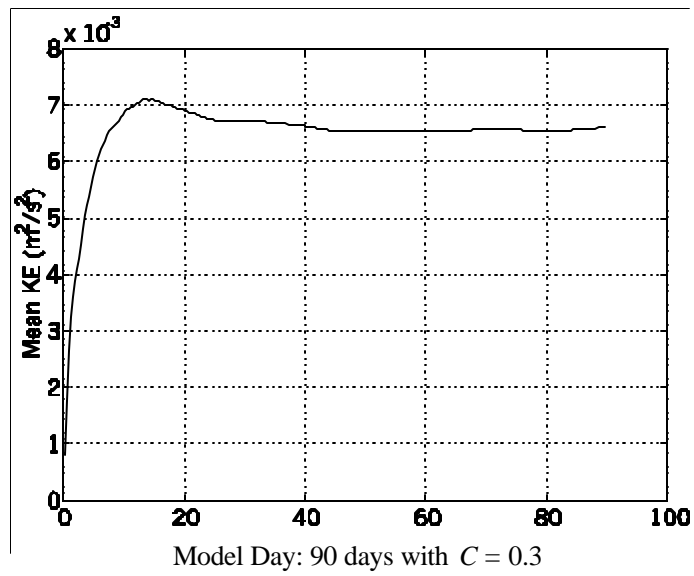


Figure 10. Mean model kinetic energy per unit mass reached quasi-steady state when POM is implemented for the SCS after about 30 days

THIS PAGE INTENTIONALLY LEFT BLANK

IV. RESULT OF SENSITIVITY STUDY – EXTREMELY STRONG SOURCE/SINK TERMS IN DIAGNOSTIC INITIALIZATION

A. HORIZONTAL DISTRIBUTION OF HEAT SOURCE/SINK TERMS

The criteria (11) and (12) are used to measure the strength of the non-physical (artificially created) heat ‘source/sink’ terms generated during the diagnostic initialization. The horizontal distributions of F_T ($^{\circ}\text{C hr}^{-1}$) generated by the diagnostic initialization at the four levels (near surface, subsurface, mid-level and near bottom) with four different C -values show extremely strong heat sources/sinks. The heat sources/sinks have various scales and strengths. They reveal small- to meso-scale patterns from the surface to the bottom of SCS and include some large-scale patterns near the surface (Figures 11 to 14). Near the surface (-10 m) of Taiwan Strait, there is an extremely strong heat source present in a large-scale pattern. At this location, the maximum time rate of temperature change is $2.217^{\circ}\text{C hr}^{-1}$ which corresponds to an extremely strong source of 2642 Wm^{-3} ($= r c_p F_T$) with $C = 0.1$. Isolated strong heat sources (meso-scale pattern) are also present near the surface of Gasper and Karimata Straits, southeast of Vietnam and Gulf of Thailand. These features are similar for the four different C -values but in general the magnitude of the heat sources decreases when C increases.

The extremely strong sink is located at the subsurface off Balabac Channel. At this location, the extremely strong heat sink reached -3371 Wm^{-3} (corresponding to $F_T = -2.828^{\circ}\text{C hr}^{-1}$) with $C = 0.05$. Near the northeast of Hainan island and southwest of Vietnam (8°N and 104°E), isolated strong heat sinks are present in small to meso-scale pattern near the surface. From the subsurface (-100 m) to the mid-level (-1500 m), numerous small-scale patterns of strong/extremely strong sources and sinks are well mixed and distributed over some areas, such as west of Palawan and northwest of Borneo. Near the bottom (-3000 m to -4000 m), the non-physical heat sources and sinks are relatively weak.

In general, when C -value increases, the non-physical sources/sinks weaken, nevertheless, they are still above the extremely strong heat source criterion (12) in some locations of SCS (as shown in Figure 14 when $C = 0.3$). It was observed that larger C would lead to smaller non-physical heat sources and sinks. However, an excessively

large C -value could cause unrealistically strong diffusion in the ocean model and could create other adverse consequences to the model results.

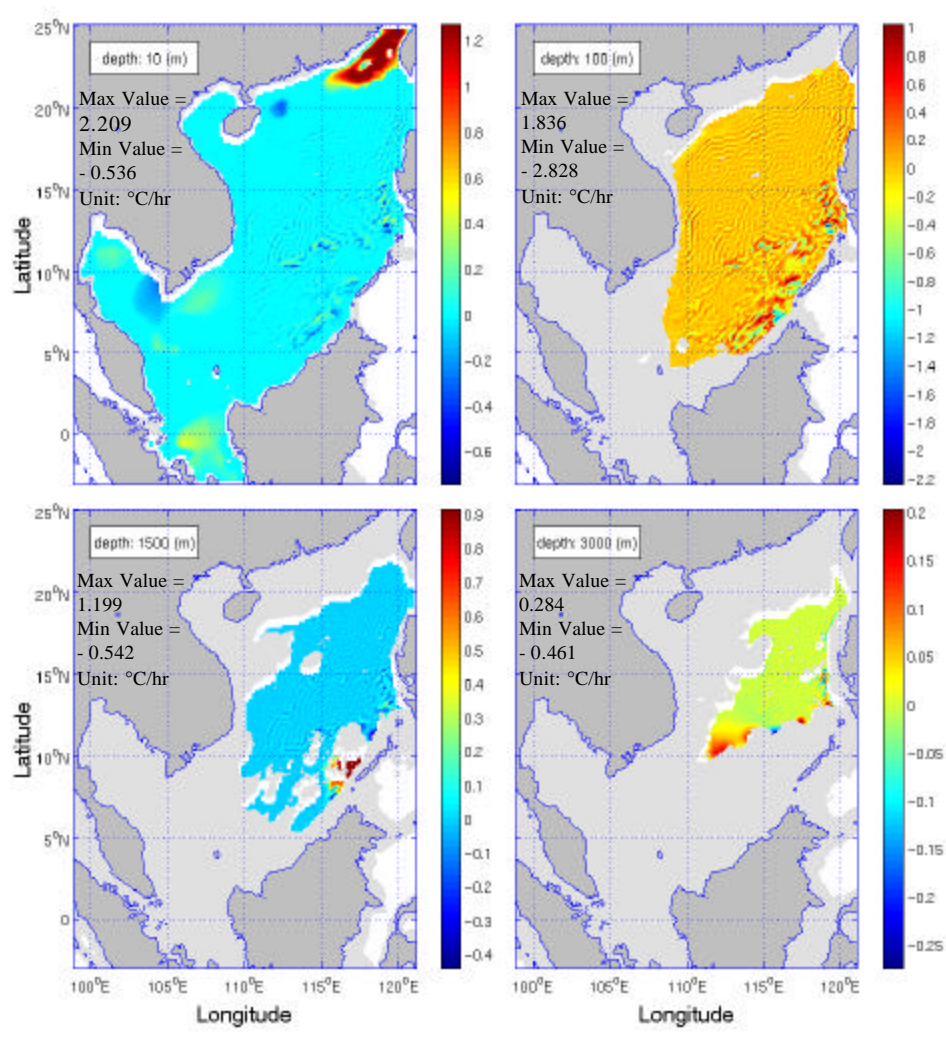


Figure 11. Horizontal distribution of F_T on day-60 with $C = 0.05$

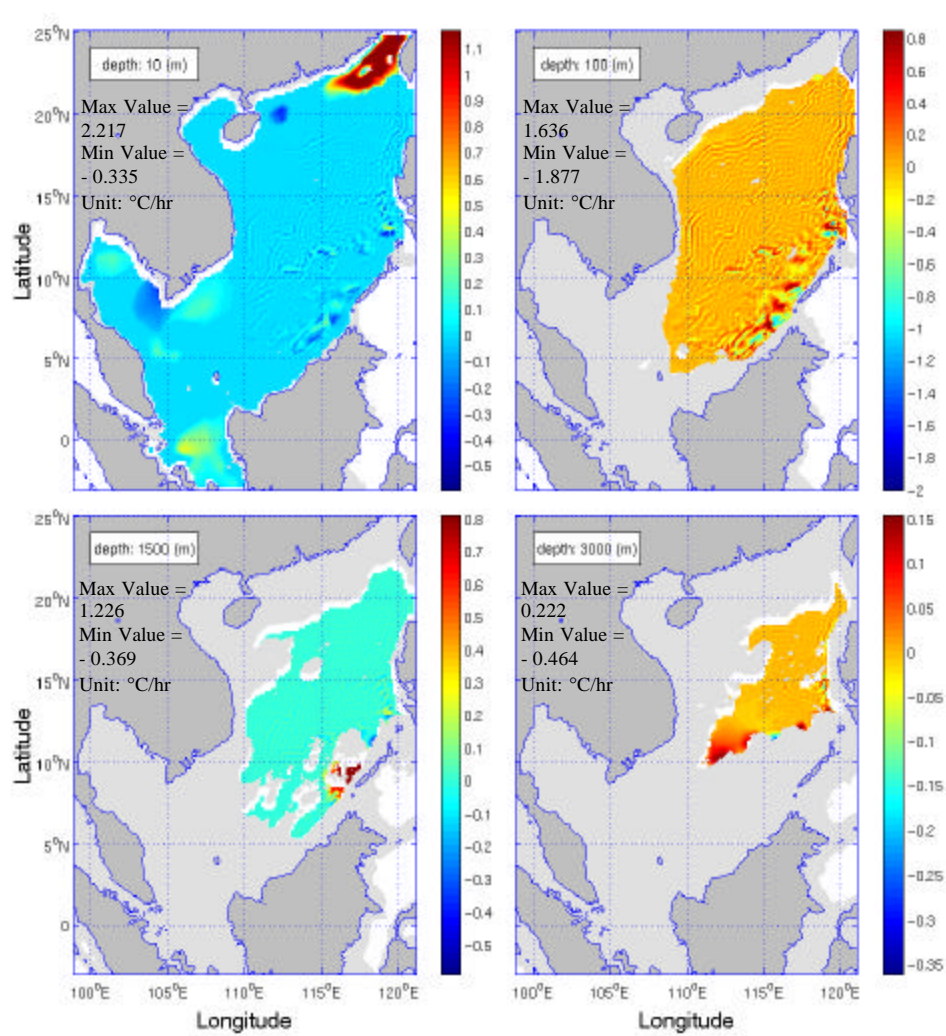


Figure 12. Horizontal distribution of F_T on day-60 with $C = 0.1$

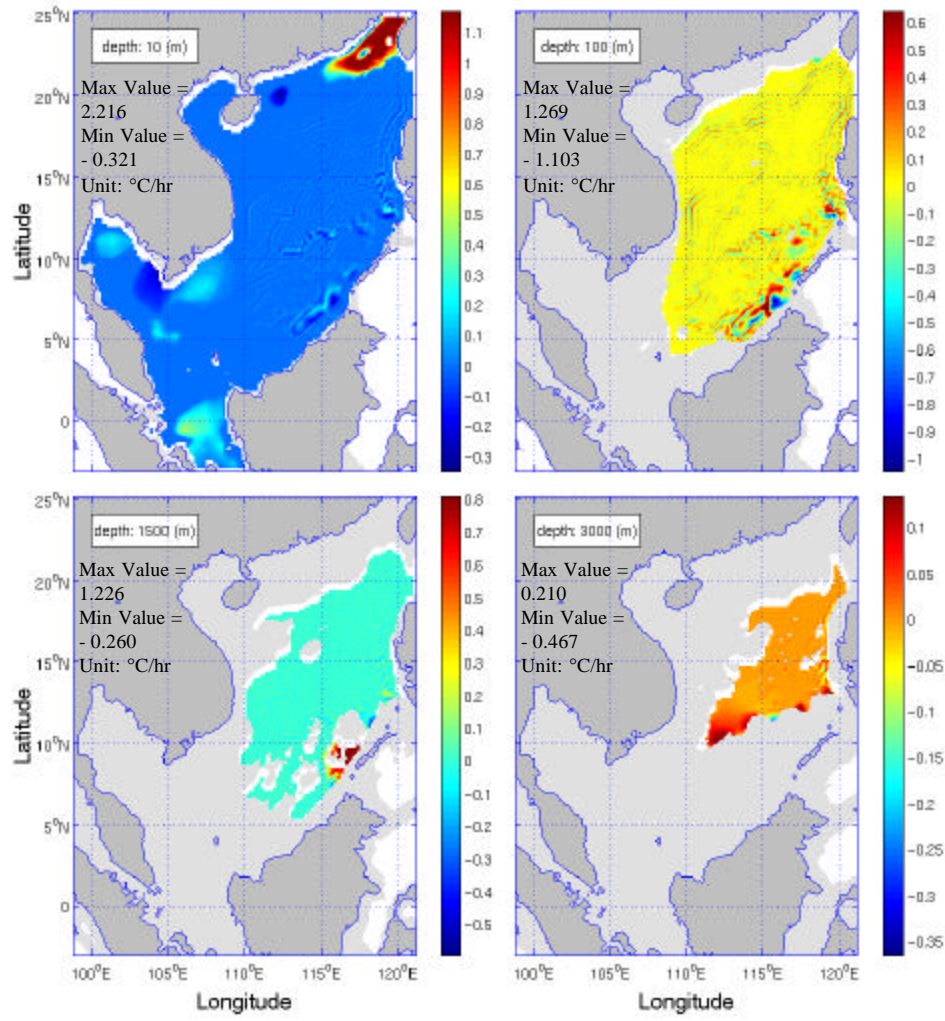


Figure 13. Horizontal distribution of F_T on day-60 with $C = 0.2$

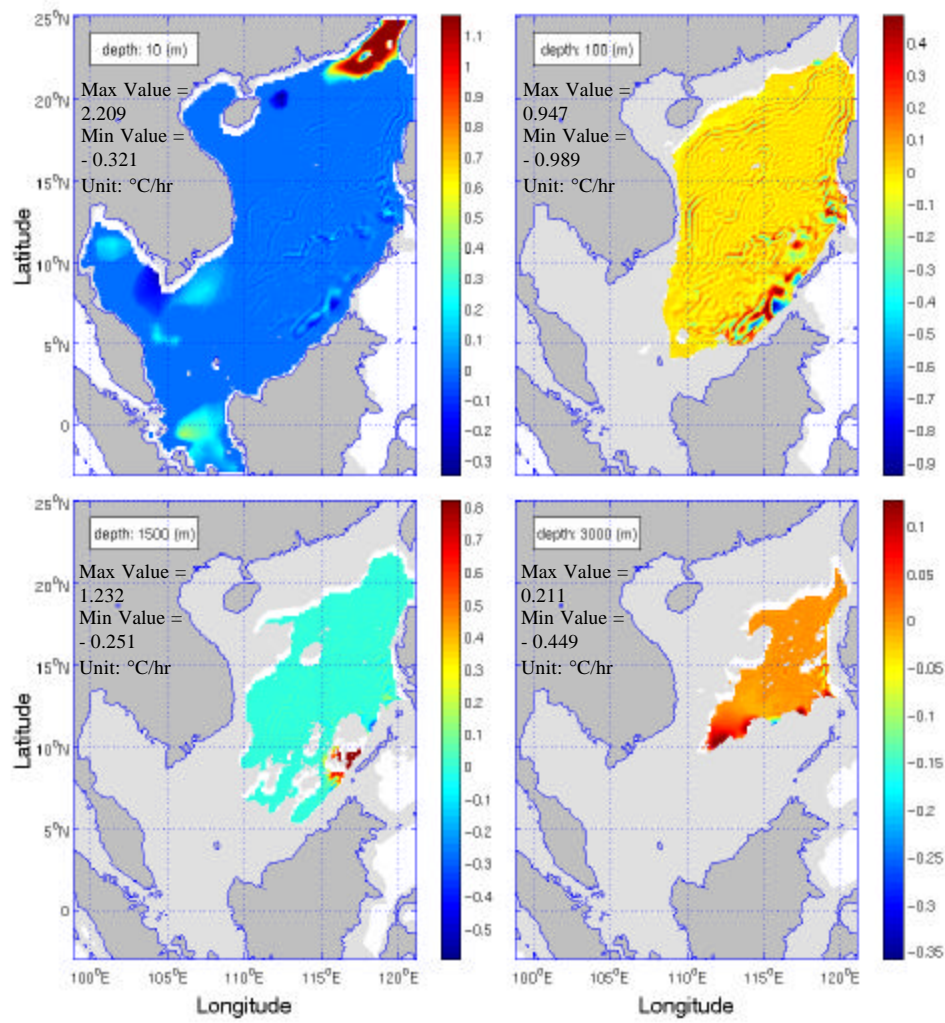


Figure 14. Horizontal distribution of F_T on day-60 with $C = 0.3$

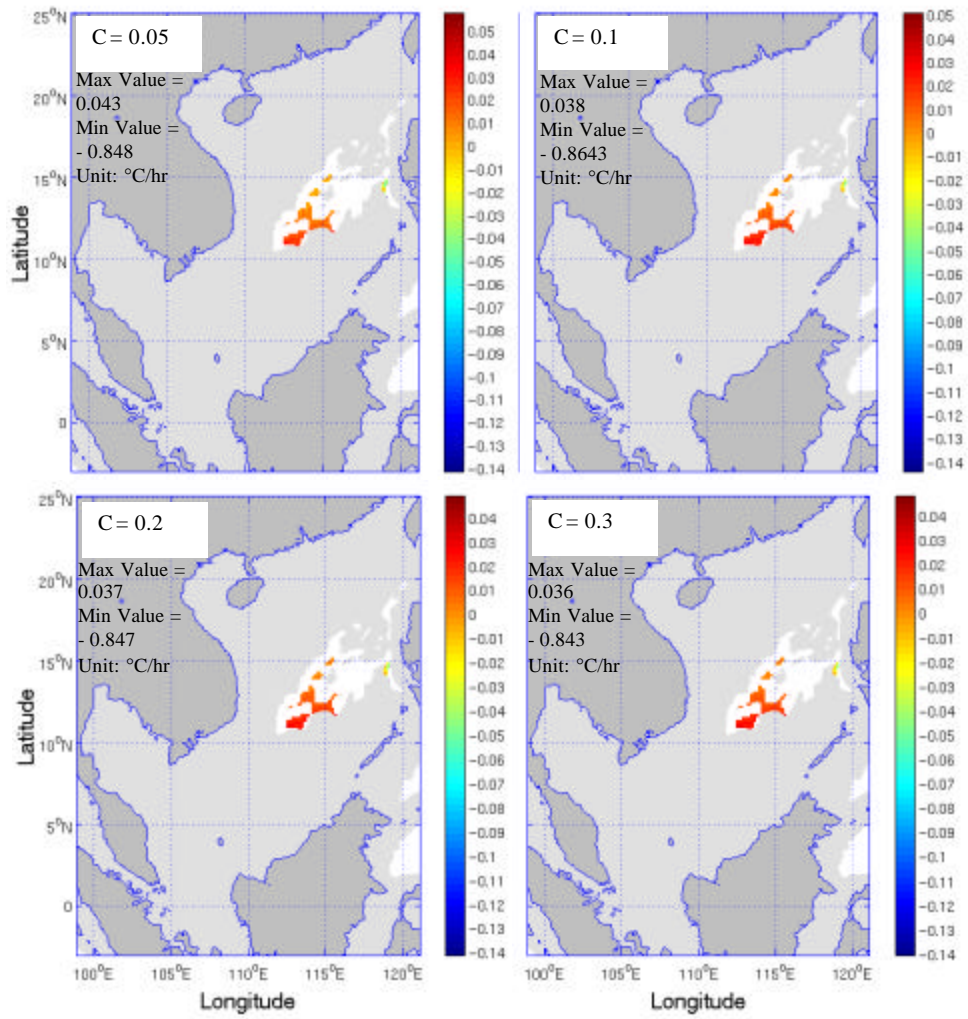


Figure 15. Horizontal distribution of F_T near the bottom of SCS (- 4000m) on day-60 with different C -values

B. HORIZONTAL DISTRIBUTION OF SALT SOURCE/SINK TERMS

The criteria (11) and (12) are used to measure the strength of the non-physical (artificially created) salt ‘source/sink’ terms. The horizontal distributions of F_s (ppt hr⁻¹) generated by the diagnostic initialization at the four levels (near surface, subsurface, mid-level and near bottom) with four different C -values show the existence of strong and extremely strong salt sources/sinks.

The non-physical salt sources/sinks have various scales and strengths. They reveal small- to meso-scale patterns from the surface to the bottom of the SCS. Near the surface, there are also some large-scale patterns (Figure 16 to 19). Near the surface (-10 m) of Taiwan Strait, there is an extremely strong salinity source present in a large-scale pattern. At this location, the maximum time rate of salinity change is 0.422 ppt hr⁻¹ which is greater than the extremely strong salinity criterion (12) when $C = 0.1$. Isolated strong salinity source (meso-scale pattern) are also present near the surface of Gasper and Karimata Straits, southeast of Vietnam and Gulf of Thailand. These features are similar for the four different C -values but in general the magnitude of the salt sources decreases when C increases.

The strongest salt sink is located at the subsurface of Taiwan Strait. At this location, the strong salt sink reached a value of -0.162 ppt hr⁻¹ with $C = 0.2$ and 0.3 . Strong salt sinks in meso-scale pattern also present at the surface of Gasper and Karimata Straits. From the subsurface (-100 m) to the mid-level (-1500 m), numerous small-scale patterns of strong salt sources and sinks are well mixed and distributed throughout some areas, such as west of Palawan and northwest of Borneo. Near the bottom (-3000 m to -4000 m), the non-physical salt sources and sinks are relatively weak.

In general, when C increases, the strength of the strong salt sources/sinks decreases in magnitude; nevertheless, they are still above the criterion (11) and (12) in some locations of SCS (as shown in Figure 19 when $C = 0.3$). In general, larger C would lead to smaller non-physical salt sources and sinks; however, an excessively large C value could cause unrealistically strong diffusion in the ocean model and could create other adverse consequences to the model results.

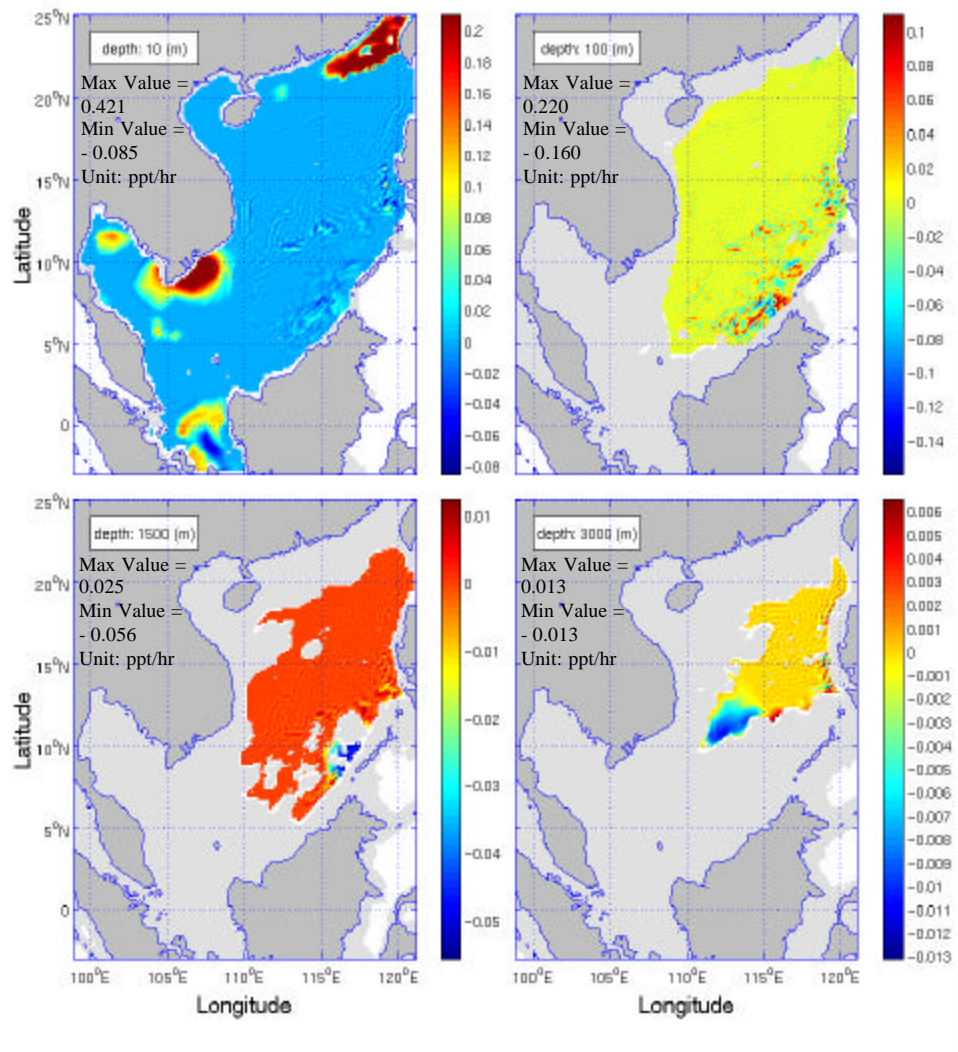


Figure 16. Horizontal distribution of F_s on day-60 with $C = 0.05$

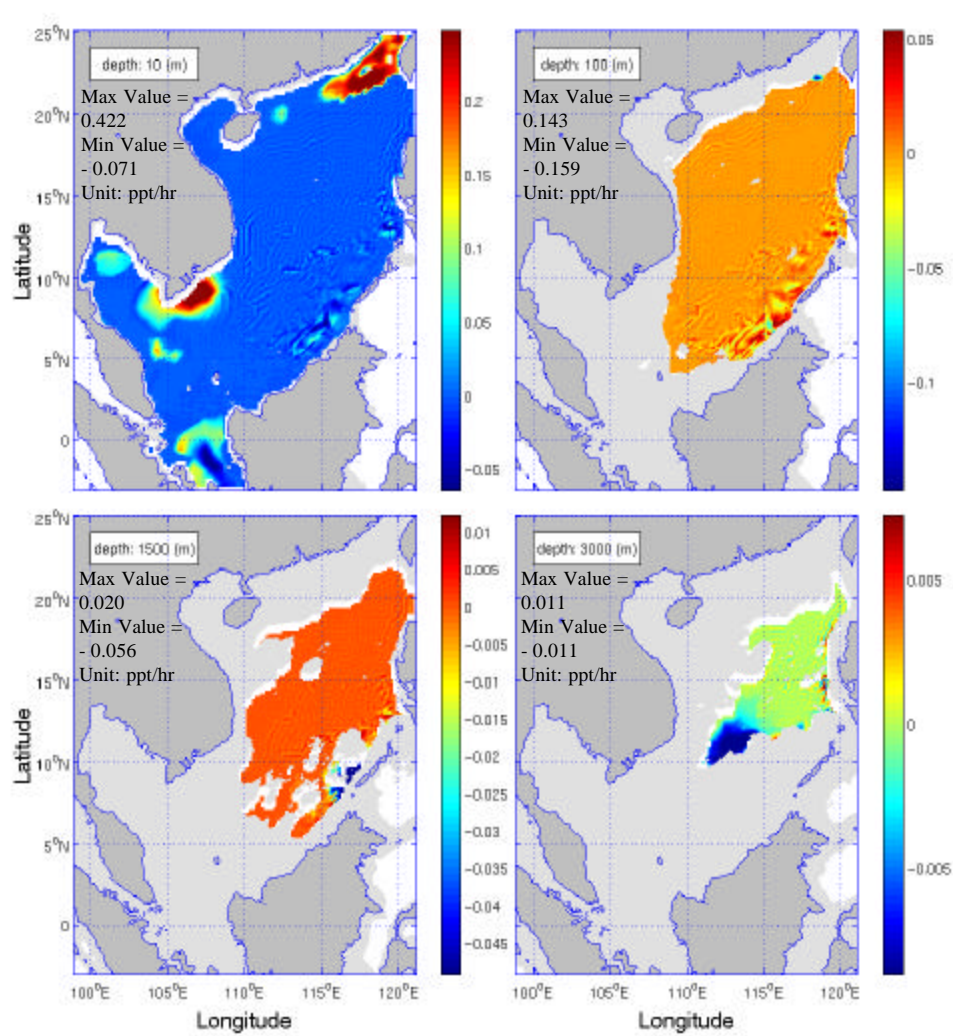


Figure 17. Horizontal distribution of F_S on day-60 with $C = 0.1$

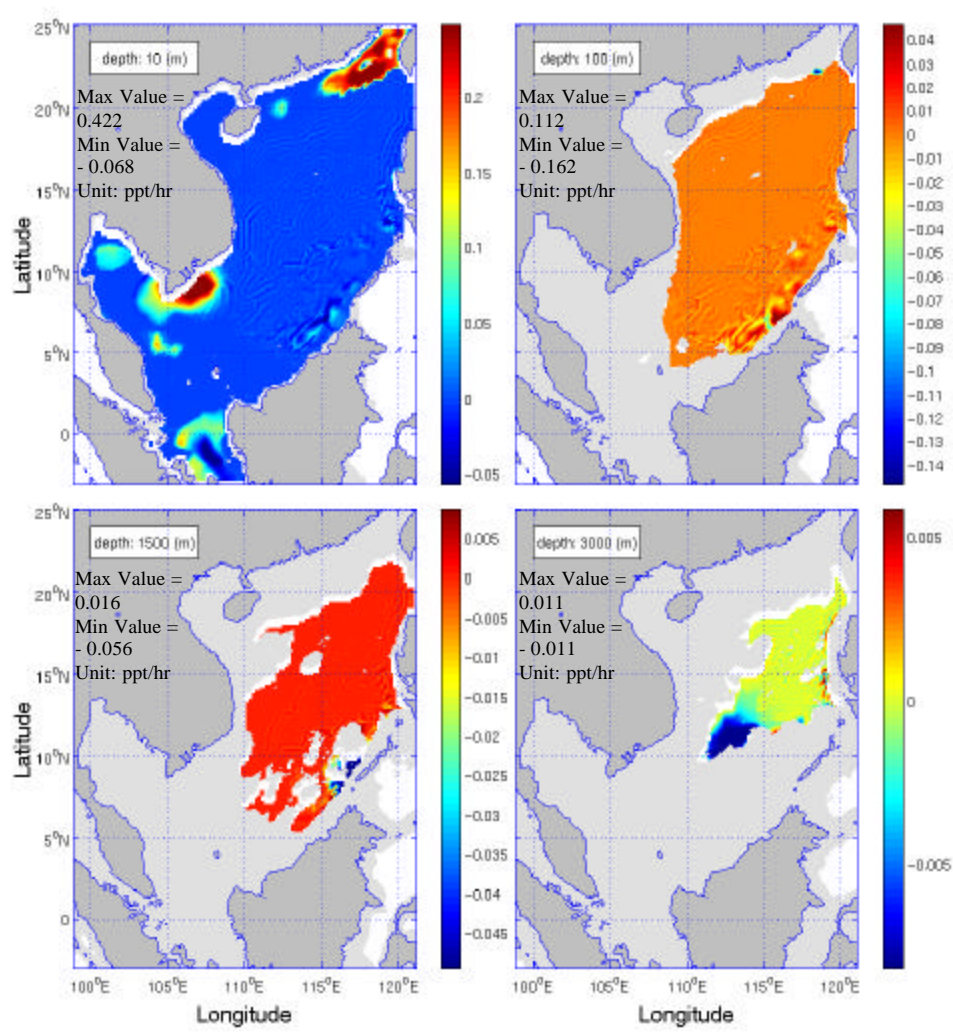


Figure 18. Horizontal distribution of F_S on day-60 with $C = 0.2$

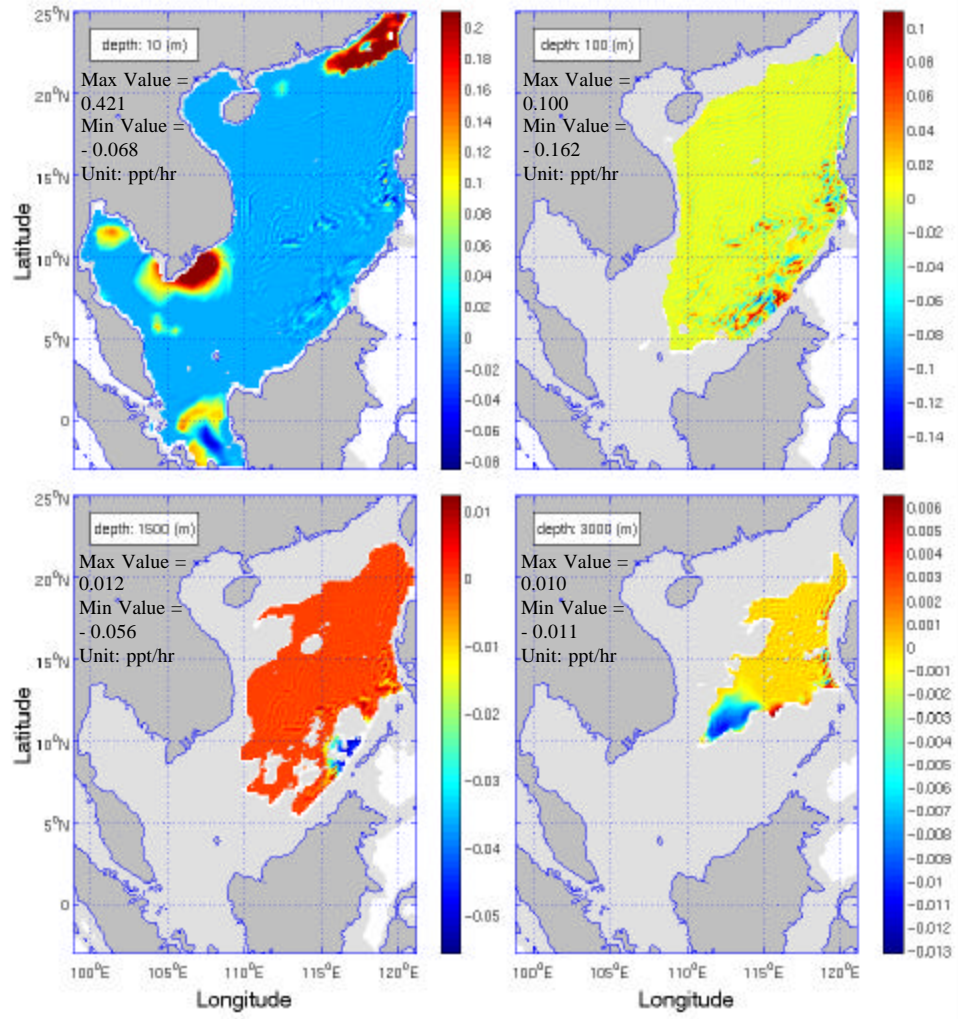


Figure 19. Horizontal distribution of F_S on day-60 with $C = 0.3$

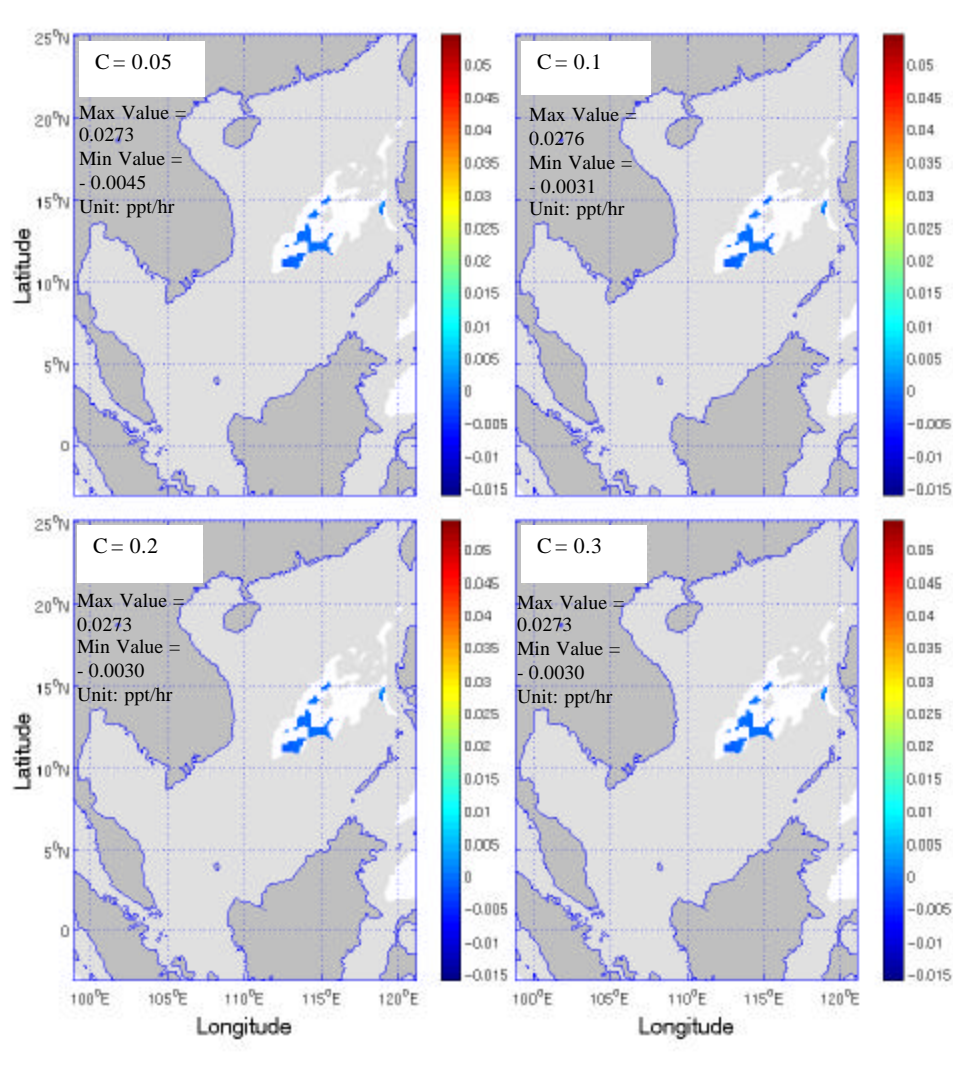


Figure 20. Horizontal distribution of F_s near the bottom of SCS (-4000m) on day-60 with different C -values

C. HORIZONTAL MEAN OF HEAT ‘SOURCE/SINK’ TERM ($M_{\mathcal{S}}(|F_T|)$)

The horizontal mean $|F_T|$ on the \mathcal{S} level with N grid points is calculated by

$$M_{\mathcal{S}}(|F_T|) = \frac{1}{N} \sum_{j=1}^N |F_T^j| \quad (17)$$

$M_{\mathcal{S}}(|F_T|)$ is used to identify the overall strength of the heat source/sink terms generated in the diagnostic initiation process. Figures 21 to 24 show the temporal evolution of $M_{\mathcal{S}}(|F_T|)$ at four different \mathcal{S} levels: near surface ($\mathcal{S} = -0.0125$), subsurface ($\mathcal{S} = -0.15$), mid-level ($\mathcal{S} = -0.5$) and near bottom ($\mathcal{S} = -0.95$) at different C -values.

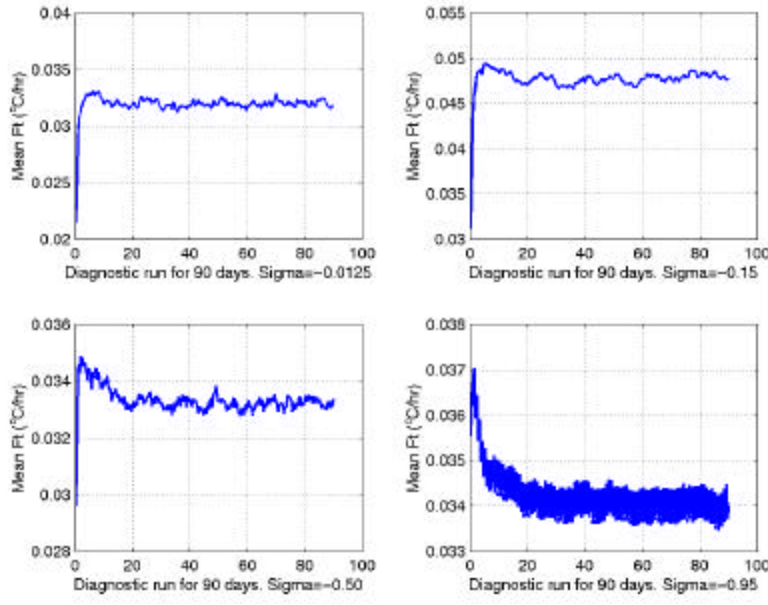


Figure 21. Temporal evolution of $M_{\mathcal{S}}(|F_T|)$ at four different \mathcal{S} levels with $C = 0.05$

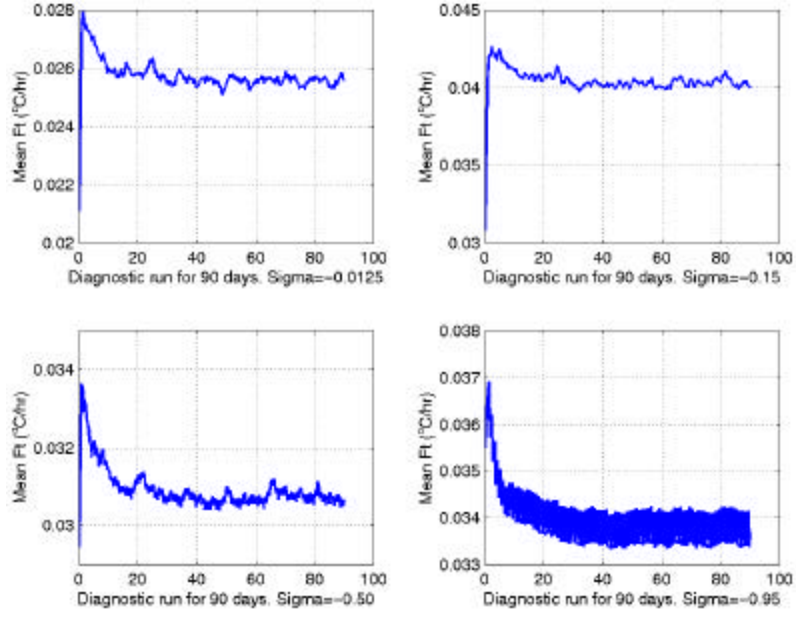


Figure 22. Temporal evolution of $M_{\mathbf{S}}(|F_T|)$ at four different \mathbf{S} levels with $C = 0.1$

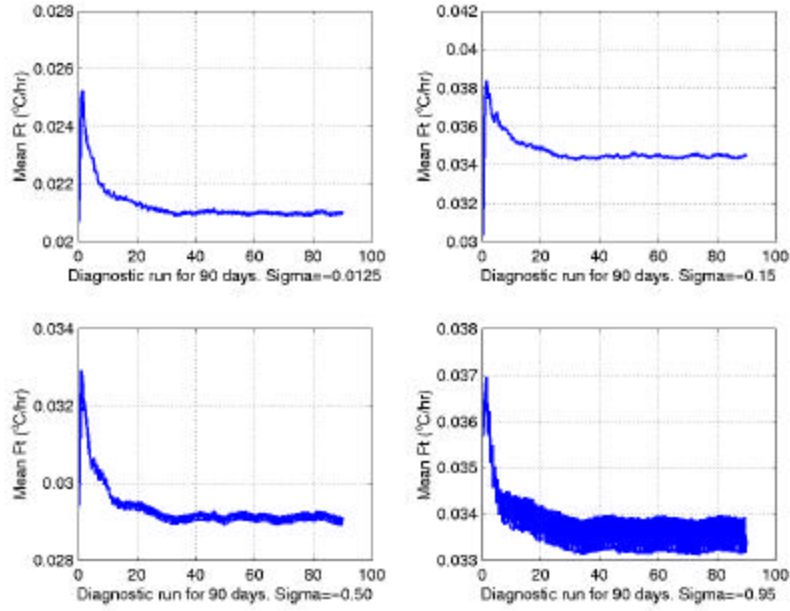


Figure 23. Temporal evolution of $M_{\mathbf{S}}(|F_T|)$ at four different \mathbf{S} levels with $C = 0.2$

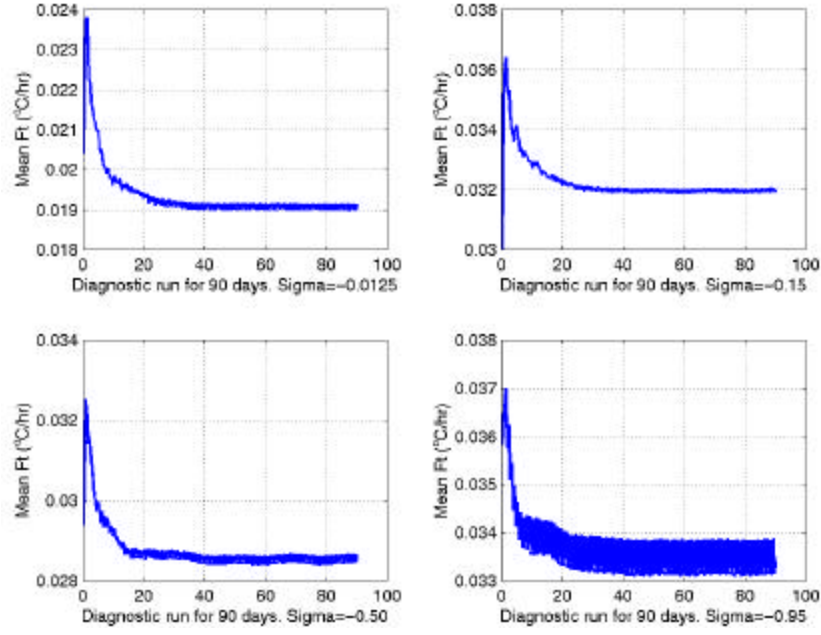


Figure 24. Temporal evolution of $M_s(|F_T|)$ at four different σ levels with $C = 0.3$

In general, the strength of the absolute mean source/sink decreases across the corresponding level when C increases. However, for different C -values, the maximum and minimum values of $M_s(|F_T|)$ occurred at different levels. When $C = 0.05$, the surface $M_s(|F_T|)$ increases with time rapidly in the first 5-10 days to reach a peak value of $0.033 \text{ } ^\circ\text{C hr}^{-1}$ and then dips slightly to $0.032 \text{ } ^\circ\text{C hr}^{-1}$. It then oscillates around quasi-stationary value ($0.032 \text{ } ^\circ\text{C hr}^{-1}$) on the 20th day onwards. At the subsurface, $M_s(|F_T|)$ behaves similar to that at the surface but reaches a higher maximum value of $0.05 \text{ } ^\circ\text{C hr}^{-1}$ and a higher quasi-stationary value of $0.0457 \text{ } ^\circ\text{C hr}^{-1}$. At the mid-level, $M_s(|F_T|)$ increases with time rapidly in the first 5-10 days to $0.035 \text{ } ^\circ\text{C hr}^{-1}$ and then decreases to $0.033 \text{ } ^\circ\text{C hr}^{-1}$ on day-20. It then oscillates around $0.033 \text{ } ^\circ\text{C hr}^{-1}$ from day-20 onwards. Near the bottom, $M_s(|F_T|)$ behaves the same way but with a higher maximum value of $0.037 \text{ } ^\circ\text{C hr}^{-1}$ and dips to $0.034 \text{ } ^\circ\text{C hr}^{-1}$ on the 20th day and then oscillates around $0.034 \text{ } ^\circ\text{C hr}^{-1}$. $M_s(|F_T|)$ generally increases with time rapidly in the first 5-10 days and then oscillates around quasi-stationary from day-20 or day-30 onwards for the rest of C -values

($C = 0.1, 0.2$ and 0.3). For $C = 0.2$, the surface $M_S(|F_T|)$ increases to $0.025\text{ }^{\circ}\text{C hr}^{-1}$ in the first 5-10 days, then oscillates with decreasing amplitudes until day-30 and finally oscillates around $0.021\text{ }^{\circ}\text{C hr}^{-1}$ with small amplitudes. The fluctuation patterns from subsurface to near bottom are similar to that at the surface except with different maximum and quasi-stationary values. These peak values and quasi-stationary values are considered large as they represent the average over the entire S level.

From the depth profile plots of $M_S(|F_T|)$ on the 30th day, 45th day, 60th day and 90th day shown in Figures 25 to 28, when $C = 0.05$ (Figure 25), the quasi-stationary $M_S(|F_T|)$ has a maximum value at the subsurface (near $S = -0.25$) which corresponds to a maximum heating rate at the subsurface. The minimum $M_S(|F_T|)$ is at the mid-level (near $S = -0.55$). When $C = 0.1$ (Figure 26), the quasi-stationary also $M_S(|F_T|)$ has a maximum value at the subsurface (near $S = -0.25$) but the minimum value occurred at the surface (near $S = -0.0125$). Bigger value at the subsurface indicates a greater spurious heat sources and sinks problem at this level. However, when $C = 0.2$ and 0.3 , maximum $M_S(|F_T|)$ occurred near to the bottom at $S = -0.85$ (Figures 27 and 28). Bigger value near the bottom indicates a greater heat sources and sinks problem at this level. The minimum $M_S(|F_T|)$ occurred near the surface.

From the sensitivity experiments conducted with four different C -values, the smallest quasi-stationary value of $M_S(|F_T|)$ is $0.019\text{ }^{\circ}\text{C hr}^{-1}$ which is near the SCS surface and it occurred when $C = 0.3$ (Figure 28). The maximum quasi-stationary value of $M_S(|F_T|)$ is $0.05\text{ }^{\circ}\text{C hr}^{-1}$ and it occurred at the subsurface of SCS when $C = 0.05$ (Figure 25).

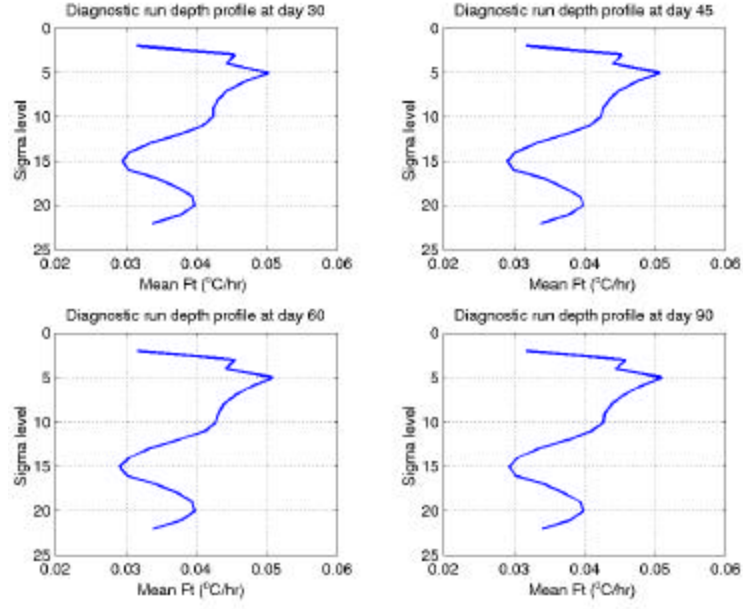


Figure 25. Depth profiles of $M_S(|F_T|)$ with $C = 0.05$

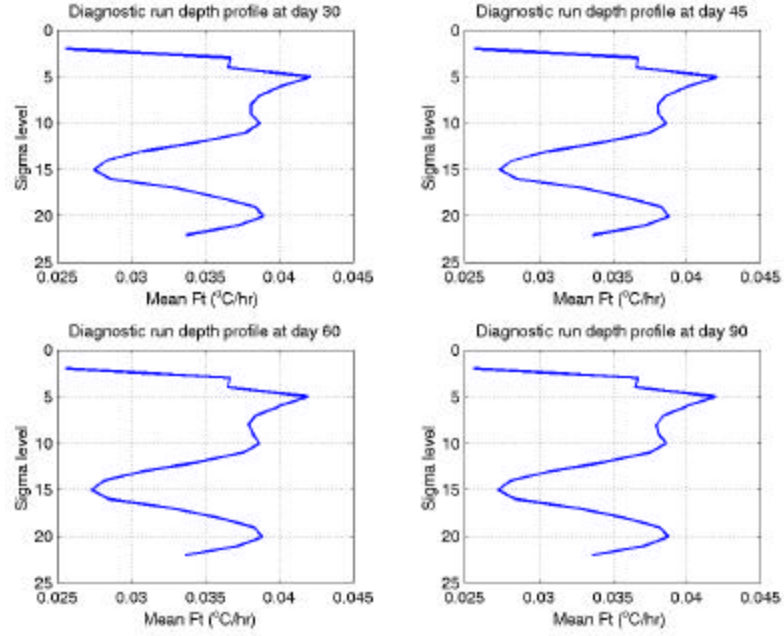


Figure 26. Depth profiles of $M_S(|F_T|)$ with $C = 0.1$

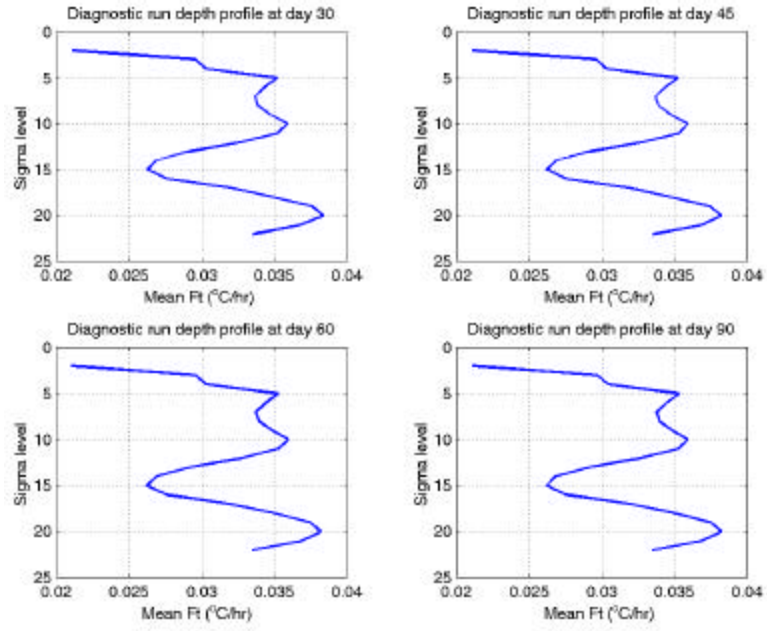


Figure 27. Depth profiles of $M_S(|F_T|)$ with $C=0.2$

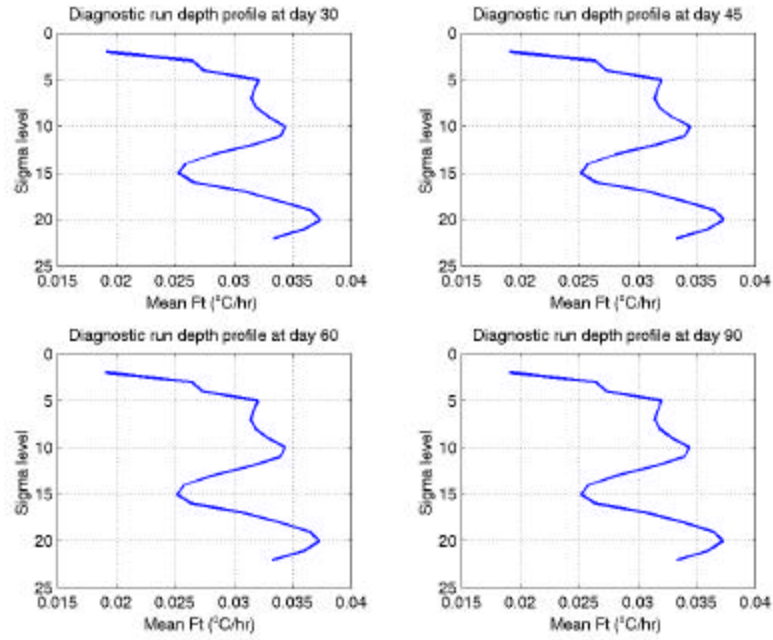


Figure 28. Depth profiles of $M_S(|F_T|)$ with $C=0.3$

D. HORIZONTAL MEAN OF SALT ‘SOURCE/SINK’ TERM ($M_{\mathbf{s}}(|F_S|)$)

Based on (9) derived in Chapter I, the horizontal mean $|F_S|$ on the \mathbf{s} level is calculated by

$$M_{\mathbf{s}}(|F_S|) = \frac{1}{N} \sum_{j=1}^N |F_S^j|, \quad (19)$$

This is used to identify the overall strength of the salt source/sink terms. Figures 29 to 32 show the temporal evolution of $M_{\mathbf{s}}(|F_S|)$ at four different \mathbf{s} levels: near surface ($\mathbf{s} = -0.0125$), subsurface ($\mathbf{s} = -0.15$), mid-level ($\mathbf{s} = -0.5$) and near bottom ($\mathbf{s} = -0.95$) at different C -values. $M_{\mathbf{s}}(|F_S|)$ increases with time rapidly in the first 5-10 days and then oscillates around quasi-stationary values for the difference cases of C -values. In general, the strength of the absolute mean source/sink decreases across the corresponding level when C increases.

When $C = 0.05$, $M_{\mathbf{s}}(|F_S|)$ increases with time rapidly in the first 5-10 days to reach a peak value of $0.0137 \text{ ppt hr}^{-1}$ (surface) and then dips slightly to oscillate around quasi-stationary values on the 20th day at around $0.0135 \text{ ppt hr}^{-1}$. At the subsurface, $M_{\mathbf{s}}(|F_S|)$ again increases with time rapidly in the first 5-10 days to a lower maximum ($0.0071 \text{ ppt hr}^{-1}$) and then decreases to $0.0068 \text{ ppt hr}^{-1}$ on day-30. It then oscillates around $0.0068 \text{ ppt hr}^{-1}$ from day-30 onwards. At the mid-level and near the bottom, $M_{\mathbf{s}}(|F_S|)$ behaves similar to that at the surface and subsurface but with a lower maximum value and a lower quasi-stationary value. When $C = 0.1, 0.2$ and 0.3 , $M_{\mathbf{s}}(|F_S|)$ behaves similar to that of $C = 0.05$ but the maximum value and the quasi-stationary values decrease when C increases across the corresponding \mathbf{s} level (See Figures 29 to 32).

From the depth profile plots of $M_{\mathbf{s}}(|F_S|)$ on the 30th day, 45th day, 60th day and 90th day shown in Figures 33 to 36, when $C = 0.05$ (Figure 33), the quasi-stationary $M_{\mathbf{s}}(|F_S|)$ has a maximum value at the surface (near $\mathbf{s} = -0.0125$) which indicates a greater artificial salt source/sink problem near the surface. The quasi-steady value of $M_{\mathbf{s}}(|F_S|)$ decreases as the depth increases. The minimum value of $M_{\mathbf{s}}(|F_S|)$ occurred at the bottom for all the four cases of C -values. The smallest quasi-steady value of

$M_S(|F_S|)$ is $0.005 \text{ ppt hr}^{-1}$ near the SCS bottom and it occurs when $C = 0.3$ (Figure 36). The maximum quasi-steady of $M_S(|F_S|)$ is $0.0135 \text{ ppt hr}^{-1}$ at the surface of SCS when $C = 0.05$ (Figure 29). Bigger $M_S(|F_S|)$ at the surface indicates a more serious spurious salt sources and sinks problem at this level.

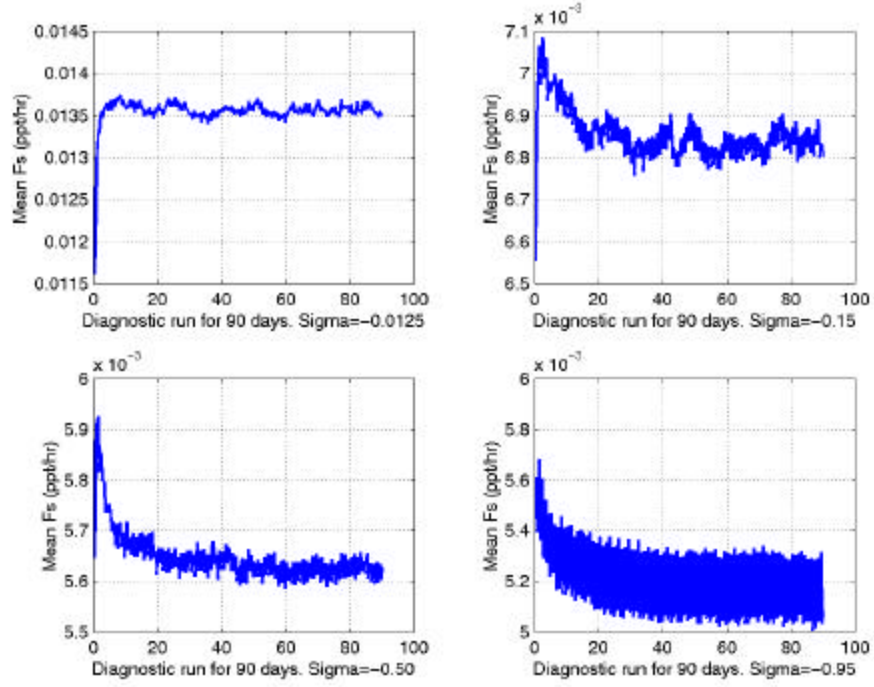


Figure 29. Temporal evolution of $M_S(|F_S|)$ at four different σ levels with $C = 0.05$

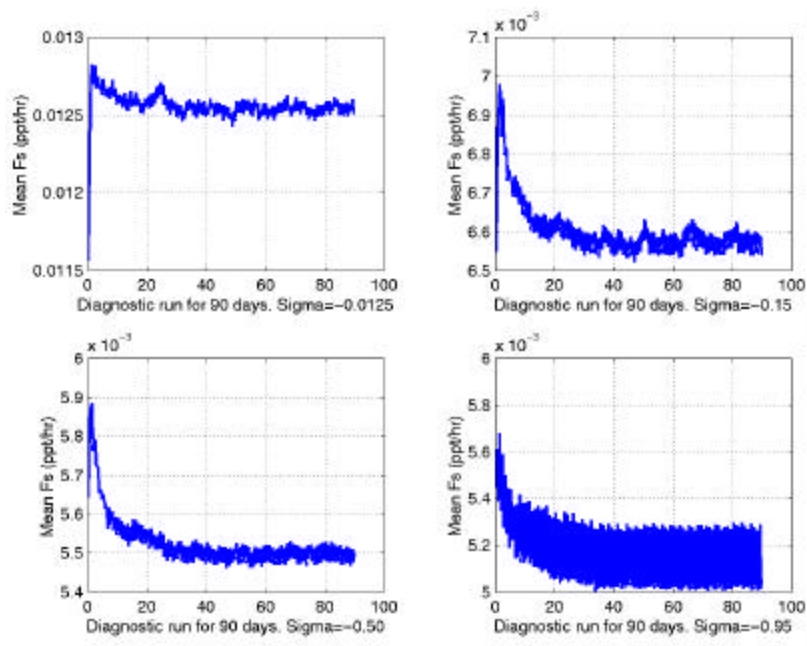


Figure 30. Temporal evolution of $M_{\mathcal{S}}(|F_{\mathcal{S}}|)$ at four different \mathcal{S} levels with $C = 0.1$

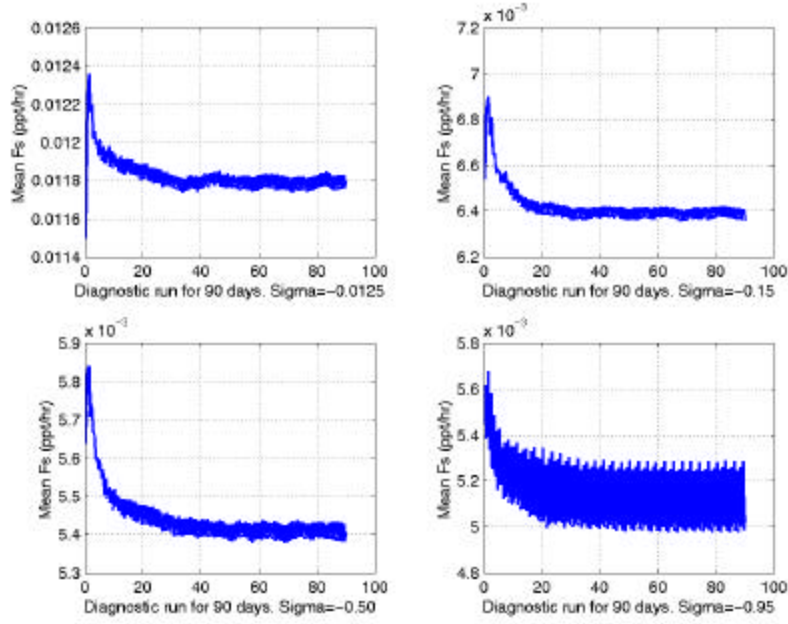


Figure 31. Temporal evolution of $M_{\mathcal{S}}(|F_{\mathcal{S}}|)$ at four different \mathcal{S} levels with $C = 0.2$

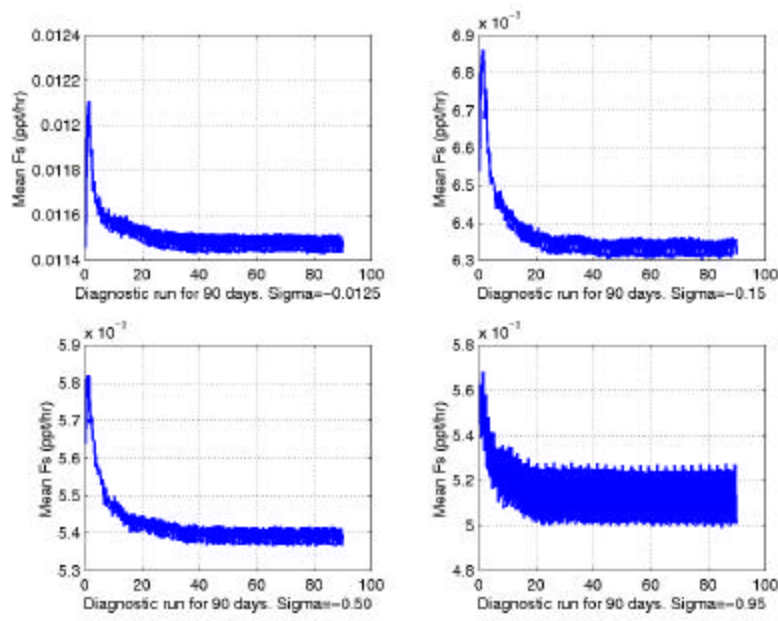


Figure 32. Temporal evolution of $M_s(|F_s|)$ at four different σ levels with $C = 0.3$

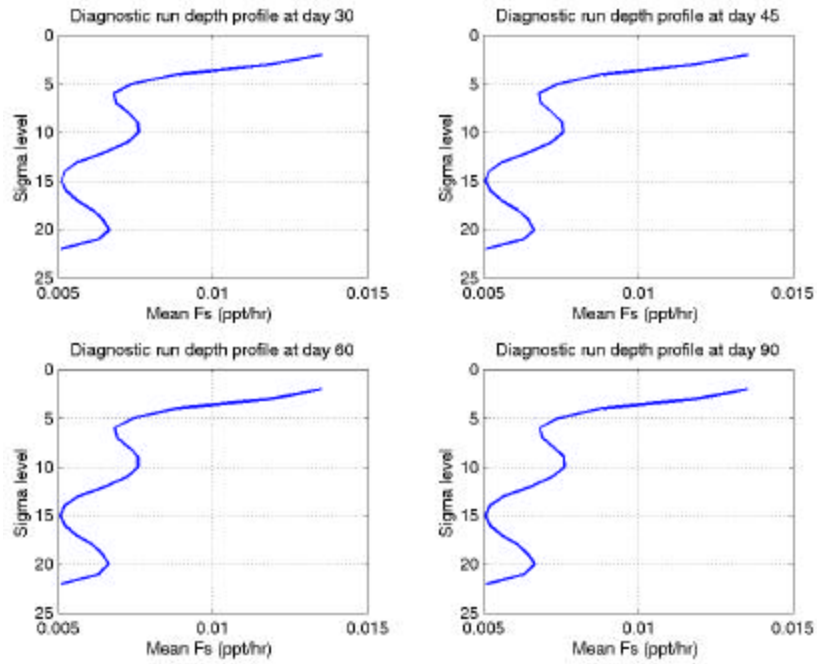


Figure 33. Depth profiles of $M_s(|F_s|)$ with $C = 0.05$

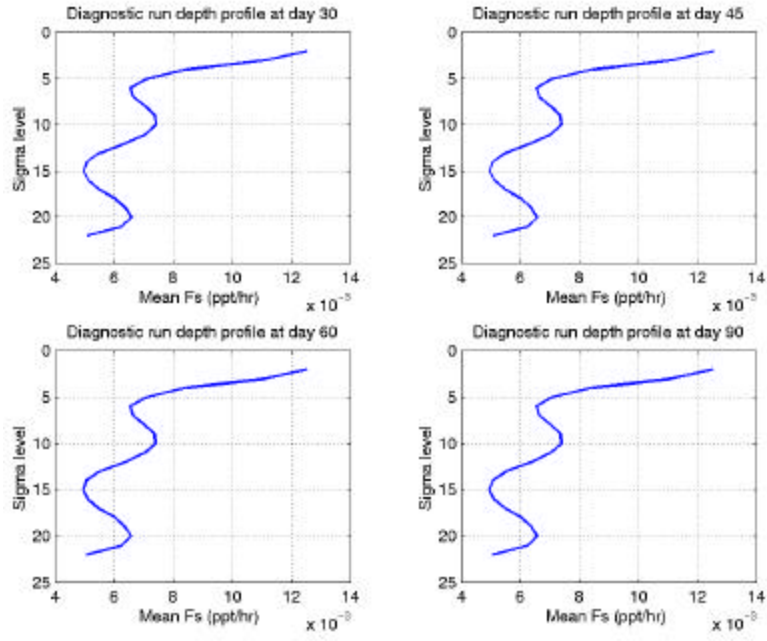


Figure 34. Depth profiles of $M_S(|F_S|)$ with $C=0.1$

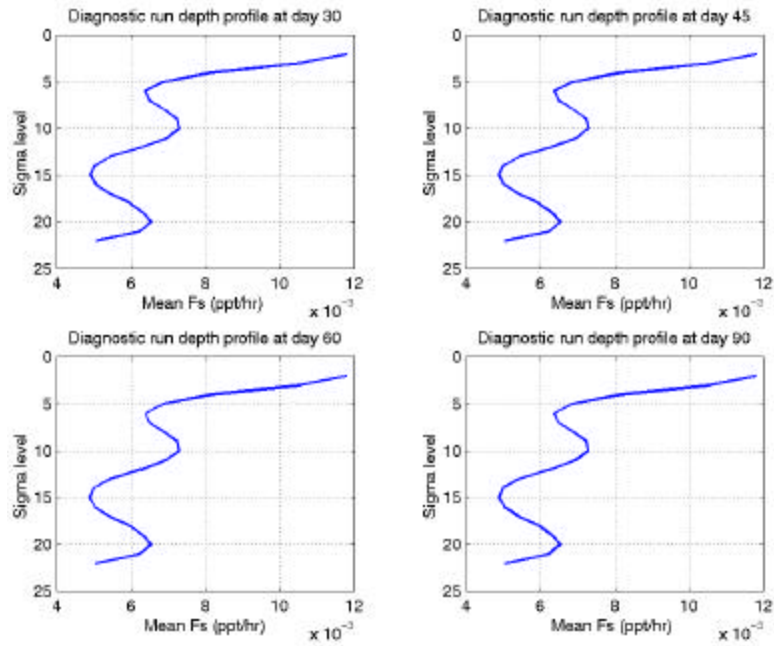


Figure 35. Depth profiles of $M_S(|F_S|)$ with $C=0.2$

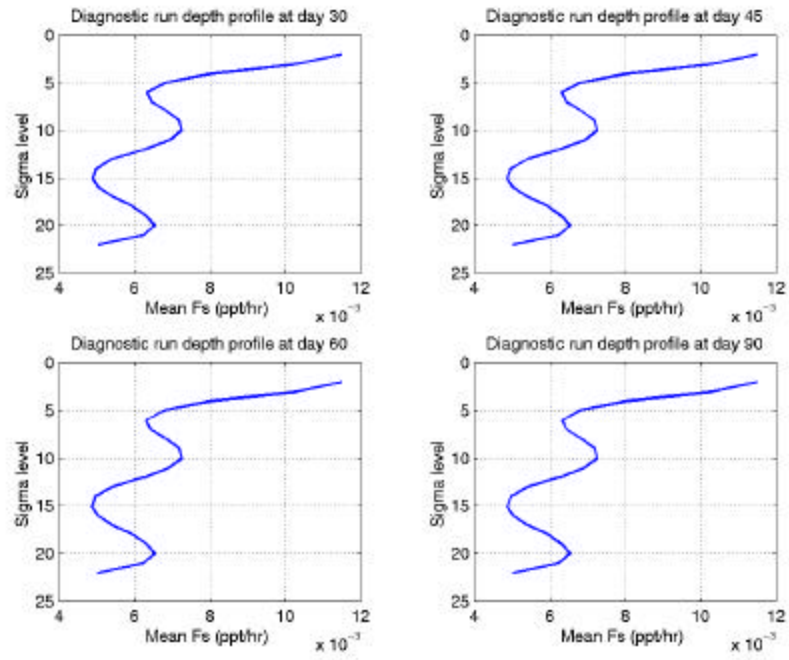


Figure 36. Depth profiles of $M_S(F_S)$ with $C=0.3$

V. UNCERTAINTY OF THE DIAGNOSTICALLY INITIALIZED VELOCITY FIELD DUE TO THE UNCERTAIN HORIZONTAL VISCOSITY

A. HORIZONTAL VELOCITIES ON DAY-60 OF THE DIAGNOSTIC INITIALIZATION

The horizontal velocities on the 60th day of the diagnostic initialization for the 4 levels (near surface, subsurface, mid-level and near bottom) for each of the four C -values are shown in Figures 37 to 40. In general, the surface and subsurface SCS circulation heads southward near the east coast of China and Vietnam in an anti-cyclonic pattern for all the four cases of C -values. However, such a velocity field could have a Relative Root Mean Square Difference as large as 60%. This large uncertainty on the velocity fields is shown in the next section. There is also an anti-cyclonic eddy-like structure centered at (14°N, 117°E) which appeared from the surface down to the bottom (- 3000m) of SCS. Near the bottom of SCS, this anti-cyclonic eddy-like structure is more pronounced when C is small ($C = 0.05$) and appeared to be in a random pattern when C increased to 0.3. The anti-cyclonic circulation pattern is contained within the SCS basin and appeared to have no exchange with the open boundaries. This is consistent with the model set-up that there is zero volume transport at the open boundaries.

At the subsurface when $C = 0.05$ and 0.1, there seems to be a strong jet headed towards the northwest coast of Borneo. This phenomenon is not apparent when $C = 0.2$ and 0.3. From the horizontal velocity plots, there is no obvious relationship between the diagnostically initialized velocity field and the C -value.

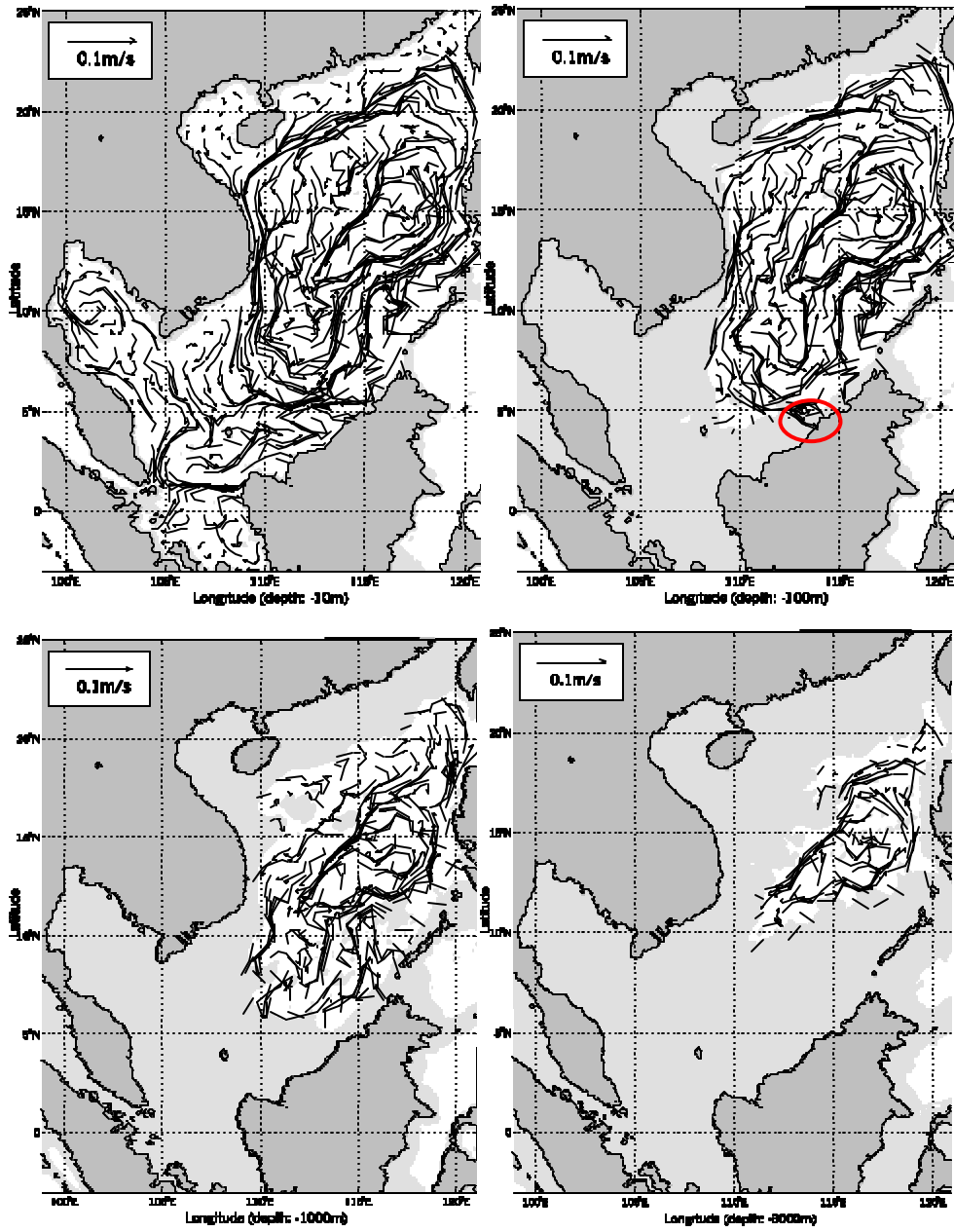


Figure 37. Horizontal velocities on the 60th day ($C=0.05$)

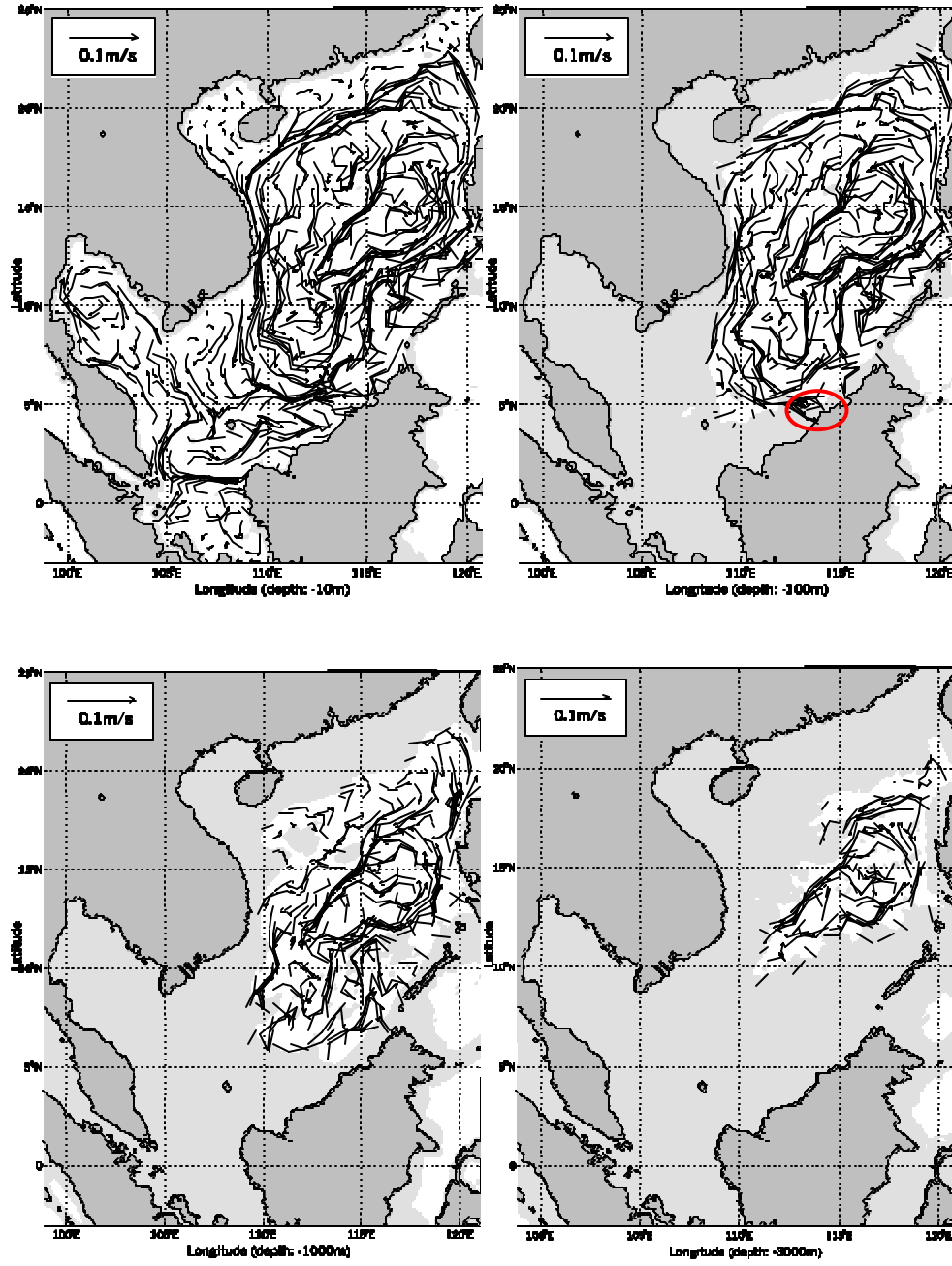


Figure 38. Horizontal velocities on the 60th day ($C=0.1$)

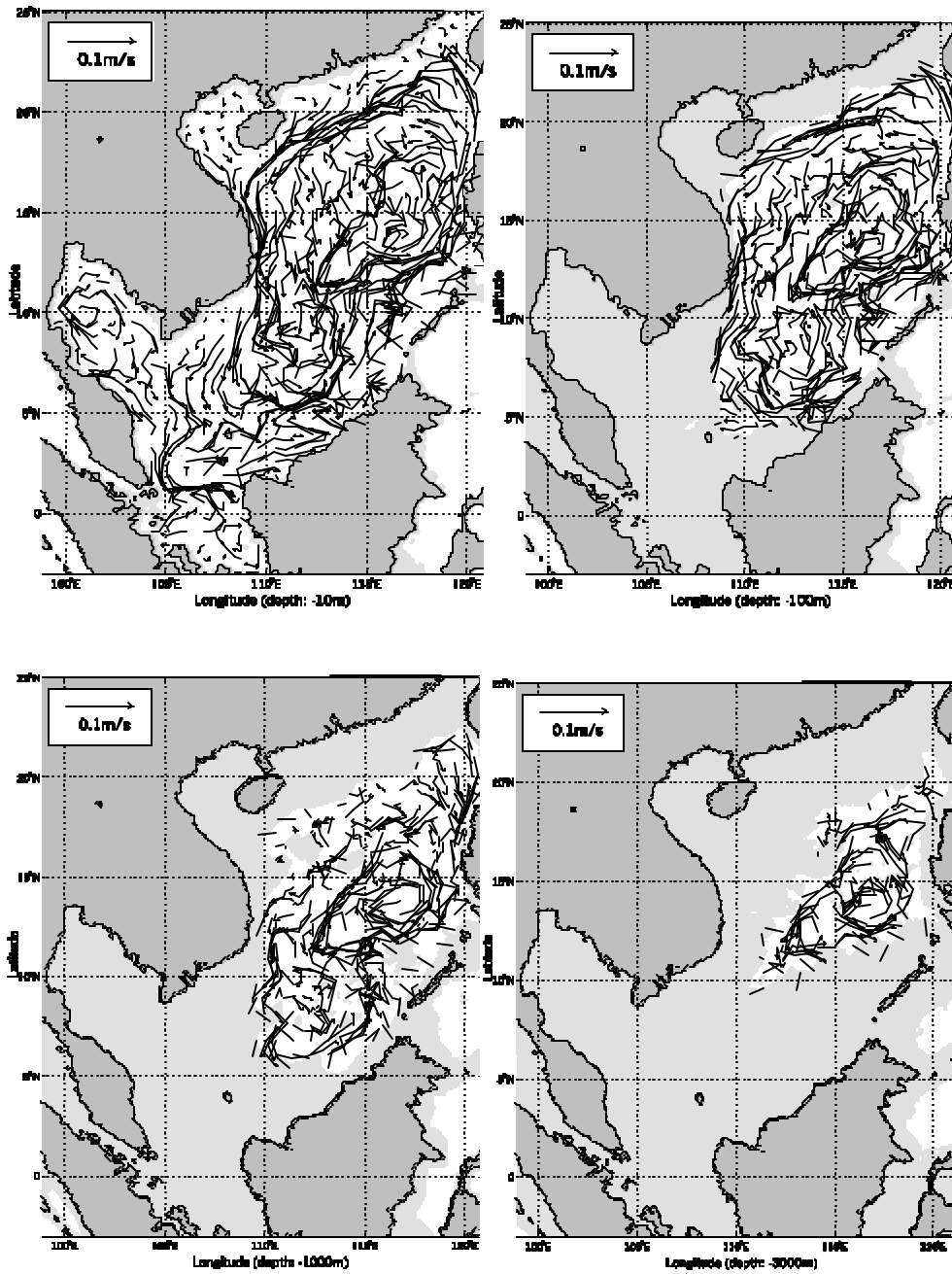


Figure 39. Horizontal velocities on the 60th day ($C = 0.2$)

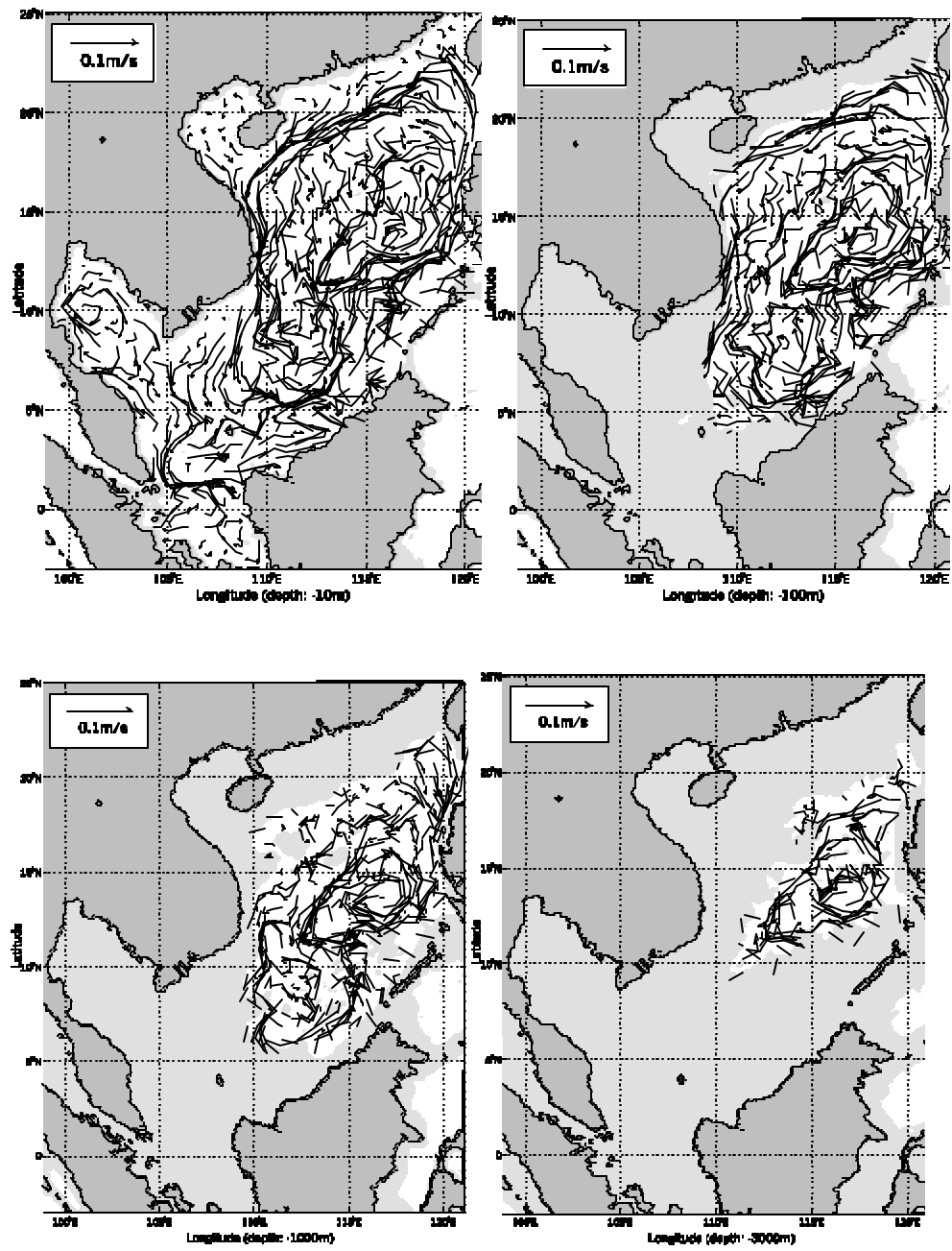


Figure 40. Horizontal velocities on the 60th day ($C = 0.3$)

B. RELATIVE ROOT MEAN SQUARE DIFFERENCE OF VELOCITIES

As highlighted in Chapter IV, one of the objectives is to demonstrate how the uncertainty of C -value affects the velocity field (\mathbf{V}) derived from the diagnostic initiation process. To study the impact caused by the uncertainty of C -values, four different C -values (0.05, 0.1, 0.2 and 0.3) were used in the POM to conduct four numerical experiments. $C = 0.2$ was used as a control run and the depth-dependent Relative Root Mean Square Difference of the horizontal velocity ($RRMSDV$) and of the vertical velocity ($RRMSDW$) between the control run and sensitivity runs ($C = 0.05, 0.1$ and 0.3) were computed,

$$RRMSDV(k, C) = \frac{\sqrt{\sum_{j=1}^{M_y} \sum_{i=1}^{M_x} \left[\left(U_C^{(i,j,k)} - U_{C=0.2}^{(i,j,k)} \right)^2 + \left(V_C^{(i,j,k)} - V_{C=0.2}^{(i,j,k)} \right)^2 \right]}}{\sqrt{\sum_{j=1}^{M_y} \sum_{i=1}^{M_x} \left(U_{C=0.2}^{(i,j,k)} \right)^2 + \left(V_{C=0.2}^{(i,j,k)} \right)^2}} \quad (17)$$

$$RRMSDW(k, C) = \frac{\sqrt{\sum_{j=1}^{M_y} \sum_{i=1}^{M_x} \left[\left(W_C^{(i,j,k)} - W_{C=0.2}^{(i,j,k)} \right)^2 \right]}}{\sqrt{\sum_{j=1}^{M_y} \sum_{i=1}^{M_x} \left(W_{C=0.2}^{(i,j,k)} \right)^2}} \quad (18)$$

where $C = 0.05, 0.1$ or 0.3 . M_x is the number of grid points along the east-west direction and M_y is the number of grid points along the north-south direction for the SCS. $k = 1$ to 23 is the number of σ -level.

Both $RRMSDV(k, C)$ and $RRMSDW(k, C)$ increase with time rapidly in the first 5-10 days and then oscillates around quasi-stationary values for the difference cases of C -values. The largest value is between $C = 0.05$ and $C = 0.2$ (control run). The value of $RRMSDW(k, C)$ is much larger than the value of $RRMSDV(k, C)$ for $C = 0.05, 0.1$ and 0.3 . This could be due to the relatively smaller magnitude and larger uncertainty of the vertical velocity in the SCS. The vertical profile of $RRMSDV(k, C)$ has a maximum value at the mid-level for the different cases of C on day-30, 45, 60 and 90 of the diagnostic run. This feature indicates a strong variation of the horizontal velocity in the mid-level of SCS. The vertical profile of $RRMSDW(k, C)$ decreases from the surface to the bottom

indicates the vertical velocity's variation decreases from the surface to the bottom. There is a decrease in the rate of decrease of $RRMSDW(k, C)$ from the subsurface to the bottom for all the three sensitivity runs ($C = 0.05, 0.1$ and 0.3) when compared with surface to subsurface. Thus, the variation of vertical velocity is expected to be smaller from the subsurface to the bottom when compared with the surface to the subsurface. Both $RRMSDV(k, C)$ and $RRMSDW(k, C)$ for different C values and σ levels are plotted in Figures 41 to 52 for illustration.

Figure 41 shows that $RRMSDV(k, 0.05)$ increases with time rapidly in the first 5 days to reach 0.6. It then oscillates between 0.6 and 0.8 from the surface to the mid-level. Near the SCS bottom, $RRMSDV(k, 0.05)$ oscillates between 0.5 and 0.6. $RRMSDV(k, 0.05)$ decreases with depth from mid-level to the bottom. The values of $RRMSDW(k, 0.05)$ and $RRMSDW(k, 0.1)$ are greater than 1 from the surface to the subsurface. $RRMSDW(k, 0.05)$ decreases to about 0.7 near the bottom (Figure 42). The uncertainty of C -value has a significant effect on the velocity field (\mathbf{V}) derived from the diagnostic initiation process.

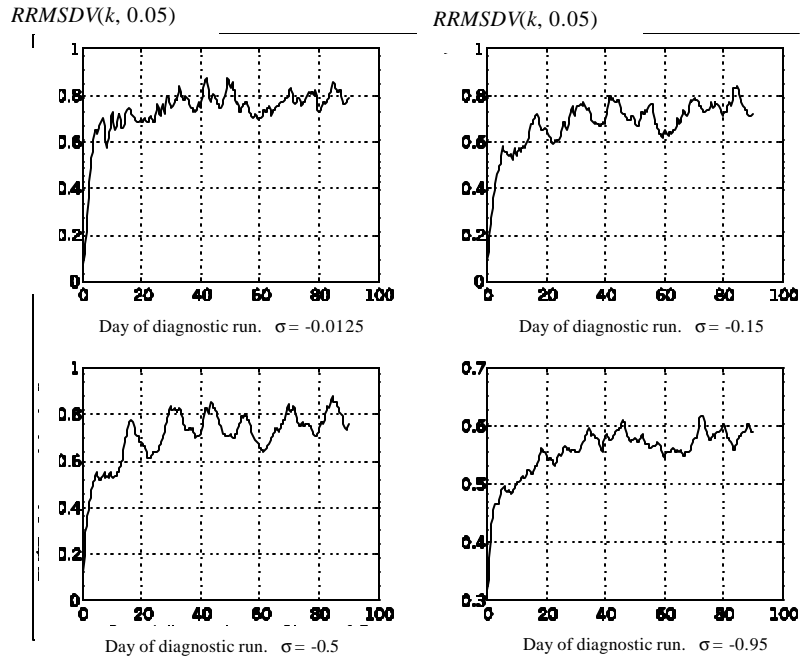


Figure 41. Temporally Varying of $RRMSDV(k, 0.05)$

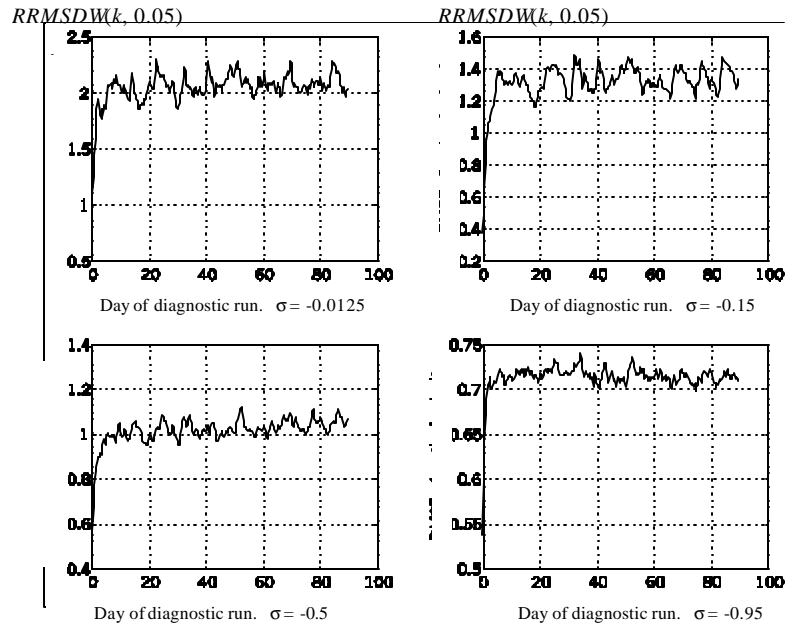


Figure 42. Temporally Varying of $RRMSDW(k, 0.05)$

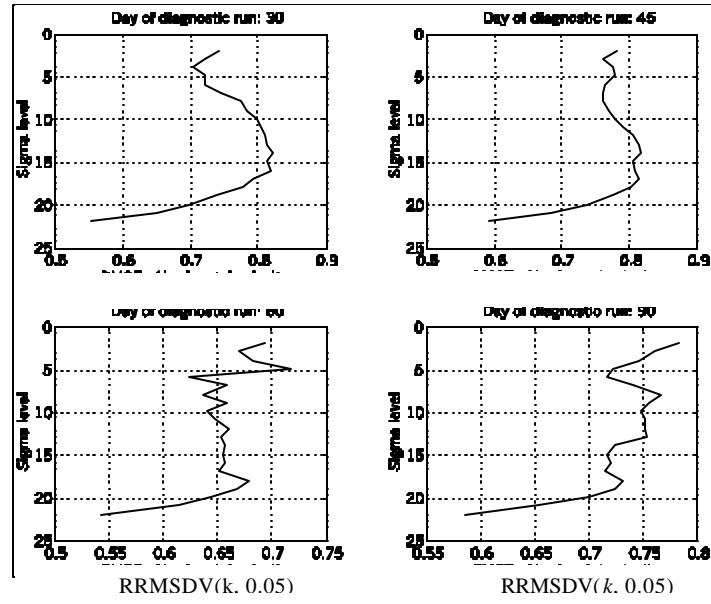


Figure 43. Depth profiles of $RRMSDV(k, 0.05)$ at different day

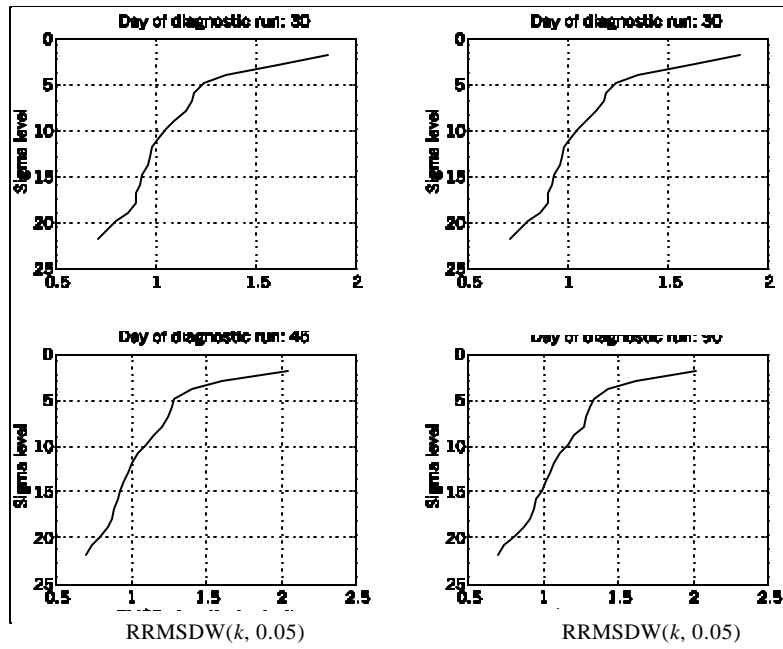


Figure 44. Depth profiles of $RRMSDW(k, 0.05)$ at different day

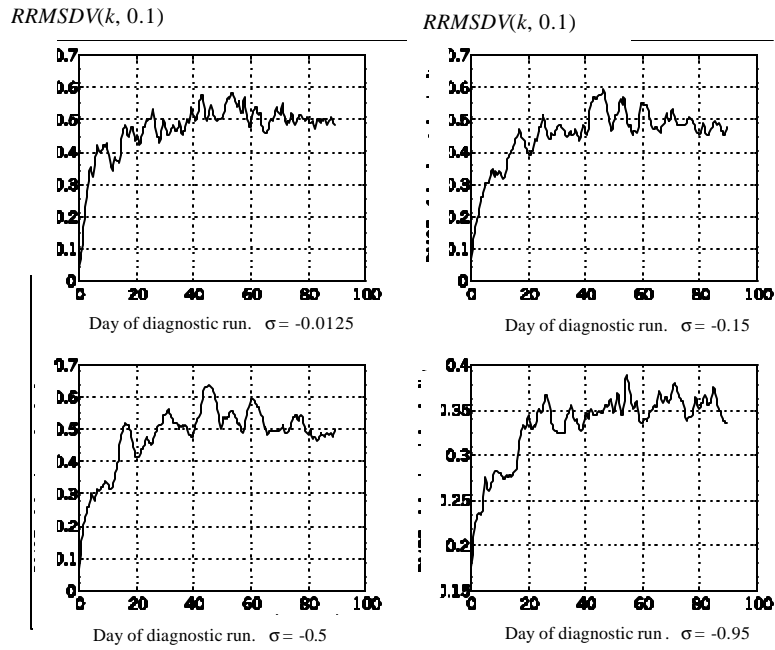


Figure 45. Temporally Varying of $RRMSDV(k, 0.1)$

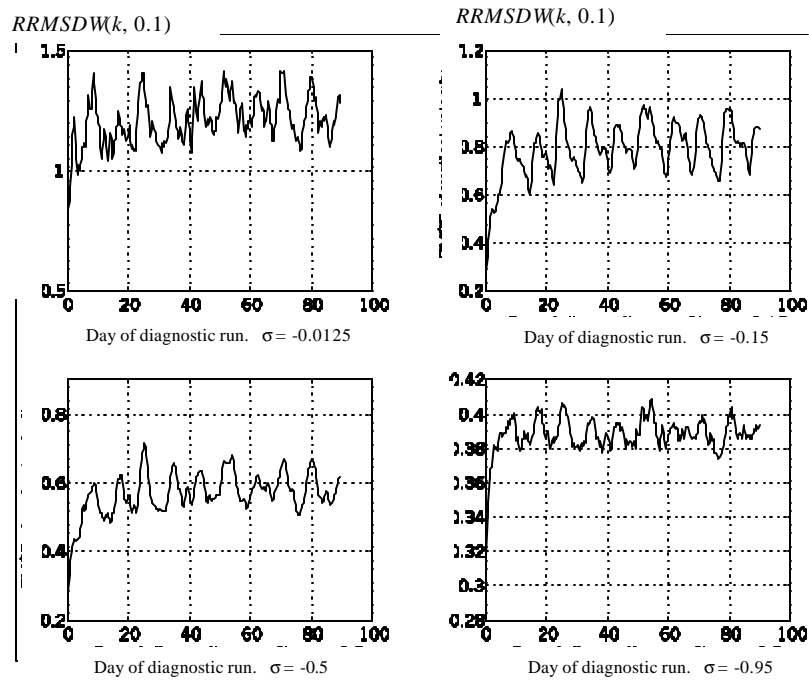


Figure 46. Temporally Varying of $RRMSDW(k, 0.1)$

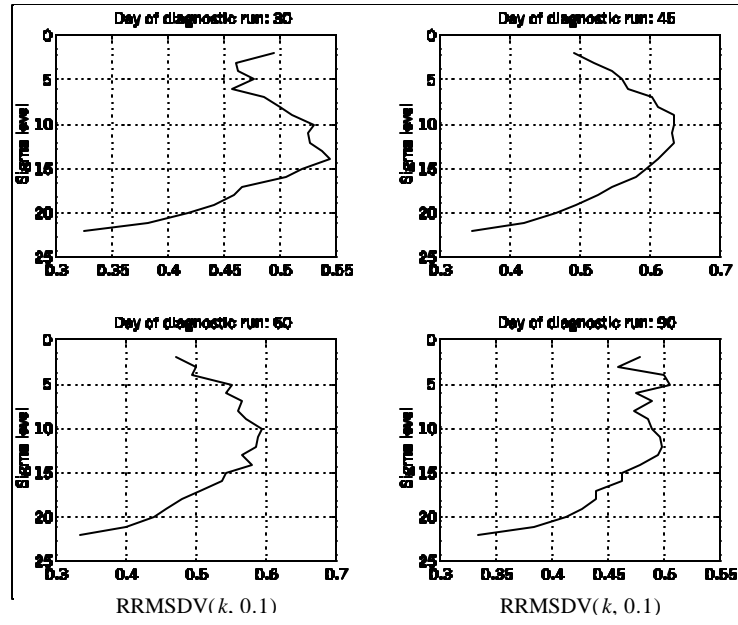


Figure 47. Depth profiles of $RRMSDV(k, 0.1)$ at different day.

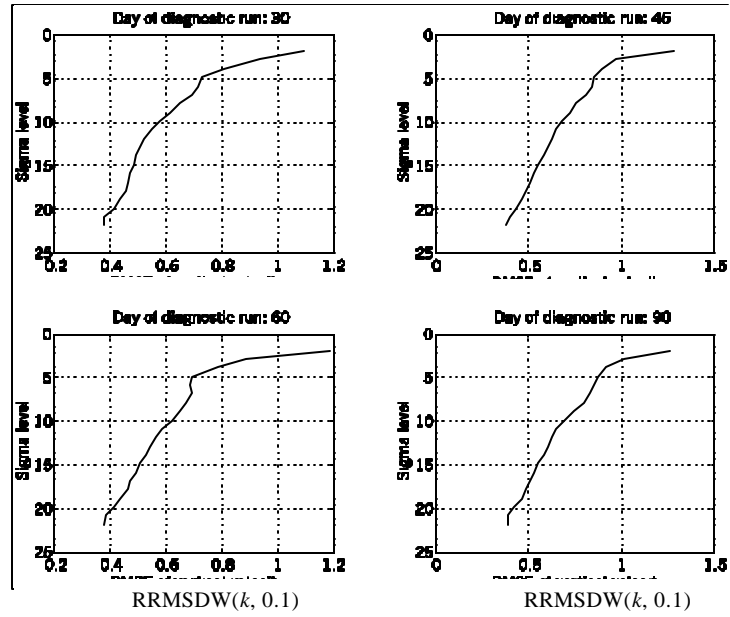


Figure 48. Depth profiles of $RRMSDW(k, 0.1)$ at different day

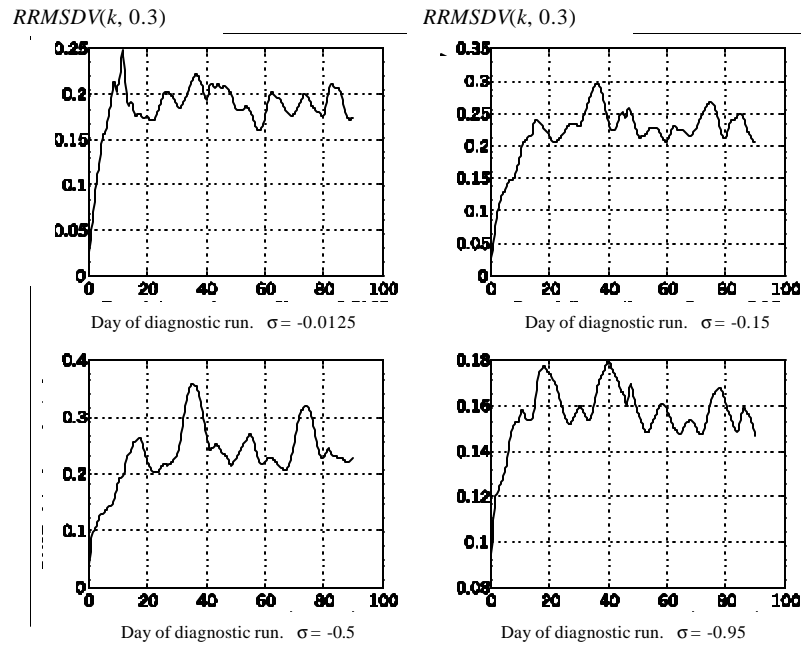


Figure 49. Temporally Varying of $RRMSDV(k, 0.3)$

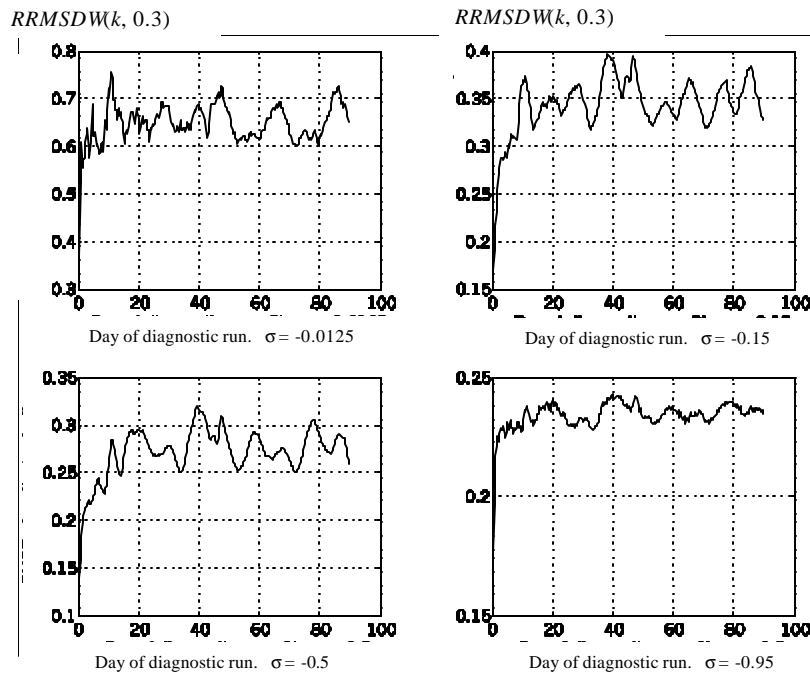


Figure 50. Temporally Varying of $RRMSDW(k, 0.3)$

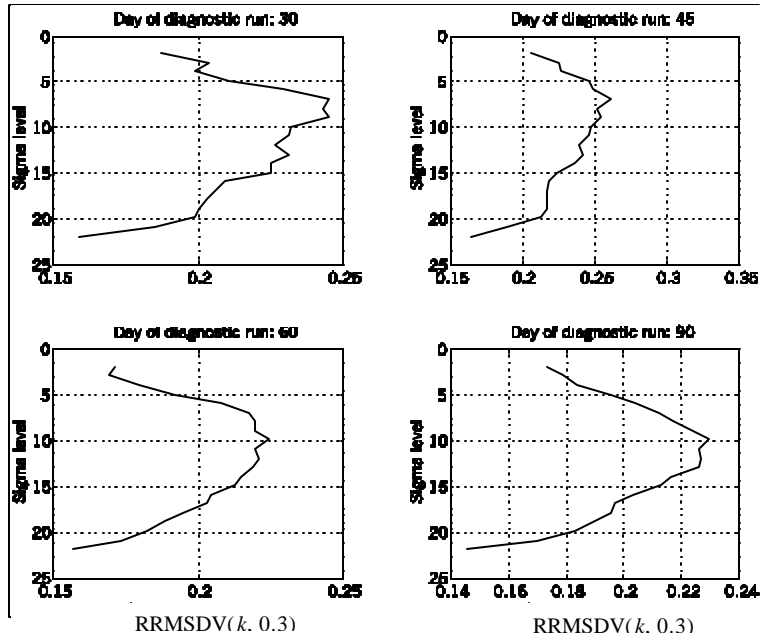


Figure 51. Depth profiles of $RRMSDV(k, 0.3)$ at different day

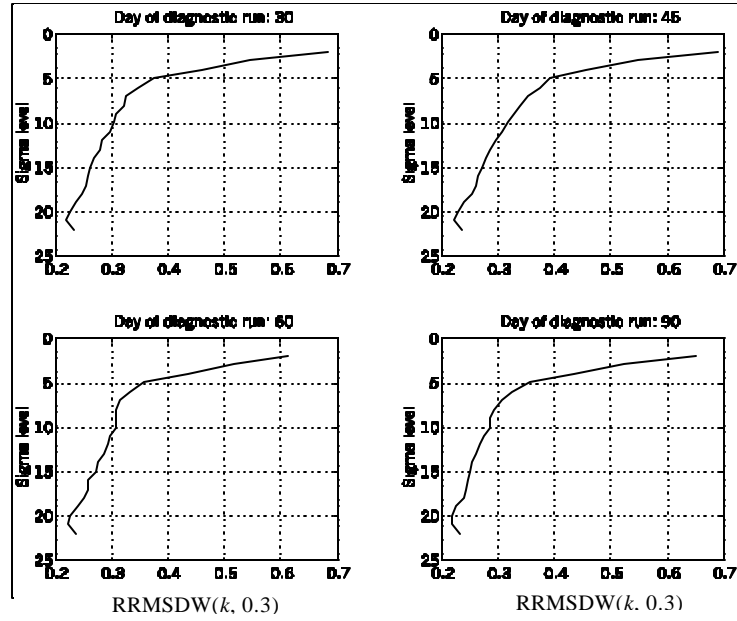


Figure 52. Depth profiles of $RRMSDW(k, 0.3)$ at different day

THIS PAGE INTENTIONALLY LEFT BLANK

VI. UNCERTAINTY OF THE DIAGNOSTICALLY INITIALIZED VELOCITY FIELD DUE TO THE UN CERTAIN LENGTH OF DIAGNOSTIC INTEGRATION

Another unsolved problem is how long the diagnostic integration is needed to obtain a suitable initial velocity field (\mathbf{V}_c). Figures 1-4 showed that after a period of ~ 30 days of diagnostic run, a quasi-steady state is achieved. Thus, the 60th day has been selected as reference field to compute $RRMSDV(t)$ and $RRMSDW(t)$ from day-60 to day-90,

$$RRMSDV(t) = \frac{\sqrt{\sum_{k=2}^{M_z-1} \sum_{j=1}^{M_y} \sum_{i=1}^{M_x} \left[\left(U_{day=t}^{(i,j,k)} - U_{day=60}^{(i,j,k)} \right)^2 + \left(V_{day=t}^{(i,j,k)} - V_{day=60}^{(i,j,k)} \right)^2 \right]}}{\sqrt{\sum_{k=2}^{M_z-1} \sum_{j=1}^{M_y} \sum_{i=1}^{M_x} \left(U_{day=60}^{(i,j,k)} \right)^2 + \left(V_{day=60}^{(i,j,k)} \right)^2}}, \quad (19)$$

$$RRMSDW(t) = \frac{\sqrt{\sum_{k=2}^{M_z-1} \sum_{j=1}^{M_y} \sum_{i=1}^{M_x} \left[\left(W_{day=t}^{(i,j,k)} - W_{day=60}^{(i,j,k)} \right)^2 \right]}}{\sqrt{\sum_{k=2}^{M_z-1} \sum_{j=1}^{M_y} \sum_{i=1}^{M_x} \left(W_{day=60}^{(i,j,k)} \right)^2}}. \quad (20)$$

where $t = 60, 61 \dots 90$, M_z is the number of σ -level.

Figures 53 and 54 show that $RRMSDV(t)$ and $RRMSDW(t)$ fluctuates irregularly with time from day-60 to day-90. The value of $RRMSDV(t)$ increases with time rapidly from day-60 to day-65 and then oscillates around quasi-stationary values for all the C -values. The maximum quasi-stationary of $RRMSDV(t)$ is above 0.6 when $C = 0.05$. When C increases, the quasi-stationary value of $RRMSDV(t)$ decreases. The maximum quasi-stationary of $RRMSDV(t)$ is about 0.09 when $C = 0.03$ (Figure 53).

The value of $RRMSDW(t)$ increases with time rapidly from day-60 to day-65 and then oscillates around quasi-stationary values. The maximum quasi-stationary of $RRMSDW(t)$ is about 0.5 when $C = 0.05$. When C increases, the quasi-stationary value of $RRMSDW(t)$ decreases. The maximum quasi-stationary of $RRMSDW(t)$ is about 0.08 when $C = 0.03$ (Figure 54). These oscillations slow down when C increases. Both the $RRMSDV(t)$ and $RRMSDW(t)$ fluctuate irregularly with time (even though quasi-steady state has been reached). The uncertainty of the diagnostic integration period affects the

uncertainty in the initialized velocity field \mathbf{V}_c significantly and in an unpredictable way. Therefore, it is difficult to determine the time period that the initial velocity field (\mathbf{V}_c) is most appropriate.

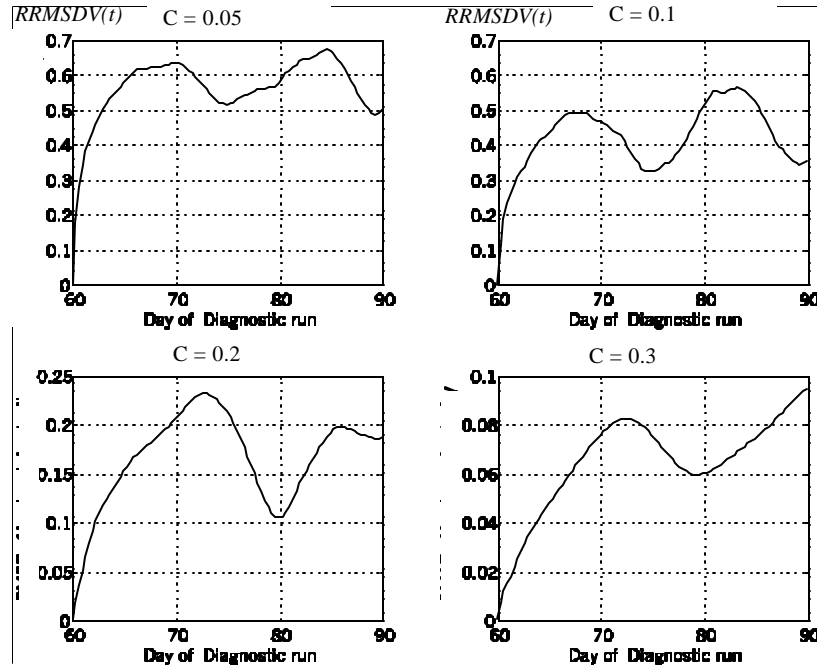


Figure 53. Temporally varying of $RRMSDV(t)$ with four different C -values

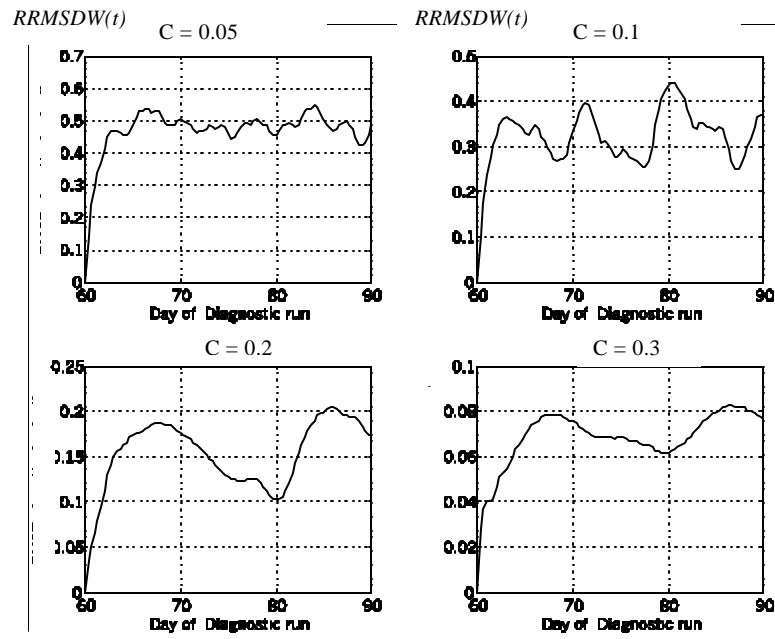


Figure 54. Temporally varying of $RRMSDW(t)$ with four different C -values

THIS PAGE INTENTIONALLY LEFT BLANK

VII. CONCLUSIONS

Diagnostic mode initialization is widely used to obtain the initial velocity field (\mathbf{V}_c) required for the prognostic model run. Together with the climatological temperature and salinity (T_c , S_c), (T_c , S_c , \mathbf{V}_c) fields are treated as the initial conditions for the numerical modeling. However, POM implemented for the SCS revealed that extremely strong thermohaline source/sink terms were generated for $C = 0.05, 0.1, 0.2$ and 0.3 . Such non-physical phenomenon was also observed in the Japan/East Sea when diagnostic initialization was conducted using POM by *Chu and Lan* [2003].

In this thesis, we saw that the strength of the mean heat source/sink, $M_S(|F_T|)$, fluctuates with depth irregularly from the surface to the bottom. The fluctuation also varies with C . At different C -values, the maximum and minimum quasi-stationary values of $M_S(|F_T|)$ occurred at different levels. In general, $M_S(|F_T|)$ increases with time rapidly in the first 5-10 days and then oscillates at different quasi-stationary values for the different C -values. The strength of the absolute mean source/sink decreases across the corresponding level when C increases. The horizontal distributions of heat source/sink term, F_T ($^{\circ}\text{C hr}^{-1}$), at the four levels (near surface, subsurface, mid-level and near bottom) at four different C -values show extremely strong heat sources/sinks generated by the diagnostic initialization. The heat sources/sinks have various scales and strengths. They revealed small- to meso-scale patterns from the surface to the bottom of the SCS but there are some large-scale patterns near the surface of the SCS. In general, when C increases, the strength of the strong and extremely strong sources/sinks decreases in magnitude; nevertheless, they are still above the criteria (11) and (12) in some locations of the SCS. Near the bottom (-3000 m to -4000 m), the SCS basin is less affected by the spurious heat sources and sinks. Although larger C would lead to smaller spurious heat sources and sinks, an excessively large C -value could cause unrealistically strong diffusion in the ocean model and could create other adverse consequences to the model result.

The strength of the mean salt source/sink, $M_S(|F_S|)$ decreases with depth from the surface to the bottom. It increases with time rapidly in the first 5-10 days and then oscillates around quasi-stationary values for the difference cases of C -values after day-20.

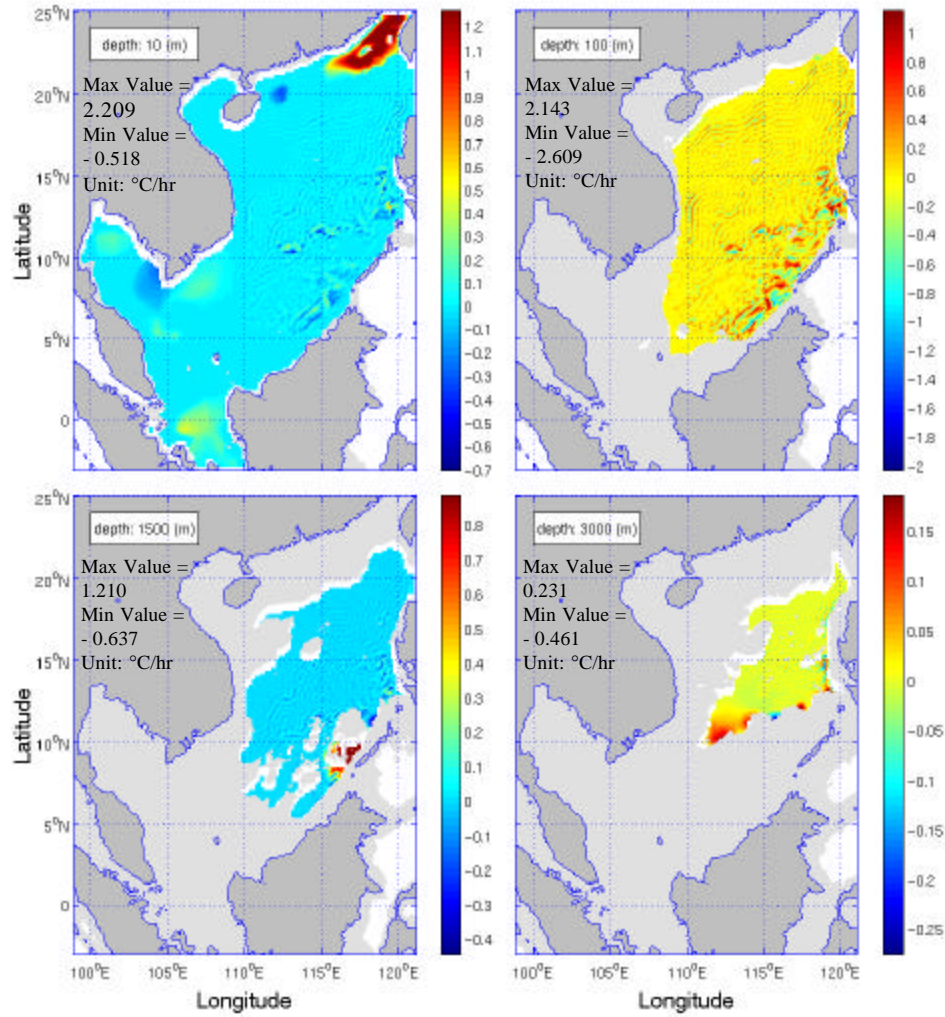
These features are consistent for the four different C -values but the strength of M_s ($|F_s|$) decreases across the corresponding S level when C increases. The horizontal distributions of the salt source/sink term, F_s ($^{\circ}\text{C hr}^{-1}$), at the four S levels (near surface, subsurface, mid-level and near bottom) at four different C -values generated strong and extremely strong salt sources/sinks from the diagnostic initialization. They revealed small- to meso-scale patterns from the surface to the bottom of SCS. In addition, there are some large-scale patterns near the surface of the SCS. Greater salting rate occurred at the surface indicated a more serious spurious salt sources and sinks problem at this level.

The effect of the uncertainty of C on the velocity field generated by the diagnostic initialization process was analyzed through the use of Relative Mean Square Error. It was observed that $RRMSDV(k, C)$ and $RRMSDW(k, C)$ increase with time rapidly in the first 5-10 days and then oscillate around quasi-stationary values for the difference cases of C -values. The largest uncertainty is between $C = 0.05$ and $C = 0.2$ (control run) and the smallest is between $C = 0.3$ and $C = 0.2$ (control run). The uncertainty of the diagnostic integration period affects drastically the uncertainty in the initialized velocity field V_c . These were demonstrated by the $RRMSDV(t)$ and $RRMSDW(t)$ which fluctuate irregularly with time from day-60 to day-90. Thus, it is difficult to determine the time which will yield the most appropriate V_c .

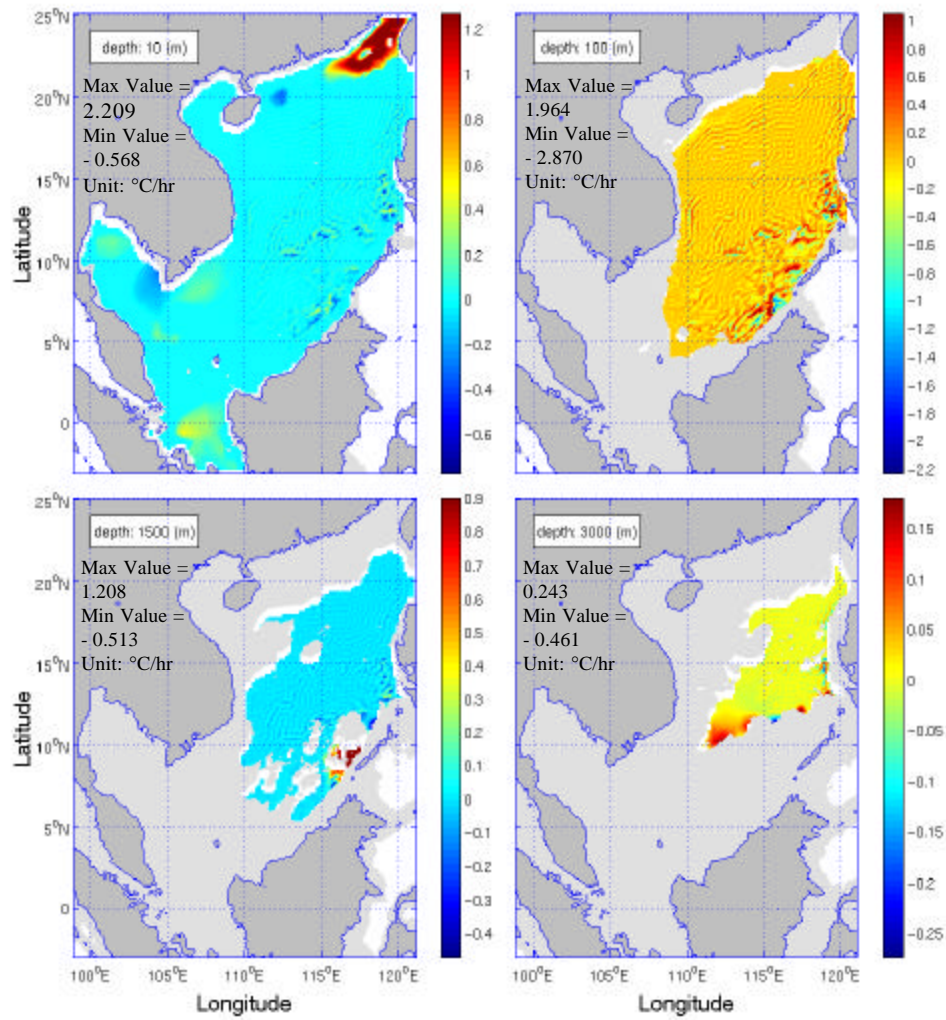
When the prognostic integration starts, F_T and F_s are immediately removed from (5) and (6) (shown in Chapter I). The extremely strong and spatially non-uniform initial heating/cooling (salting/freshening) rates are introduced into the ocean models and cause drastic changes in the thermohaline and velocity fields initially (after the diagnostic run). This effect is especially significant in the deep layer below the thermocline and halocline. Since diagnostic initialization is extensively used, there is an immediate need to develop a check-up algorithm to monitor the strength of the ‘source/sink’ terms during the diagnostic initialization process; otherwise, alternative methods would have to be used to derive V_c .

APPENDIX A. HORIZONTAL DISTRIBUTION OF HEAT SOURCE/SINK TERMS

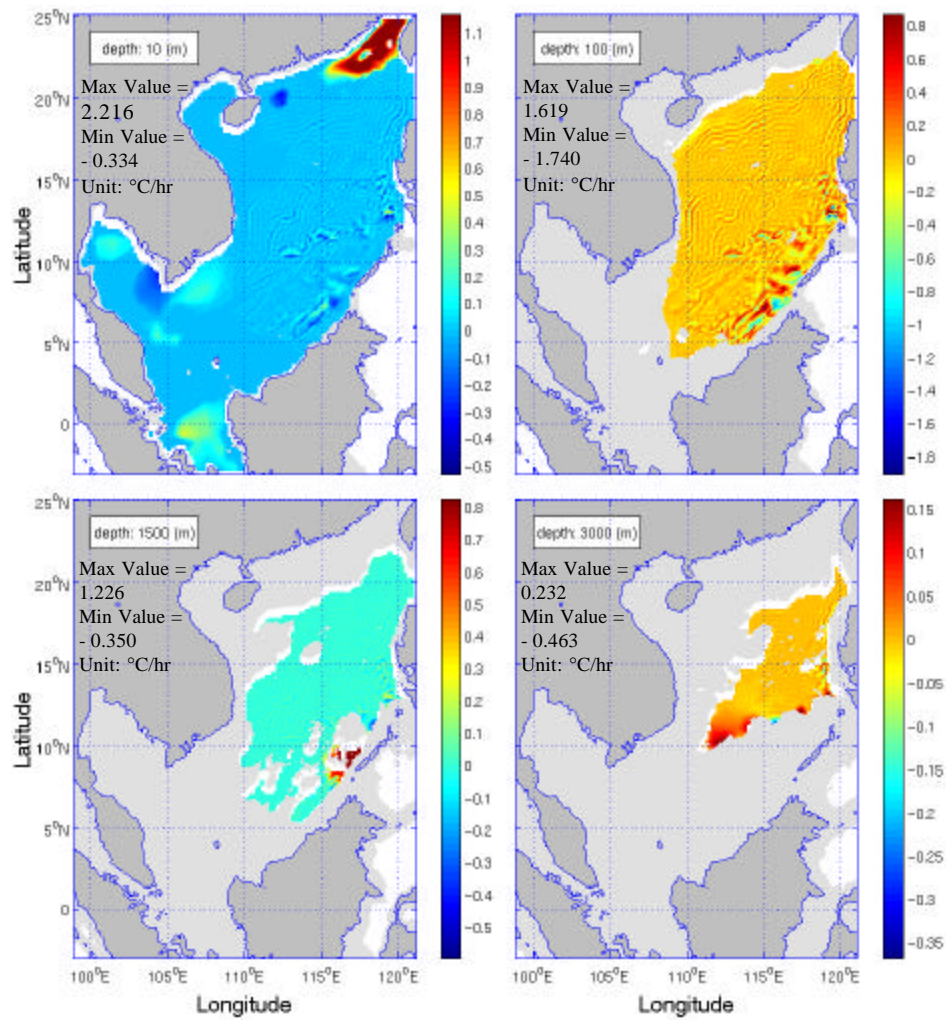
Horizontal distribution of F_T on day-30 with $C = 0.05$



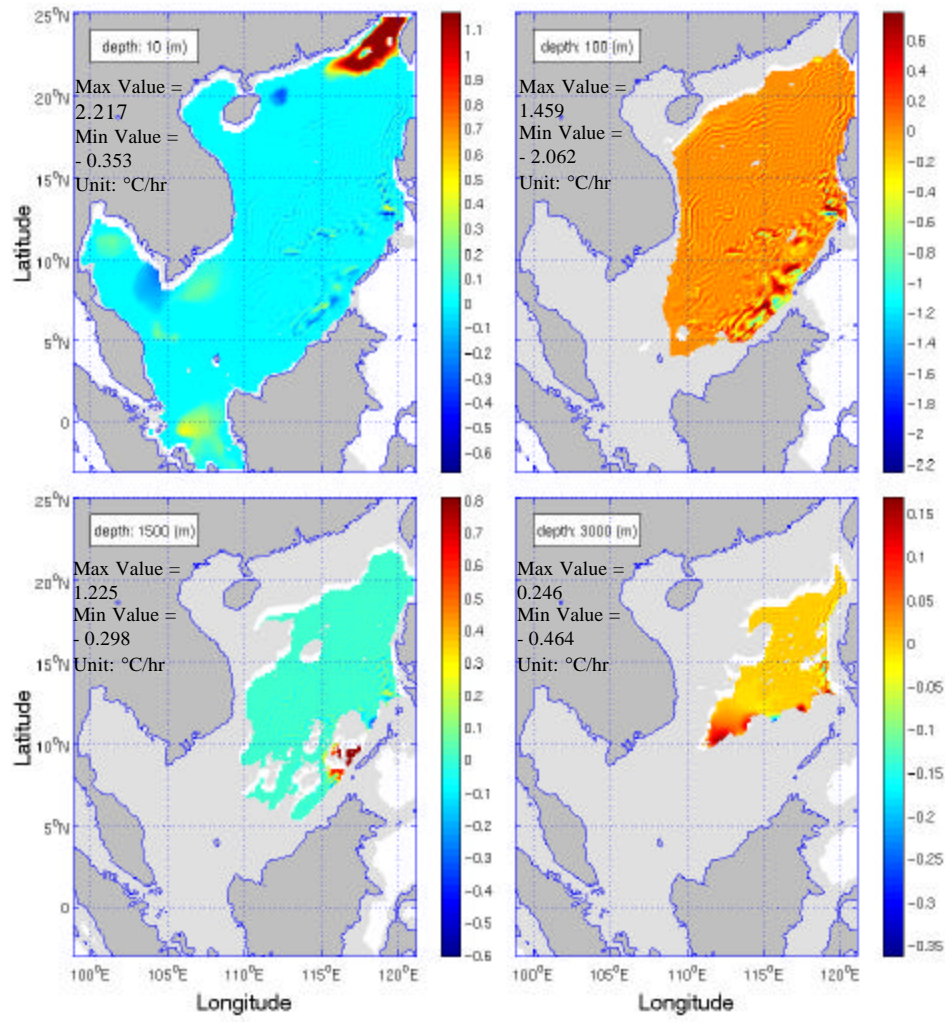
Horizontal distribution of F_T on day-90 with $C = 0.05$



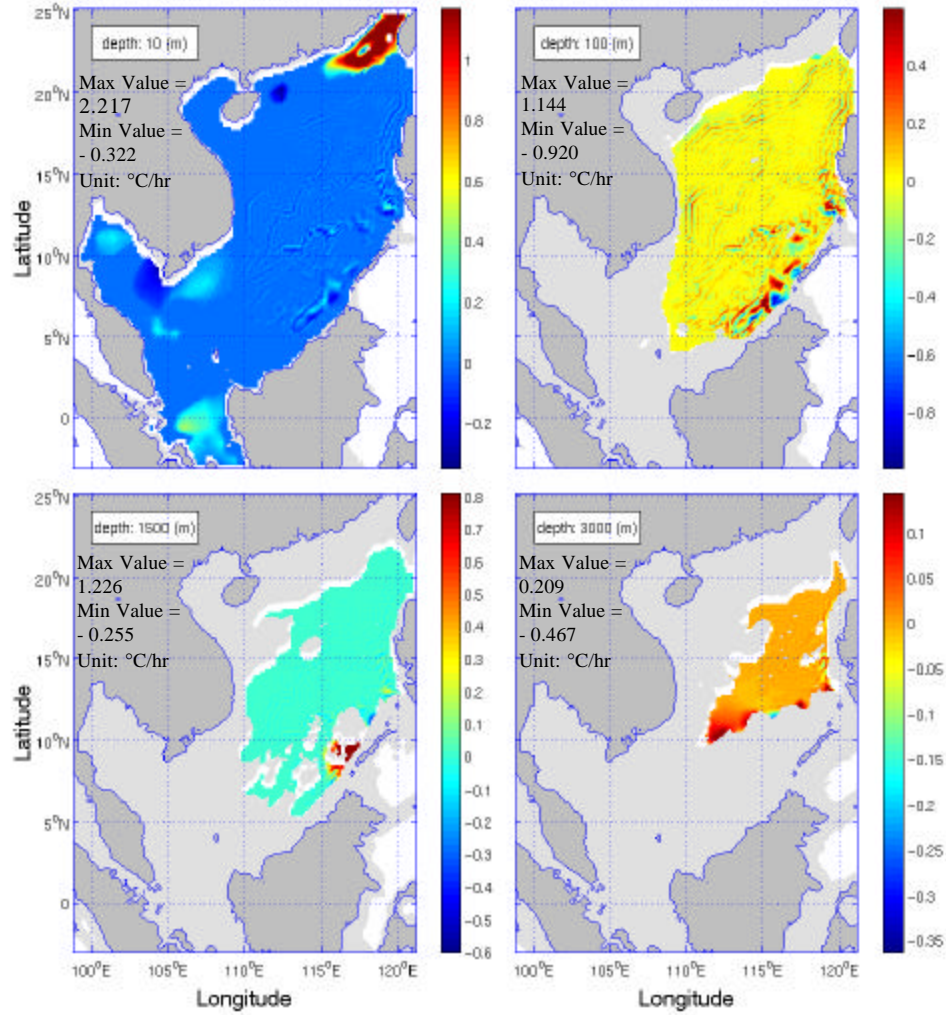
Horizontal distribution of F_T on day-30 with $C = 0.1$



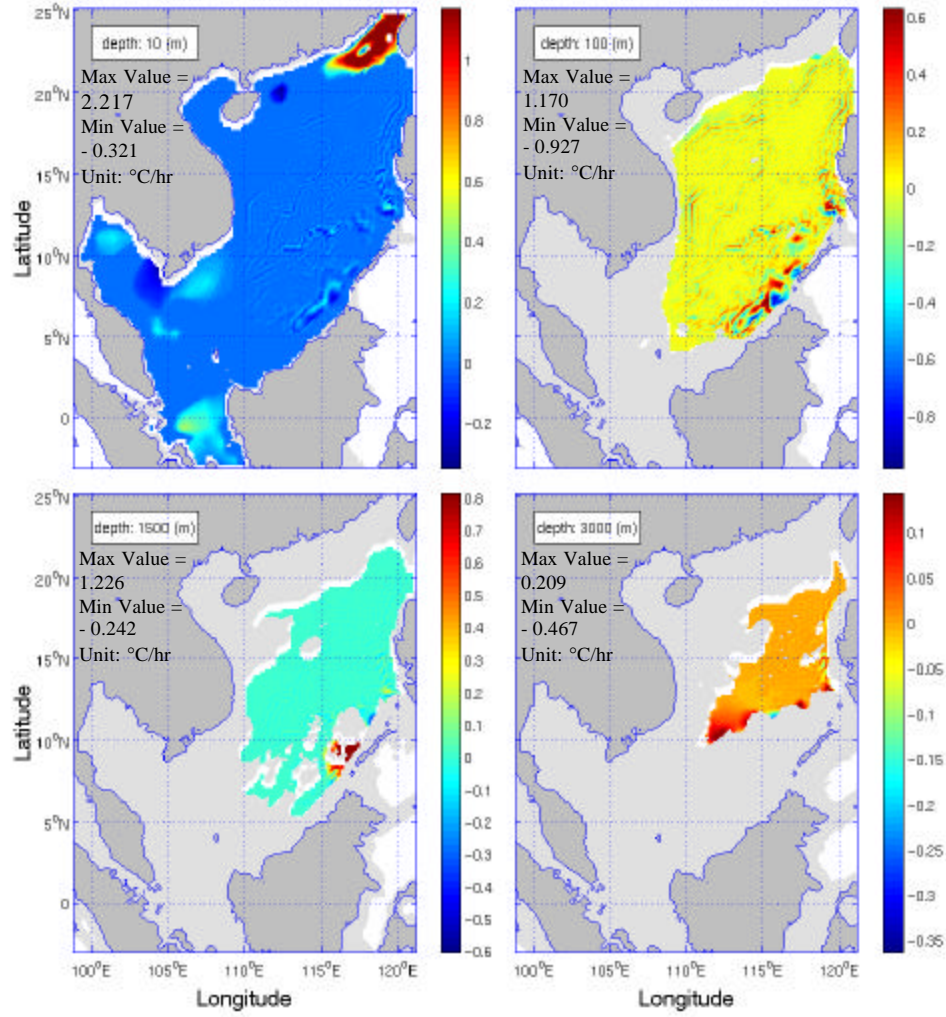
Horizontal distribution of F_T on day-90 with $C = 0.1$



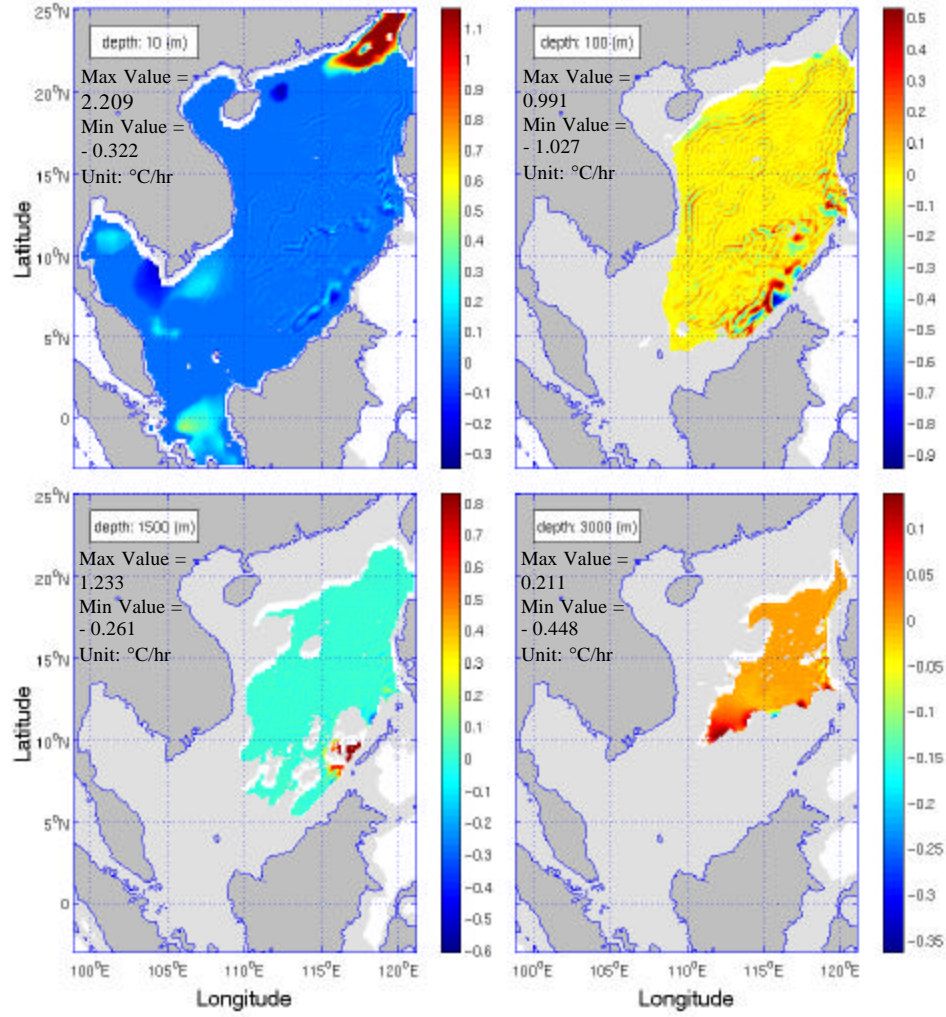
Horizontal distribution of F_T on day-30 with $C = 0.2$



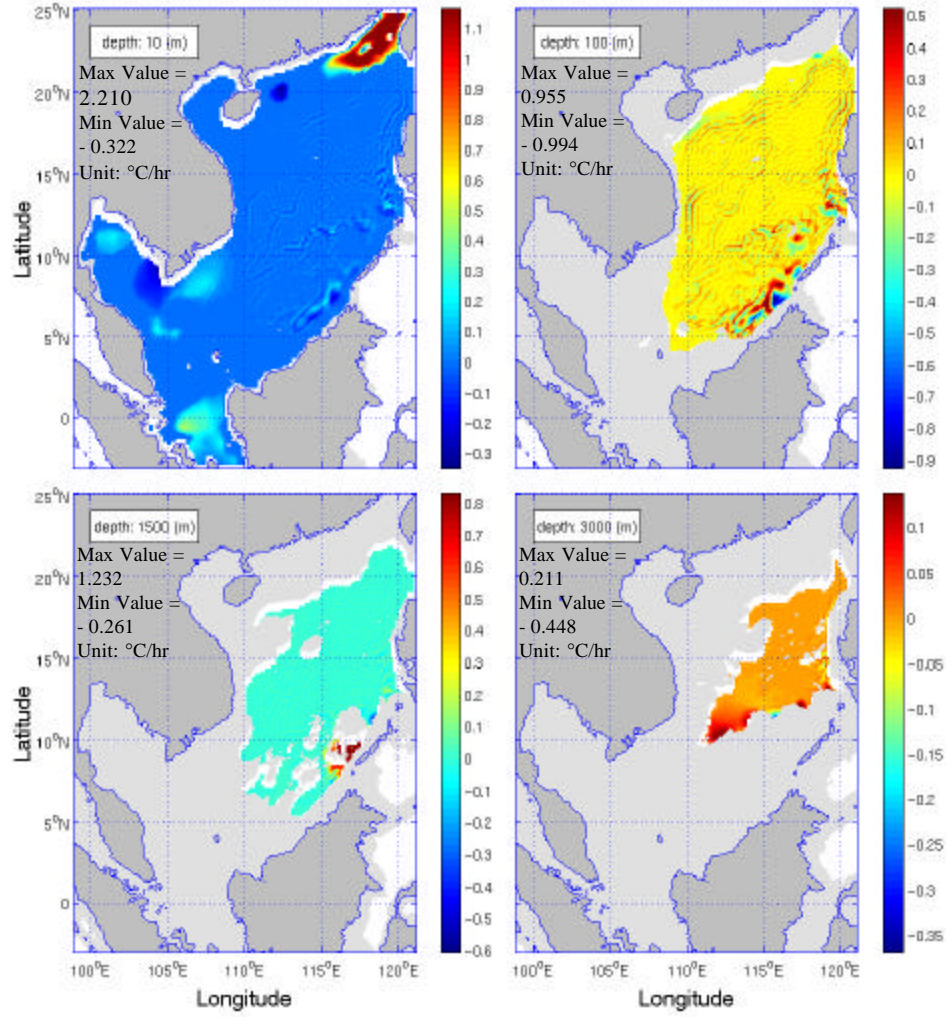
Horizontal distribution of F_T on day-90 with $C = 0.2$



Horizontal distribution of F_T on day-30 with $C = 0.3$

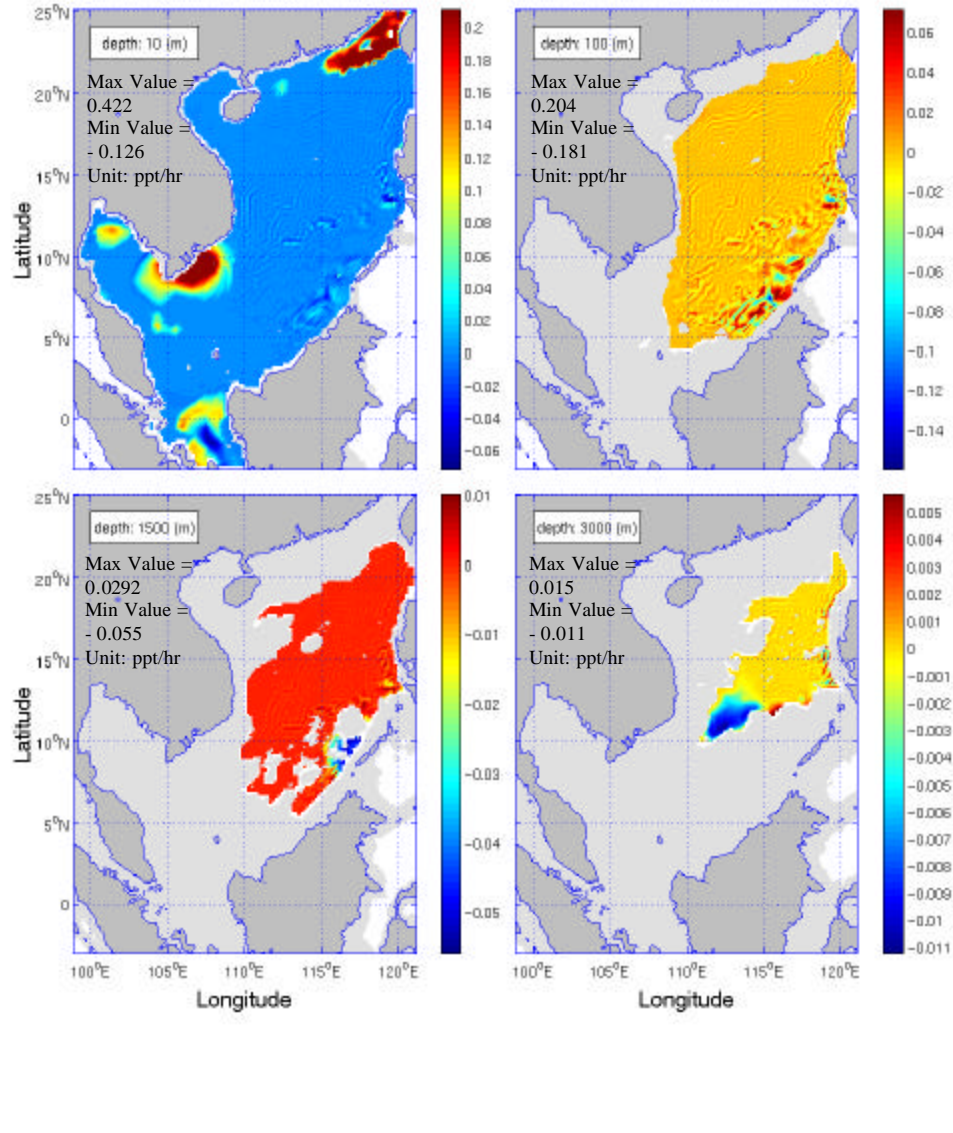


Horizontal distribution of F_T on day-90 with $C = 0.3$

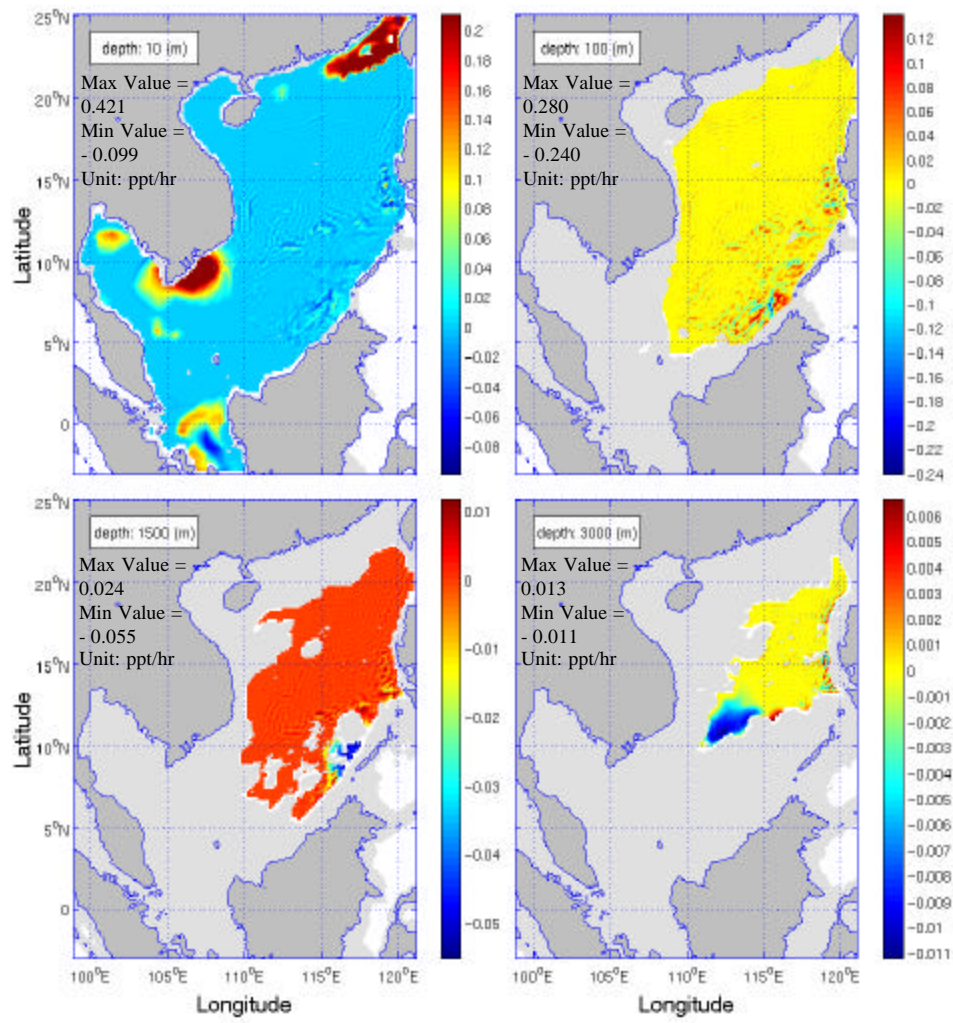


APPENDIX B. HORIZONTAL DISTRIBUTION OF SALT SOURCE/SINK TERMS

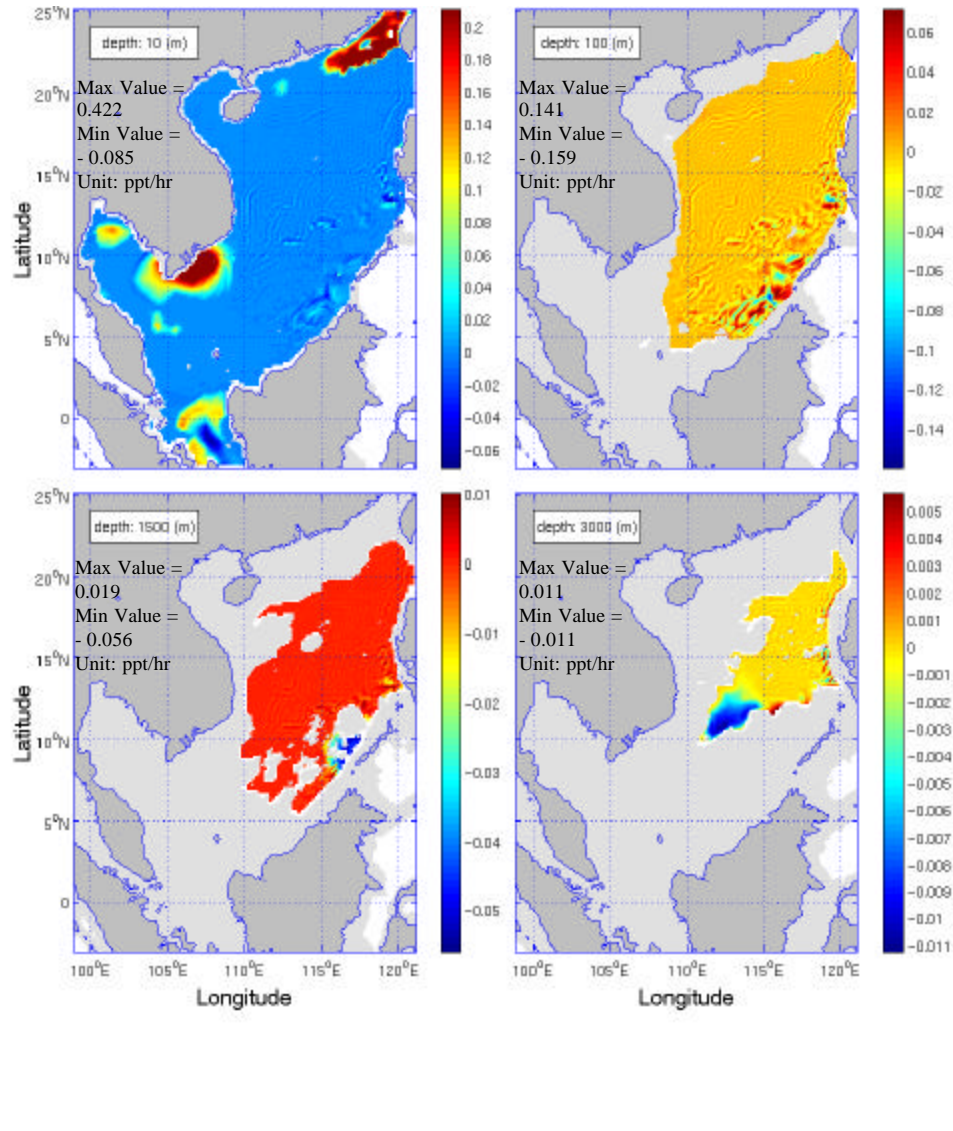
Horizontal distribution of F_s on day-30 with $C = 0.05$



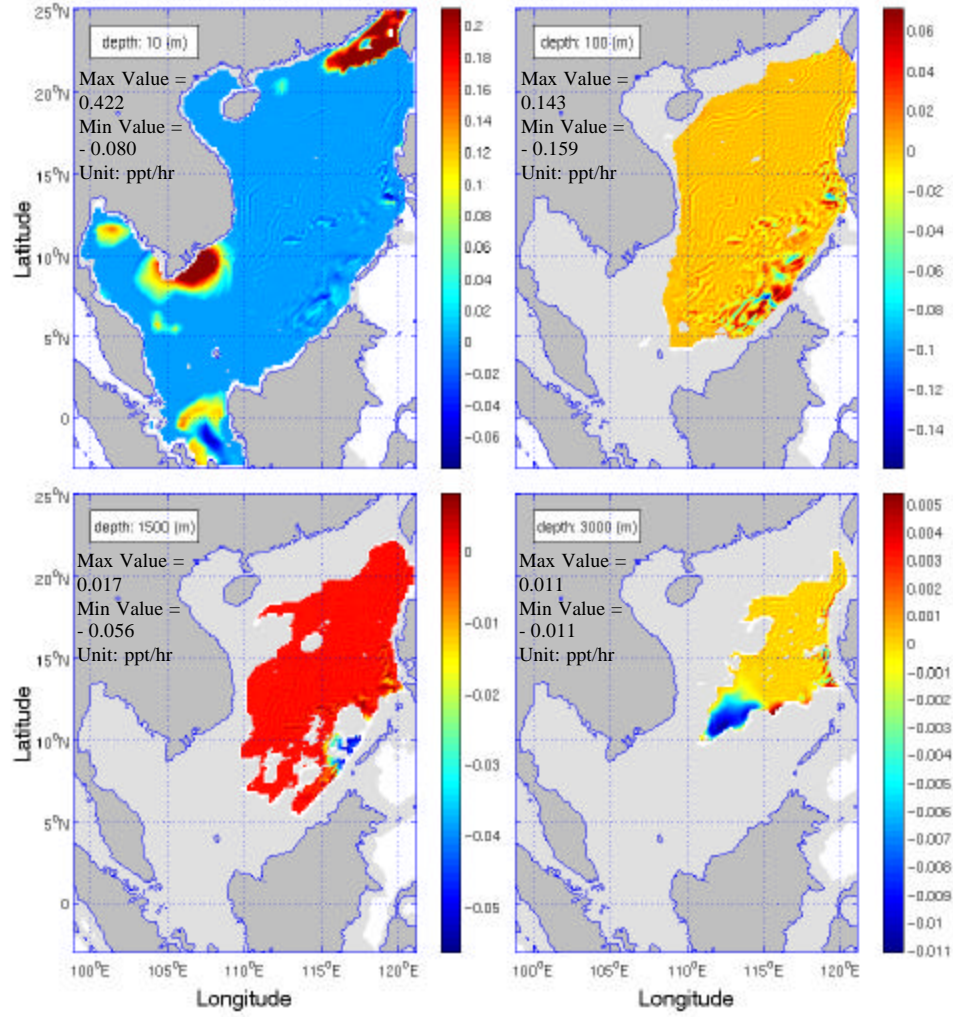
Horizontal distribution of F_S on day-90 with $C = 0.05$



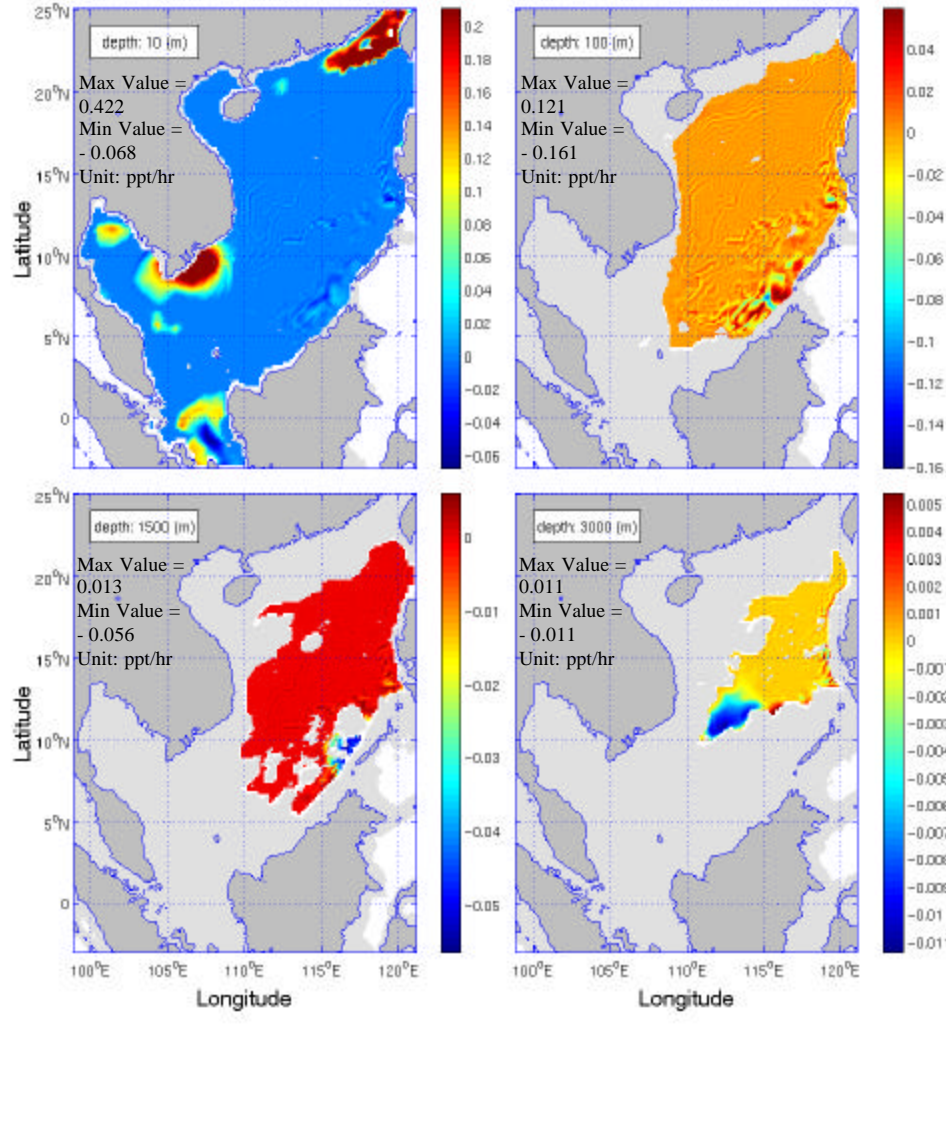
Horizontal distribution of F_S on day-30 with $C = 0.1$



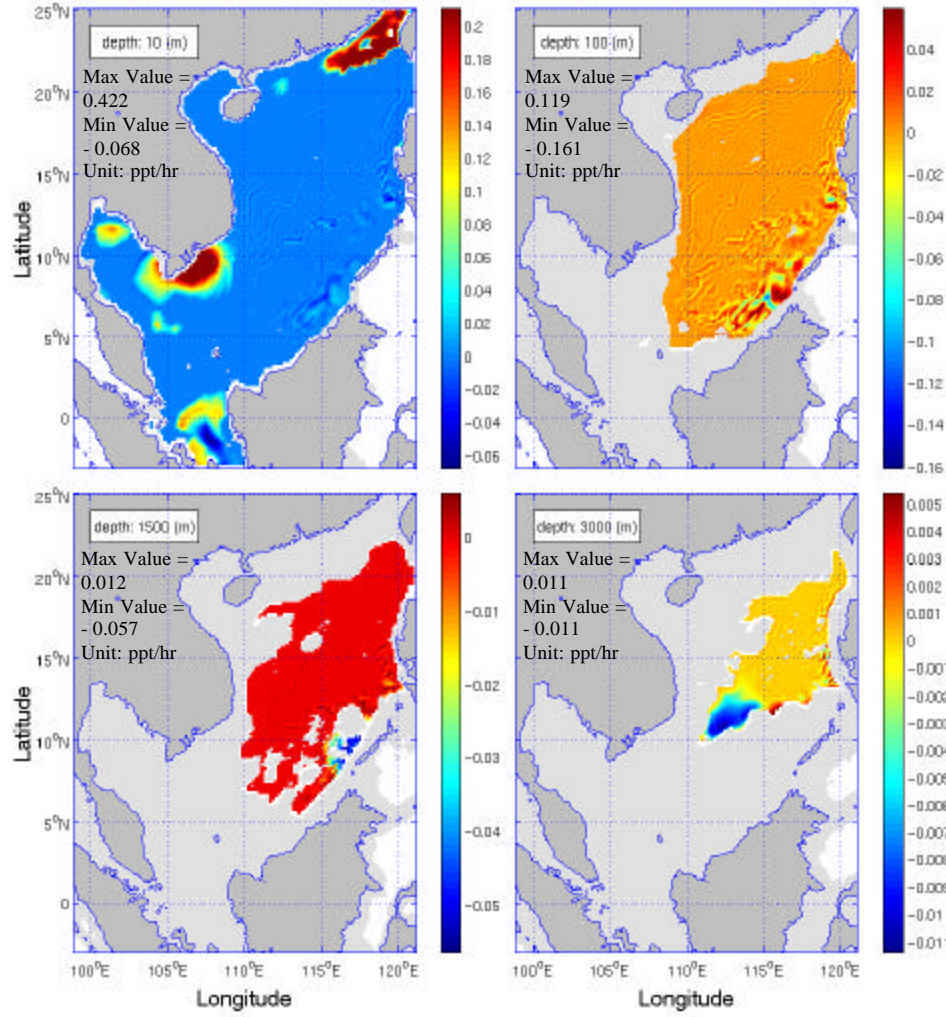
Horizontal distribution of F_S on day-90 with $C = 0.1$



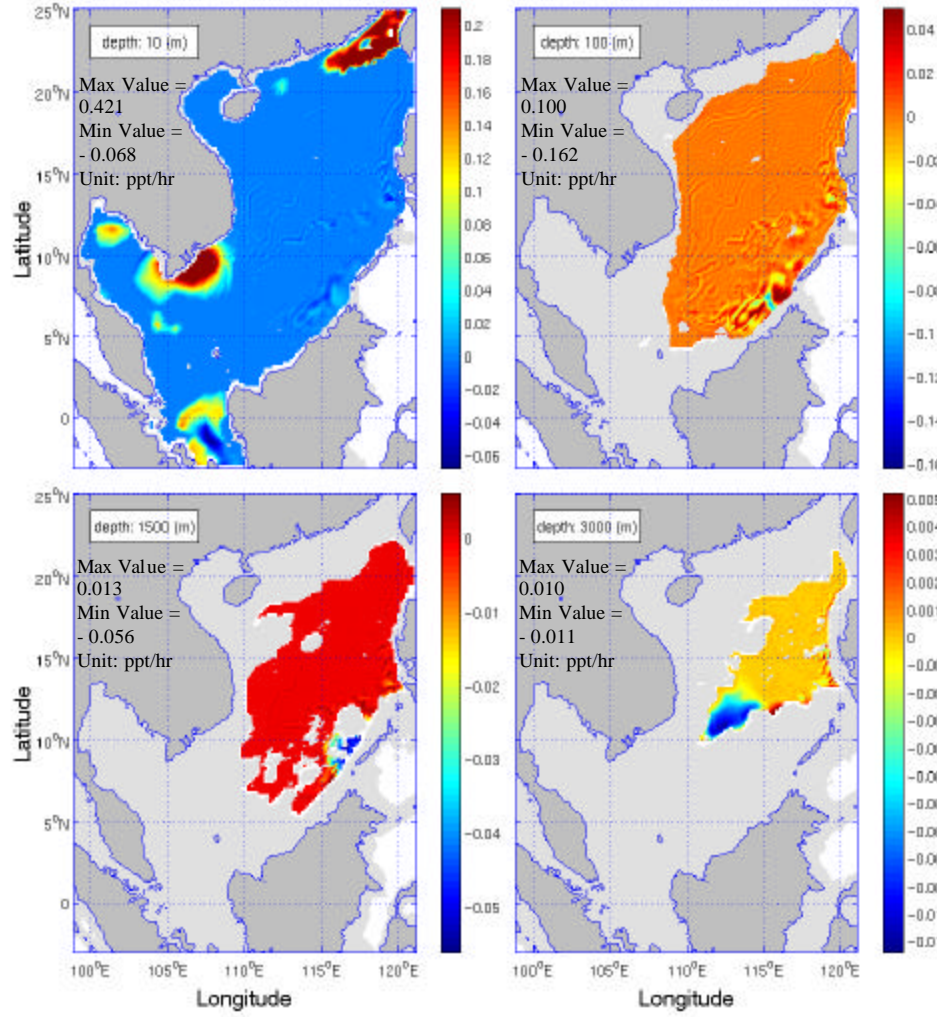
Horizontal distribution of F_S on day-30 with $C = 0.2$



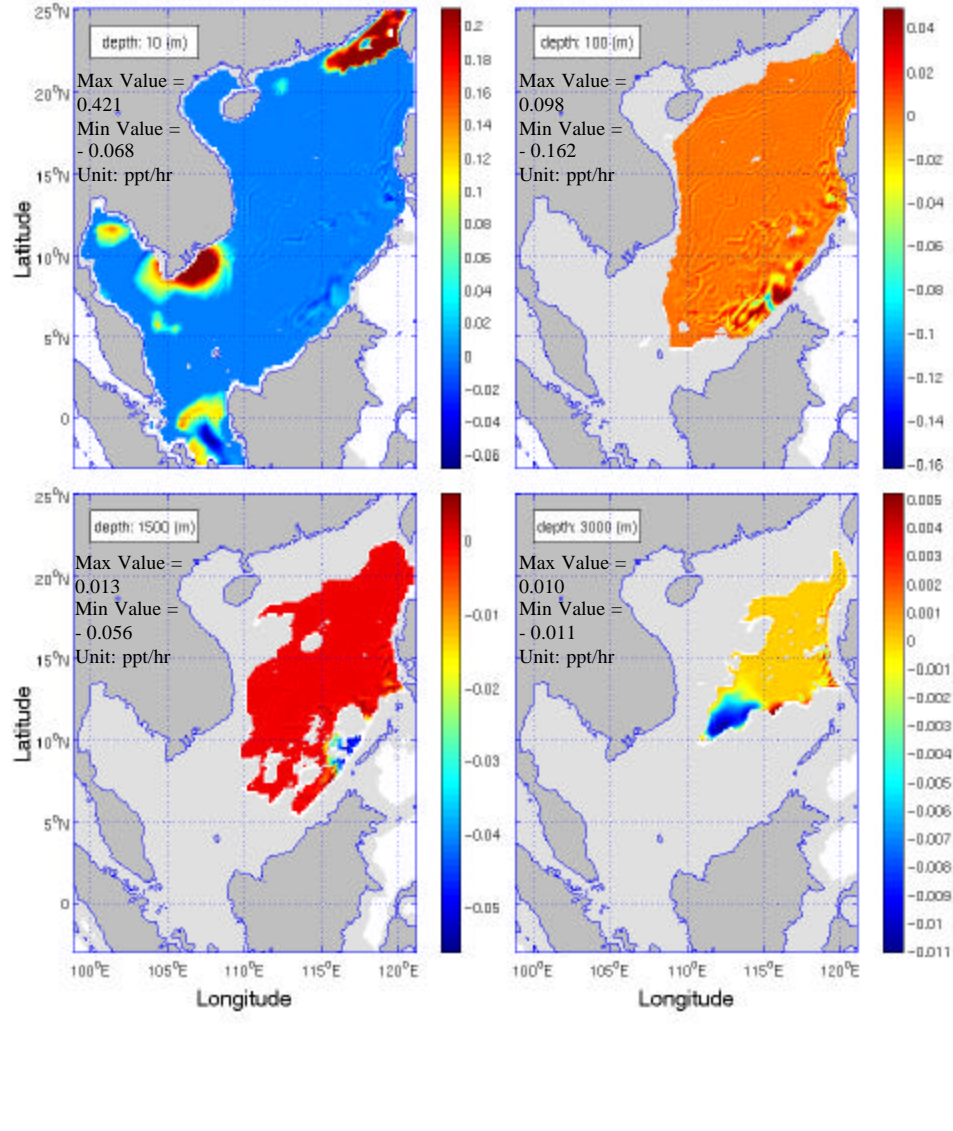
Horizontal distribution of F_S on day-90 with $C = 0.2$



Horizontal distribution of F_S on day-30 with $C = 0.3$



Horizontal distribution of F_S on day-90 with $C = 0.3$



LIST OF REFERENCES

Peter C. Chu, Shihua Lu and Yuchun Chen, *Evaluation of the Princeton Ocean Model Using South China Sea Monsoon Experiment (SCSMEX) Data*. Journal of Atmospheric and Oceanic Technology, v. 18, pp. 1521 -1523, 2001.

George L. Mellor, *Users Guide for the Princeton Ocean Model*. Princeton University, Princeton, NJ 08544-0710, 1998.

Peter C. Chu and Jian Lan, *Extremely Strong Thermohaline Sources/sinks Generated by Diagnostic Initialization*. Geophysical Research Letters, v. 30. no. 0, XXXX, doi:10.1029/2002GL016525, pp. 1-5, 2003 (Article in Proof).

Peter C. Chu, Nathan L. Edmons and Chenwu Fan, *Dynamic Mechanisms for the South China Sea Seasonal Circulation and Thermohaline Variabilities*. Journal of Physical Oceanography, pp. 2971-2975, 1999.

Tomczak, M, and J. S. Godfrey, *Regional Oceanography: An Introduction*, 122-123, Pacific Ocean, 2003.

Peter C. Chu, Binbing Ma and Yuchun Chen, *The South China Sea Thermohaline Structure and Circulation*. Acta Oceanologica Sinica, v. 21, pp. 227-261, 2002.

THIS PAGE INTENTIONALLY LEFT BLANK

INITIAL DISTRIBUTION LIST

1. Defense Technical Information Center
Ft. Belvoir, Virginia
2. Dudley Knox Library
Naval Postgraduate School
Monterey, California
3. Chairman Code OC
Department of Oceanography
Naval Postgraduate School
Monterey, California
4. Professor Peter C. Chu Code OC/CU
Department of Oceanography
Naval Postgraduate School
Monterey, California
5. Mr. Steve D. Haeger
Naval Oceanographic Office
Stennis Space Center, Mississippi
6. Professor Chan Eng Soon
Director Tropical Marine Science Institute
National University of Singapore
7. Ms Cindy Ong
Naval Personnel Department
Republic of Singapore Navy
8. MAJ Ahchuan Ong
Underseas Warfare Centre
Republic of Singapore Navy